Ursula Fernanda Salazar Roggero

Plasmonic nanoantenna arrays for biosensing and electrophysiological monitoring

Arranjos de nanoantenas plasmônicas para biossensoriamento e monitoramento eletrofisiológico

Ursula Fernanda Salazar Roggero

PLASMONIC NANOANTENNA ARRAYS FOR BIOSENSING AND ELECTROPHYSIOLOGICAL MONITORING

Arranjos de nanoantenas plasmônicas para biossensoriamento e monitoramento eletrofisiológico

Thesis presented to the Faculty of Electrical and Computing Engineering of the University of Campinas in partial fulfillment of the requirements for the degree of Doctor in Electrical Engineering, in the area of Telecommunications and Telematics.

Tese apresentada à Faculdade de Engenharia Elétrica e de Computação da Universidade Estadual de Campinas como parte dos requisitos exigidos para a obtenção do título de Doutora em Engenharia Elétrica, na Área de Telecomunicações e Telemática.

Supervisor/Orientador: Prof. Dr. Hugo Enrique Hernandez Figueroa

ESTE EXEMPLAR CORRESPONDE À VERSÃO FINAL DA TESE DEFENDIDA PELA ALUNA URSULA F. S. ROGGERO, E ORIENTADA PELO PROF. DR. HUGO ENRIQUE HERNANDEZ FIGUEROA.

Ficha catalográfica Universidade Estadual de Campinas (UNICAMP) Biblioteca da Área de Engenharia e Arquitetura Elizangela Aparecida dos Santos Souza - CRB 8/8098

Salazar Roggero, Ursula Fernanda, 1991-

Sa31p

Plasmonic nanoantenna arrays for biosensing and electrophysiological monitoring / Ursula Fernanda Salazar Roggero. – Campinas, SP: [s.n.], 2025.

Orientador: Hugo Enrique Hernandez Figueroa. Tese (doutorado) – Universidade Estadual de Campinas (UNICAMP), Faculdade de Engenharia Elétrica e de Computação.

1. Plasmônicas. 2. Antenas óticas. 3. Biossensores. 4. Cortisol. 5. Eletrofisiologia. 6. Miócitos cardíacos. I. Hernandez Figueroa, Hugo Enrique, 1959-. II. Universidade Estadual de Campinas (UNICAMP). Faculdade de Engenharia Elétrica e de Computação. III. Título.

Informações complementares

Título em outro idioma: Arranjos de nanoantenas plasmônicas para biossensoriamento e monitoramento eletrofisiológico

Palavras-chave em inglês:

Plasmonics

Optical antennas

Biosensors

Cortisol

Electrophysiology

Cardiomyocytes

Área de concentração: Telecomunicações e Telemática

Titulação: Doutora em Engenharia Elétrica

Banca examinadora:

Hugo Enrique Hernandez Figueroa [Orientador]

José Alexandre Diniz

Marcos Vinicius Puydinger dos Santos

Aitzol Garcia Echarri

Andreas Seifert

Data de defesa: 15-04-2025

Programa de Pós-Graduação: Engenharia Elétrica

Objetivos de Desenvolvimento Sustentável (ODS)

ODS: 9. Inovação e infraestrutura ODS: 3. Saúde e bem-estar

Identificação e informações acadêmicas do(a) aluno(a)

- ORCID do autor: https://orcid.org/0000-0001-9813-3781
- Currículo Lattes do autor: http://lattes.cnpq.br/6926967476833109

Prof. Dr. Hugo Enrique Hernandez Figueroa (Presidente)

Prof. Dr. José Alexandre Diniz

Prof. Dr. Marcos Vinicius Puydinger dos Santos

Prof. Dr. Aitzol Garcia Echarri

Prof. Dr. Andreas Seifert

A ata de defesa, com as respectivas assinaturas dos membros da Comissão Julgadora, encontra-se no SIGA (Sistema de Fluxo de Dissertação/Tese) e na Secretaria de PósGraduação da Faculdade de Engenharia Elétrica e de Computação.

To my family for their unconditional support and to my nieces and nephews for their loving hugs. Also, to all those who defend Science in Brazil and throughout Latin America.

Acknowledgment

First and foremost, I would like to express my deepest gratitude to my advisor, Prof. Hugo Figueroa. You placed your trust in me and gave me the confidence to embark on this graduate journey. Over these eight years, you have been more than just an advisor; you and your family have supported me like my own. For that, I am eternally grateful.

I extend my sincere thanks to all the research groups I collaborated with at my beloved UNICAMP. Thank you to everyone from LEMAC, LEEDS, and LPCV for the countless hours spent studying, discussing, and experimenting together. A special thank you to my colleagues Gustavo, Jorge, Yuri, Jhonattan, Paloma, Ruth, Luciano, Luana, Freddy, Waldemir, Bruna, and Adriano, as well as the dedicated technicians, Rubia and Elizângela. My heartfelt appreciation goes to the professors who generously collaborated on this project: Prof. Lauro Kubota (in memoriam), and Profs. José and Rosana Bassani.

How can I not mention my incredible journey in the Basque Country, where I gained profound knowledge in nanosciences and met amazing people? My warmest gratitude to Prof. Andreas Seifert and to my dear friends and colleagues Laura (que hubiera sido de mí en Euskal Herria sin ti, Lauracha!), Ralph (my nanofabrication father!), Renata (jednog dana ću otići u Hrvatsku!), Isabel, Maitane, Marita, Eneko, Harun (seni çok seviyorum bebeğim <3), and Olga, from nanoGUNE. I am also deeply thankful to Prof. Aitzol García for welcoming me into his group at DIPC and providing the opportunity to extend my time in Donostia. Mario Zapata from CFM-DIPC, thank you immensely for all the nanophotonics knowledge you shared with me, but more importantly, for your advice and true friendship. Mila esker guztioi!

I would also like to thank the research centers where I had the opportunity to learn micro and nanofabrication techniques: CTI and CCSnano. I am grateful to Prof. Stanislav, Mara, Luana, Silvia, Emilio, Raluca, Daniel, Andrei, and Maria das Graças.

This journey has been long, and I would not have reached this point without the wonderful people who accompanied me along the way. I am incredibly fortunate to have two families: my blood family in Peru and the family I built in Brazil with the most supportive friends ever. I can never thank you enough for always being there for me, no matter the time or place. Pa', ma', lo logramos, gracias por nunca rendirse y permitirme soñar! Hermanos, un millón de gracias por ser esa red de apoyo incondicional, contemos siempre con nosotros! A mi Lua, Facu, Noah, Iso, Lucho e Emi gracias por enseñarme ese amor tan bonito y puro. Cuenten con tía Uchi (o Puchi) siempre! A mi mamita Yola, gracias por estar desde el día 1, cuidarme y no juzgarme. A mis puritas sin mezcla Kati, Gabi y Mili, los años no pasan por nosotras (o por nuestra amistad). A Clau y Jimmy, de UPC para la vida, mis incondicionales, los espero en Brazil. A mis muchachos de bien, David, Abel y Karen (e Canelinha), que privilegio es tenerlos! A minhas koalas, não só me apresentaram o futebol americano, me deram uma família. Ka, Neki, e Jé, obrigada por lutar do meu lado em cada batalha, dentro e fora do campo! E às lovelaces queridas, obrigada por me permitirem voltar ao futebol da maneira mais divertida. Só love, só love!

I also extend my gratitude to all the professors who shared their knowledge with me throughout my academic journey. Thank you for being my guides and inspirations.

This study was financed in part by the Coordenação de Aperfeiçoamento de Pessoal de Nível Superior – Brasil (CAPES) – Finance Code 001. In addition, this work was carried out with the support of CNPq, Conselho Nacional de Desenvolvimento Científico e Tecnológico - Brasil (381928/2023-3, 384028/2024-1, 381850/2024-2).

Para los que ya no están, para los que están y los que vienen.
Residente and Orishas, Pa'l norte

Resumo

Este trabalho apresenta o desenvolvimento e a aplicação de um arranjo de nanoantenas plasmônicas de dupla funcionalidade, projetada para biossensoriamento e monitoramento eletrofisiológico de células. O dispositivo opera na região do infravermelho próximo, aproveitando suas vantagens de baixa reflexão e absorção em tecidos, sendo ideal para potenciais aplicações *in-vivo*. As nanoantenas de ouro foram projetadas por meio de simulações eletromagnéticas para alcançar fortes efeitos de ressonância plasmônica de superfície localizada (LSPR) e ressonância de rede de superfície (SLR). A fabricação foi realizada utilizando litografia por feixe de elétrons, seguida pela caracterização óptica em um sistema espectroscópico configurado em modo de transmissão.

A primeira funcionalidade, biossensoriamento, foi demonstrada por meio de uma prova de conceito com soluções de sacarose, seguida por testes especializados para detecção de cortisol, um biomarcador chave relacionado ao estresse. O arranjo de nanoantenas foi biofuncionalizado com aptâmeros específicos para o cortisol, permitindo a detecção molecular sem uso de marcadores. O dispositivo alcançou uma sensibilidade de 471 nm/RIU, uma figura de mérito de 8.3 RIU⁻¹ e um limite de detecção de 166.6 nM. Considerando a simplicidade e a reprodutibilidade do arranjo de nanodiscos fabricado, esses resultados evidenciam seu potencial como uma plataforma diagnóstica portátil e miniaturizada para detecção biomolecular em tempo real.

A segunda funcionalidade, o monitoramento eletrofisiológico, foi validada pela detecção de potenciais de campo extracelular gerados por cardiomiócitos isolados de ratos. Os registros optoeletroquímicos mostraram que a luz espalhada pelo arranjo de nanoantenas foi modulada por um campo elétrico externo aplicado sobre o dispositivo. Experimentos biológicos confirmaram, adicionalmente, a capacidade do dispositivo de monitorar a atividade elétrica de células unitárias e pequenos grupos de células, demonstrando uma alta resolução espacial, operação em tempo real e capacidades sem fio.

Esta tese de doutorado representa um avanço significativo na área, ao relatar o primeiro registro óptico da atividade elétrica de cardiomiócitos individuais utilizando nanoantenas plasmônicas, realizando experimentos eletrofisiológicos ex-vivo inéditos. Além disso, sua funcionalidade dupla permite realizar o monitoramento eletrofisiológico de células complementado pela detecção biomolecular, proporcionando uma análise abrangente. Comparado a tecnologias convencionais, como ensaios imuno-enzimáticos (ELISA) e arranjos de microeletrodos, o dispositivo oferece vantagens únicas, incluindo detecção sem marcadores, alta resolução espaço-temporal e versatilidade para estudar diversos tipos de células e analitos.

Em conclusão, o arranjo de nanoantenas plasmônicas demonstrou com sucesso sua dupla funcionalidade como uma ferramenta poderosa para biossensoriamento e monitoramento eletrofisiológico. Seu potencial para aplicações em tempo real, sem fio e sem necessidade de marcadores a torna uma tecnologia promissora para o avanço da pesquisa biológica e diagnósticos clínicos. Perspectivas futuras incluem a ampliação de suas aplicações para outros tipos de células excitáveis e biomarcadores, a realização de estudos *in-vivo* e a exploração de usos inovadores, como interfaces cérebro-computador e plataformas de órgãos-em-chip.

Abstract

This work presents the development and application of a dual-purpose plasmonic nanoantenna array designed for biosensing and electrophysiological monitoring of cells. The device operates in the near-infrared region (NIR-I), leveraging its advantages of reduced tissue reflection and absorption for potential *in-vivo* applications. The gold nanoantennas were designed through electromagnetic simulations to achieve strong localized surface plasmon resonance (LSPR) and surface lattice resonance (SLR) effects. Fabrication was accomplished using electron beam lithography, followed by optical characterization in a spectroscopic setup with a transmission configuration.

The first functionality, biosensing, was demonstrated through proof-of-concept experiments using sucrose solutions, followed by specialized tests for detecting cortisol, a key biomarker for stress. The nanoantenna array was biofunctionalized with cortisol-specific aptamers, enabling label-free molecular detection. The device exhibited competitive sensing performance, achieving a sensitivity of 471 nm/RIU, a figure of merit (FOM) of 8.3 RIU⁻¹, and a limit of detection (LoD) of 166.6 nM. Considering the simplicity and reproducibility of the fabricated nanodisk array, these results highlight its potential as a portable and miniaturized diagnostic platform for real-time biomolecular detection.

The second functionality, electrophysiological monitoring, was validated by detecting extracellular field potentials generated by isolated cardiomyocytes from rats. Optoelectrochemical recordings revealed that the scattered light from the nanoantenna array was modulated by an external electric field applied across the array. Biological experiments further confirmed the device's ability to monitor the electrical activity of single cells and small groups of cells, demonstrating high spatial resolution, real-time operation, and wireless capabilities.

This doctoral thesis represents a significant advancement in the field, as it reports the first optical recording of the electrical activity of single cardiomyocytes using plasmonic nanoantennas, successfully performing unprecedented ex-vivo electrophysiological experiments. Furthermore, its dual-functionality allows for electrophysiological monitoring complemented with biomolecular detection, enabling comprehensive analysis. Compared to conventional technologies such as enzyme-linked immunosorbent assays (ELISA) and microelectrode arrays (MEAs), the device offers unique advantages, including label-free detection, high spatio-temporal resolution, and versatility for studying various cell types and biomarkers.

In conclusion, the plasmonic nanoantenna array has successfully demonstrated its dual functionality as a powerful tool for biosensing and electrophysiological monitoring. Its potential for real-time, wireless, and label-free applications makes it a promising technology for advancing biological research and clinical diagnostics. Future directions include expanding its applications to other excitable cells and biomarkers, conducting *in-vivo* studies, and exploring innovative uses such as brain-computer interfaces (BCIs) and organ-on-a-chip (OoC) platforms.

List of Figures

1.1 1.2	Scale comparison between nanostructures and biological features Schematic illustration of the nanoantenna-based platform for biomolecule	22
1.2	detection and cell monitoring.	23
2.1	Plasmonic nanostructures: Electron microscopy images and corresponding	
	optical responses	27
2.2	Nanofabrication approaches: top-down and bottom-up	28
2.3	Electron beam lithography. a) Schematic diagram. b) Equipment	30
2.4	Spin coating process. a) Schematic of the operating principle. b) Spin coater	31
2.5	PVD75 equipment from Kurt J. Lesker company, used in this work	32
2.6	Schematic diagram of the electropolymerization setup	33
2.7	General scheme of an optical biosensor	34
2.8	Transmittance spectra of an LSPR-based biosensor for detection purposes.	35
2.9	Operating principle of nanoantennas as electrophysiological probes	38
3.1	Working principle of the plasmonic nanoantenna array as a two-purpose	
	device: biomolecular sensor and electrophysiological probe	42
3.2	Scheme of the nanoantenna array. a) Side view. b) Top view	43
3.3	Simulated scattering spectra of plasmonic gold nanodisks, obtained with	
	Ansys Lumerical. Sweeps in diameter from 200 nm to 250 nm, and in height	
	from 40 nm to 50 nm	44
3.4	Simulated local electric field enhancement of gold nanodisks using Ansys	
	Lumerical. a) Side view. b) Top view	45
3.5	Simulated transmittance spectra of a nanoantenna arrays with varying lattice periods. Single element: gold nanodisks with 225 nm diameter and	
	45 nm thickness. Simulations were performed in COMSOL Multiphysics	
	and validated with Ansys Lumerical.	46
3.6	Simulated local field enhancement of the gold nanodisks in array configuration	
	using Ansys Lumerical. a) Side view. b) Top view	47
3.7	Polar and 3D far-field radiation patterns of gold nanodisks in array configuration	
	with different lattice periods: a) 400 nm, b) 500 nm, and c) 600 nm. All	
	patterns are plotted at their respective resonance wavelengths. Simulations	
	performed using COMSOL Multiphysics	47
3.8	Workflow of the nanofabrication process based on electron beam lithography	
	to manufacture the gold nanoantenna array.	48
3.9	Dose test. a) Pattern designed in KLayout software. b) Optical microscope	
	image of the exposed dose test	40

3.10	Photographs of the fabricated device. a) Substrate featuring the $2 \times 2 \text{ mm}^2$ gold nanoantenna array. b) Rear view of the 3D-printed sample holder with	
3.11	the device installed	51
	view	52
0.12	(b) high-magnification view	53
3.13	Schematics for optical characterization	54
	Setup for optical characterization	54
	Measured transmittance spectra of fabricated nanoantenna arrays	55
4.1	a) Schematic and b) implemented setup for the proof of concept of the device as a index refractive sensor.	60
4.2	Calibration curve of the refractive index as a function of sucrose concentration in DI water. Single measurements; error bars reflect ± 0.0001 RIU resolution.	60
4.3	Transmittance spectra of the nanoantenna array with surrounding medium	00
1.0	of sucrose solutions at different concentrations	61
4.4	Sensitivity curve of the device for refractive index sensing	62
4.5	Determination of the FWHM value for the dip in the transmittance spectrum.	
4.6	Schematic of aptamer-based biofunctionalization of a gold nanodisk. a) Cortisol	
	aptamer application. b) Capturing of cortisol molecules	64
4.7	Schematic of the microspectroscopic setup used in the biosensing experiment	
	for cortisol detection	65
4.8	Setup used for the biosensing experiment to detect cortisol. a) Front view.	
	b) Rear view	66
4.9	Transmittance spectra of the biofunctionalized nanoantenna array for	
	cortisol solutions at different concentrations	67
4.10	Dose-response curve for cortisol detection in the biosensing experiment	68
5.1	Comparison of schematics and micrographs for a) bright field and d) dark	
	field microscopy	71
5.2	Customization of the microspectroscopic setup to dark field transmission	
	setup. a) Illumination configuration. b) Micrograph of the sample	72
5.3	Schematics of the dark field setup used for optoelectrochemical recording	73
5.4	Implemented dark field setup for optoelectrochemical recording	73
5.5	Optoelectrochemical recording: time-dependent scattering signal (orange	
	curve) of the nanoantenna array under the application of a square voltage	- 1
- c	(blue curve)	74
5.6	Schematic of the protocol for the isolation of cardiomyocytes from rats	75
5.7	a) Schematic and b) implemented custom-built platform for experiments with cardiomyocyte cells	76
5.8	Isolated rat cardiomyocytes a) before (at rest) and b) after (contracted) electrical stimulation. The red rectangles indicate the total length of the cells at rest, while the blue rectangles show the new length when the cells	
	are contracted	77
5.9	Schematic of the setup used for the plasmonic-based electrophysiological	
	monitoring of cardiomyocytes	78
5.10	Implemented setup for the plasmonic-based electrophysiological monitoring	
	of cardiomyocytes	78

5.11	Scattering signal in response to the electrophysiological activity of a single cardiomyocyte	79
5.12	Scattering signal in response to the electrophysiological activity of a group of two cardiomyocytes	79
5.13	Validation that the optical far-field response corresponds to the electric field generated by the cardiomyocytes and not to the external stimulation. Control measurements without cells show no modulation (blue curve), confirming the recorded optical signal arises from cellular activity	80
5.14	Comparison of optical signals corresponding to the electrophysiological activity and contractile movement of cardiomyocytes. The curves are presented without normalization to allow for direct comparison of signal intensity	81
6.1	Integrated microfluidic platform with the nanoantenna array. a) Components.	
6.2	b) Visualization of the device, highlighting its scale	86
6.3	image after the PEDOT:PSS coating	87 88
A.1	General scheme of the integrated optical biosensor based on the comparison	1.0.1
A.2	a) Top view of the coupling system. Percentage of power coupled from fiber to non-linear taper as a function of the length of the taper sections for	
A.3	b) TE ₂ , c) TE ₄ and d) TE ₆ modes	

List of Tables

4.1	Refractive indices of aqueous sucrose solutions	61
4.2	Performance metrics of plasmonic refractive index sensors	63
5.1	Overview of plasmonic nanoantenna arrays for electrophysiology: experimental	
	context and spatial precision.	82

List of Abbreviations

AFM Atomic Force Microscopy

AP Action Potential

BCI Brain-computer interfaces

CCD Charge-Coupled Device

CE Counter Electrode

CEB Center for Biomedical Engineering

CFM Materials Physics Center

CVP Chemical Vapor Deposition

DF Dark Field

DIPC Donosti International Physics Center

eSEM Environmental Scanning electron Microscope

EBL Electron Beam Lithography

ECG Electrocardiography

EEG Electroencephalography

EFP Extracellular Field Potential

ELISA Enzyme-Linked Immunosorbent Assay

EMG Electromyography

FDTD Finite Difference Time Domain

FEM Finite Element Method

FIB Focused Ion-Beam

FOM Figure of Merit

FOV Field of View

FWHM Full Width at Half Maximum

GEVI Genetically Encoded Voltage Indicator

IBL Ion Beam Lithography

IPA Isopropyl Alcohol

ITO Indium Tin Oxide

LEEDS Laboratory of Electrochemistry, Electroanalytics and Sensor Development

LoD Limit of Detection

LPCV Laboratory of Cardiovascular Research

LSP Localized Surface Plasmon

LSPR Localized Surface Plasmon Resonance

MEA Microelectrode Array

MIBK Methyl IsoButyl Ketone

NA Numerical Aperture

NANORIGO Nanotechnology Risk Governance

NIR Near Infrared

NNI National Nanotechnology Initiative

OoC Organ-on-a-Chip

PDMS Polydimethylsiloxane

PLA Polylactic Acid

PMMA PolyMethyl MethAcrylate

PoC Point-of-Care

PVD Physical Vapor Deposition

RE Reference Electrode

RF Radio Frequency

RIU Refractive Index Unit

R&D Research and Development

SEM Scanning Electron Microscopy

SLR Surface Lattice Resonance

SPP Surface Plasmon Polariton

STM Scanning Tunneling Microscopy

UV Ultraviolet

WE Working Electrode

List of symbols

Ø	Diameter
γ	Damping coefficient
ε	Permittivity of the surrounding medium
$arepsilon_D$	Real part of the dielectric constant of the surrounding medium
$arepsilon_{\infty}$	Relative permittivity at the high frequency limit
λ	Wavelength
λ_{LSPR}	Resonance wavelength
Λ	Lattice period
$ ho_n$	Radial coordinate
σ	Standard deviation of noise level
σ_s	Surface charge density
σ_{scat}	Scattering cross-section
ϕ_n	Angular coordinate
ω	Frequency
ω_{LSPR}	Resonance frequency
ω_P	Plasma frequency
c	Speed of light in vacuum
C_{suc}	Sucrose concentration
d	Minimum distance
d_{TF}	Thomas-Fermi screening length
d_{TF}^{Au}	Thomas-Fermi screening length in gold
e	Elementary charge
E	Electric field
E_{cell}	Electric field generated by cells

- $|E|^2$ Enhancement factor
- I Light intensity through a sample
- I_0 Light intensity through a reference
- L Geometrical factor
- m Effective electron mass
- n_{clad} Cladding refractive index
- $n_{sucrose}$ Sucrose refractive index
- n_{water} Water refractive index
- N_{Au} Electron density of gold
- r^2 Coefficient of determination
- S Sensitivity
- S_c Scattered light
- S_{c0} Scattered light without applying an external electric field
- t Time
- Transmitted light
- T_0 Transmitted light without applying an external electric field
- T_1 Local maximum transmittance value
- T_2 Dip transmittance value
- V_{pp} Peak-to-peak voltage

Summary

1	Intr	roduction	20
	1.1	Nanotechnology	20
	1.2	Nanoantenna-based platform for life sciences	22
	1.3	Motivation, objectives and contribution	24
	1.4	Thesis Organization	25
2	The	eoretical Background	26
	2.1	Plasmonics	26
	2.2	Nanofabrication	28
		2.2.1 Lithography	29
		2.2.1.1 Electron Beam Lithography	29
		2.2.2 Thin film deposition	30
		2.2.2.1 Spin-coating	31
		2.2.2.2 Evaporation	31
		2.2.2.3 Electrodeposition	33
	2.3	Biosensing	34
	2.4	Electrophysiological monitoring	37
3	Eng	gineering of plasmonic nanoantenna arrays	41
Ū	3.1	Working principle	
	3.2	Ŭ. I	43
	3.3	9	48
	3.4	Optical characterization	
	3.5	Conclusions	
4	Bios	sensing	59
_	4.1	9	59
	4.2	<u>.</u>	63
	4.3		68
5	Elec	ctrophysiological monitoring	70
		1	70
	5.2		75
	5.3	· · ·	83
6	Con	nclusions and future perspectives	84
	6.1		84
	6.2		86

1		٦
- 1	ľ	

References		89
Appendix A	Supplementary chapter	100
Appendix B	What not to do: common mistakes	105
Appendix C	List of publications	108

Chapter 1

Introduction

Since the late 1960s, when the first research into nanoparticles expanded, there has been great interest in their applications across diverse fields, including health, energy, electronics, and computing [1]. Nowadays, nanotechnology has achieved the status of one of the critical research endeavors of 21st century [2]. Among the most challenging applications in the field of medicine, nanoparticles are utilized for drug delivery, cancer treatment, medical imaging, antimicrobial agents, and diagnostic tools [3]. In this work, we aim to study and implement arrays of nanoparticles in order to apply them for biosensing and monitoring electrophysiological activity. In essence, a novel nanodevice was developed for two primary purposes. Firstly, for detecting specific molecules in the body, such as cancer biomarkers, pathogens (bacteria, viruses and fungi), certain hormones, and other important biological substances. Secondly, for recording the electrical activity of single or very few cells, such as cardiomyocytes in the heart or neurons in the brain. The achievement of these two applications with a single device constitutes the main contribution of this work from scientific, engineering and medical perspectives.

1.1 Nanotechnology

Nanotechnology involves the design, manipulation, and application of materials and devices at the nanoscale, typically ranging from 1 to 100 nanometers, which is approximately 10,000 times smaller than the diameter of a human hair [4]. The concept is commonly attributed to the Nobel Laureate physicist Richard P. Feynman, who introduced it in his famous lecture titled "There's Plenty of Room at the Bottom", presented at Caltech in 1959 [5].

In his talk, Feynman discussed the manipulation and control of matter on an extremely small scale [6]. He wondered about the possibility of writing and reading at the atomic level, storing information on minuscule scale and miniaturizing the computer. Evaporation of materials was also proposed as a technique for manufacturing the exceedingly fine elements of the next generation of devices. He was inspired by the marvelous biological

system, when he realized the amount of things that are done by cells, not just storing information, but manufacturing various substances and transporting them on a very small scale. He even suggested rearranging atoms to manipulate the properties of materials.

While Feynman was a visionary proposing a new field of science, implementing his proposals was extremely difficult at the time, due to the lack of sophisticated equipment and techniques to manipulate matter at the nanoscale. Actually, Feynman himself acknowledged the necessity of better electron microscopes capable of imaging atoms [6]. The first Scanning Electron Microscope (SEM) was developed in 1942, utilizing a beam of electrons to provide information about surface topography and composition [7]. Although it offered superior resolution compared to optical microscopes, it fell short of Feynman's ambitions.

It was not until the 1980s that the development of Scanning Tunneling Microscopy (STM) and Atomic Force Microscopy (AFM) allowed the study of structures with very few nanometer dimensions [8,9]. Both powerful techniques, complementary to SEM, enabled imaging surfaces at atomic resolution. STM operates based on the principle of quantum tunneling and provides information about topography and electronic properties. AFM operates based on the interaction between a sharp probe tip and the sample surface, yielding information about topography and mechanical properties.

Furthermore, at that time advancements in nanofabrication techniques were crucial for achieving the manipulation of materials at the extremely small scale proposed by Feynman [10]. Another key factor supporting the realization of Feynman's predictions was the significant advancement of computational models driven by increasingly robust hardware.

Nowadays, nanotechnology represents a megatrend for both research and industry and has become a general-purpose technology [11]. Due to its tremendous potential and applicability in various fields, from biomedical innovations to space exploration, nanotechnology investments have been increasing worldwide over the years. The United States of America has been a strong investor in this area since 2001 through the National Nanotechnology Initiative (NNI). With a budget of US\$1.99 billion in 2023, the NNI focuses on diverse areas including nanoscience, device development, and addressing global challenges like COVID-19 [12]. Similarly, the European Union has the Horizon Europe program called Nanotechnology Risk Governance (NANORIGO), complemented by two other programs: Gov4Nano and RiskGONE. The main goal of these initiatives is to guide all stakeholders in the sustainable development of nanotechnologies in Europe. NANORIGO, launched in 2019 with a duration of 50 months and a budget of $\in 4.7$ million, is a significant part of these efforts [13]. Japan and China, the two Asian giants, are also heavily investing in nanotechnology, with budgets of 19.74 trillion yen in 2021 and one billion yuan from 2012 to 2017, respectively [14, 15]. In Brazil, from 2003 to 2019, the government invested R\$ 600 million in nanotechnology, focusing on forming research networks, supporting

various laboratories and projects, promoting international cooperation projects, knowledge dissemination and business events [16]. It is worth noting that global investment in nanotechnology is not only for technological development but also for research into the ethical, environmental and health implications.

The biomedical field is among the most impacted by nanotechnology [2]. The scale and novel properties of nanomaterials enable their interaction with biomolecules, organelles and small biological systems as illustrated in Fig. 1.1. This new approach offers a wide range of tools and applications in drug development, medical diagnostics, disease treatment, personalized medicine, and more. Despite being a relatively young field, nanotechnology is rapidly growing due to collaborative efforts among researchers from diverse disciplines such as chemistry, physics, engineering and biology. These unprecedented multidisciplinary collaborations aim to address complex healthcare challenges and transform lives worldwide.

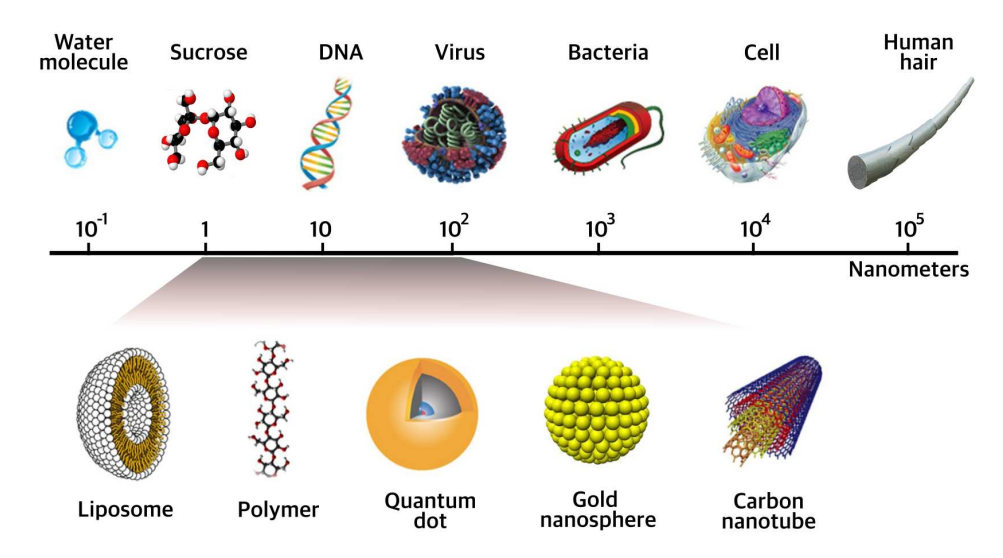


Figure 1.1: Scale comparison between nanostructures and biological features (adapted from [17]).

1.2 Nanoantenna-based platform for life sciences

This doctoral thesis lies at the intersection of nanotechnology and life sciences. Figure 1.2 presents a schematic illustration of the proposed platform, which is based on plasmonic nanoantenna arrays designed for two major subfields within the life sciences: medical diagnostics and the investigation of cellular dynamics.

Specifically, the device developed in this work consists of a square periodic array of gold nanodisks fabricated on a transparent substrate. These nanodisks function as optical antennas: when illuminated with an appropriate light source, they concentrate electromagnetic energy at the nanoscale due to plasmonic resonances. This effect makes them extremely sensitive to changes in the surrounding environment, such as variations

in biomolecule concentrations or the electrical activity of excitable cells. The modulated electromagnetic energy, influenced by these biological or chemical phenomena, is then scattered back into free space. This scattered light can be collected and analyzed optically, enabling both quantitative and qualitative measurements in a fully wireless manner.

For example, when this nanoantenna-based platform is placed in the brain, the nanodisks can be functionalized to detect neurotransmitters such as dopamine and simultaneously monitor the electrical activity of neurons, as illustrated in Figure 1.2. Similarly, when applied to the heart, the same platform could be used to detect trace concentrations of cardiac biomarkers such as troponin — used for myocardial infarction diagnostic — and to monitor the electrical behavior of cardiomyocytes.

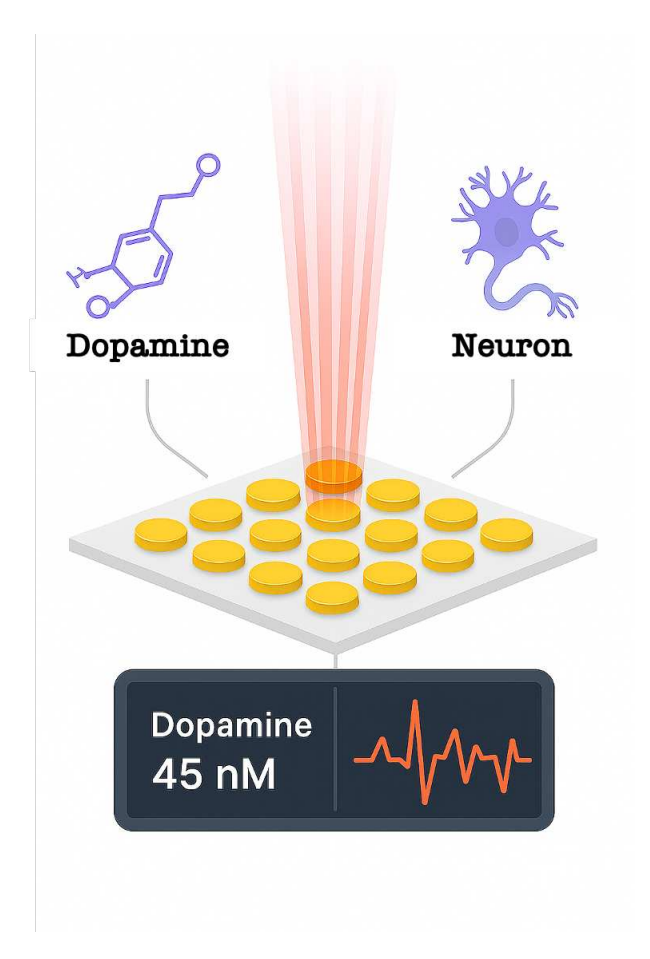


Figure 1.2: Schematic illustration of the nanoantenna-based platform for biomolecule detection and cell monitoring.

Other potential molecular targets include cancer biomarkers, hormones, and viruses, while additional excitable cells of interest encompass skeletal muscle cells, endocrine cells (found in adrenal glands and pancreatic islets), and epithelial cells (such as hair cells in the inner ear). Being able to measure slight changes in the concentration of specific molecules in the cellular environment while monitoring the electrical activity of these cells would represent a significant advancement in our understanding of biological systems at a very small scale, particularly at the level of individual or small cell populations.

1.3 Motivation, objectives and contribution

Understanding how the human brain operates is one of the greatest current scientific challenges [18]. Furthermore, while our knowledge of the heart has advanced considerably, it remains a subject of ongoing research, with many aspects still not fully understood [19]. In this sense, the motivation of this work is to assist the development of novel tools for studying these organs. From our perspective, optical probes based on plasmonic nanoparticles represent highly promising candidates for investigating these organs and others due to their high sensitivity, reliability, spatio-temporal resolution, low-invasiveness, label-free operation and wireless capabilities.

In this context, the main objective of this project is to design, fabricate and characterize a nanodevice based on plasmonic nanoantenna arrays to enable the study of organs, such as brain and heart, in two aspects: biosensing molecular composition and monitoring electrical activity. To achieve this purpose, the following specific objectives have been pursued:

- Design a suitable array of plasmonic nanoantennas to operate in the first biological window of the near-infrared band.
- Fabricate the device based on lithographic nanofabrication techniques.
- Optically characterize the device to verify its operation in accordance with the design.
- Establish collaborations with chemistry and biomedical research groups to conduct experiments involving biosensing and electrophysiological recording.
- Implement a robust measurement setup to detect target molecules and record bioelectrical signals, integrating optical, electrical, chemical and biological techniques.

As mentioned above, plasmonic nanoparticles are being utilized in numerous applications in biomedical research such as sensing, stimulation, imaging, drug delivery, etc. However, to the best of our knowledge, no device has been created for two different applications. In this work, we have developed a single nanodevice capable of functioning as both a biomolecular sensor and an electrophysiological probe. This represents a significant contribution, as it enables more comprehensive analysis of cellular dynamics from a research standpoint, and improves diagnostic capabilities for clinical applications.

Furthermore, as far as we are aware, this study provides the first demonstration of plasmonic nanoantennas functioning as an electrophysiological probe in *ex-vivo* experiments using cells isolated from adult animals, representing more realistic scenarios. This unprecedented achievement also marks an important contribution of this doctoral thesis, as previous works have mainly focused on *in-vitro* experiments involving cell cultures maintained under controlled laboratory conditions [20–23].

1.4 Thesis Organization

This thesis is organized as follows:

In **Chapter 2**, a review of basic concepts is presented, covering plasmonic fundamentals and the current state-of-the-art. In addition, some nanofabrication techniques are briefly described, focusing on those utilized in this project. Concepts of biosensing and electrophysiological recording are also explained, as they are the final applications of this work.

Chapter 3 is the most comprehensive chapter covering the entire development process of the proposed device. First, the principle of operation of the plasmonic nanoantenna arrays is described. Subsequently, the design procedure is explained supported by numerical simulations. Experimental activities are also reported in this chapter, including the manufacture in clean rooms and the optical characterization of the device. From these results, some conclusions are presented.

In Chapter 4 and 5, the applications of the developed device are demonstrated. Each chapter begins by detailing the configuration and operation of the experimental setups. Chapter 4 focuses on biosensing, where the proof-of-concept is validated using the device as a sucrose sensor, followed by the demonstration of its biosensing functionality through the detection of the cortisol hormone. Chapter 5 explores electrophysiological monitoring, presenting the proof-of-concept by recording an external electric field with the nanoantenna array and subsequently demonstrating the device's capability to monitor the electrophysiological activity of rat cardiomyocytes. Each chapter concludes with a summary of key findings.

In Chapter 6, the overall conclusions of this work and the perspectives for future research arising from the results presented here are discussed.

Supplementary Chapter presents a separate project on integrated photonic biosensors undertaken during the doctoral program. This work proposes a pigtailed optical biosensor based on interferometric multimode waveguide and image processing. The sensing performance is evaluated as a sucrose sensor, similar to the developed plasmonic device, but with experimentally obtained refractive index values transferred to a simulated environment. The main contribution of this device lies in being designed as a genuine Point-of-Care (PoC) platform, considering essential features for operation outside laboratories.

Finally, a **list of common mistakes** and **publications** are provided to enhance understanding and offer additional resources for further exploration and improvement.

Chapter 2

Theoretical Background

2.1 Plasmonics

Diffraction limit is one of the major obstacles to the widespread adoption of photonics, since it makes it difficult to use light in integrated circuits, unlike modern electronics. This limitation restricts the confinement of electromagnetic waves to nanoscale regions significantly smaller than the wavelength of light in the material [24]. Plasmonics is a research field that studies and applies the interaction of light and free electrons at the interface between conductors and dielectrics [25, 26]. When plasmonic devices are irradiated by adequate electromagnetic energy, they create local hot spots of electric field, enhancing light-matter interactions by several orders of magnitude [27].

Materials with negative dielectric permittivity are the most convenient to exploit this phenomenon overcoming the diffraction limit and localizing electromagnetic energy into nanoscale regions [24]. Noble metals such as gold - considered a standard for biomedical applications -, silver, copper, platinum and platinoids are the most used materials for this purpose.

Surface plasmons can take various forms and are, therefore, classified into two different types: surface plasmon polaritons (SPP) and localized surface plasmon polaritons (LSP). The former are propagating bound oscillations of electron and electromagnetic waves at a metal-dielectric interface [28]. While the latter are basically standing waves formed by electron oscillations tightly confined on sub-wavelength metallic nanoparticles [29]. The proposed project intends to use this last plasmonic mode, exciting it with incident light that resonates with these electron oscillations.

Plasmonic nanoantennas refer to plasmonic nanostructures due to an analogy with the well-known much larger radio frequency antennas [30]. In general, these devices consist of a metallic conductor, where, under certain conditions, electric currents generate radio waves that propagate through space [31]. In the same way, plasmonic nanoantennas are capable of confining and enhancing the electromagnetic energy from an incident

excitation and, subsequently, radiating it back to free-space with high efficiency [32]. This exceptional property is based on the strong coupling of free electron oscillations in metals to free-space [30]. Furthermore, the great advantage of these plasmonic nanoantennas is that both near-field and far-field radiation are extremely useful for various applications. Near-field energy is commonly used for ultra-high-resolution microscopy and SERS (Surface-Enhanced Raman Spectroscopy) [33–35], while far-field scattering can be used for wireless electrophysiological signal detection [20–23, 36–38], as is done in this project.

During the last two decades, a variety of plasmonic nanoparticles with different shapes and configurations, which support LSP, have been developed. Fig. 2.1 shows a set of geometries that includes nanopillars, cylinders, triangles, stars, cages and polyhedral, and also their respective optical response. To date, the development of these devices, especially of gold, is being pursued in studies ranging from basic research in biology and chemistry to medical applications [3, 39].

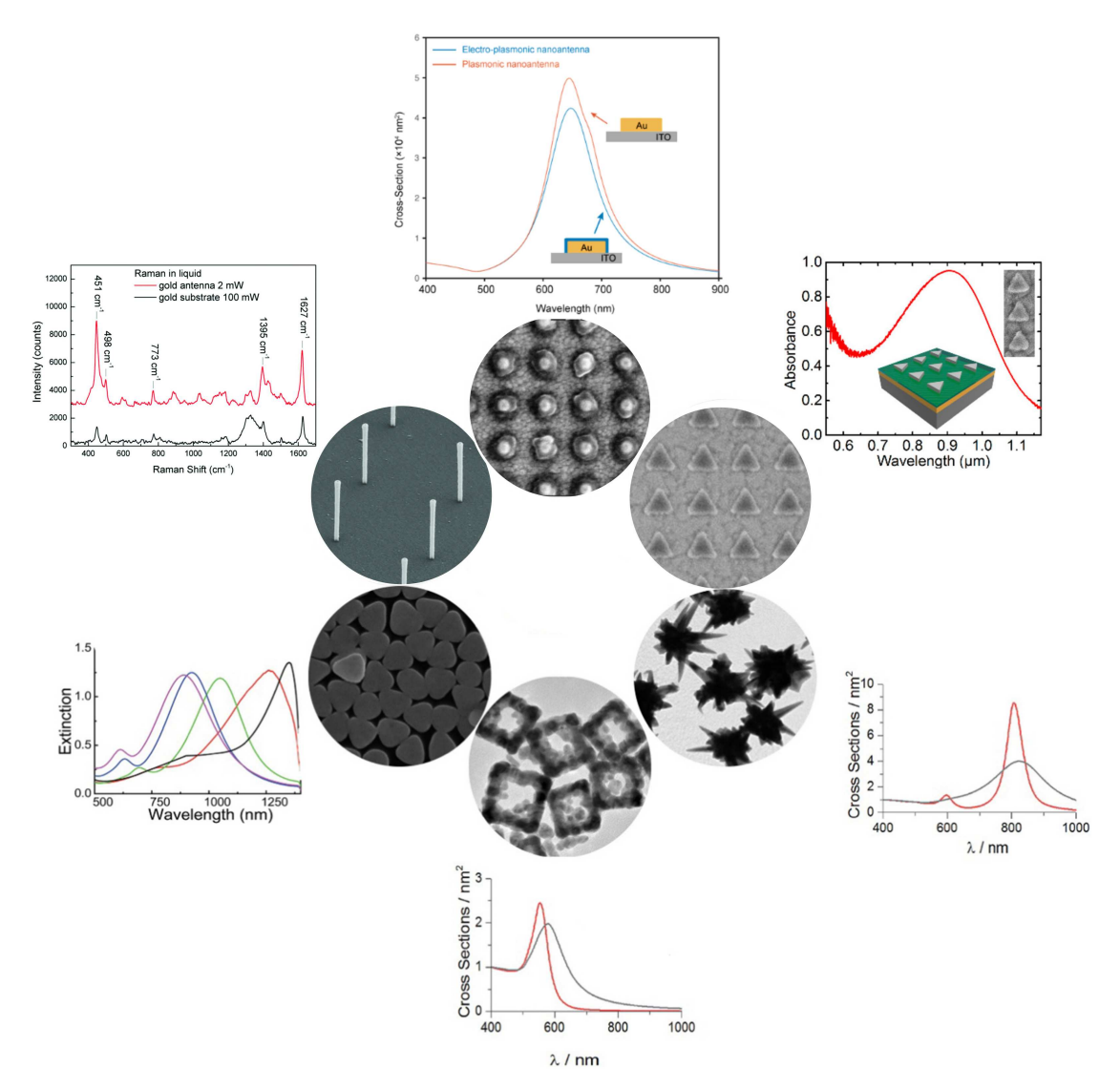


Figure 2.1: Plasmonic nanostructures: Electron microscopy images and corresponding optical responses (adapted from [3, 20, 37, 40]).

2.2 Nanofabrication

Despite the fact that plasmonics began to be studied in the early 20th century and achieved significant progress throughout the following decades, poor manufacturing techniques did not allow its application at the nanometric level [41]. More recently, the development of nanofabrication techniques, such as electron beam lithography, ion beam milling, and self-assembly, has been coupled with the emergence of powerful electromagnetic simulation tools and modern nanocharacterization techniques. This has led to a growing interest in this area and its nanoscale applications [42].

In general, micro and nanofabrication technology consists of the sequential execution of processes and steps. The current procedures were inherited from the processes developed in the semiconductor and integrated circuits industry [43]. Thus, lithography, thin film deposition and etching are the most common techniques to manufacture micro and nano structures [44]. Besides, the wide range of processes and materials available allows the fabrication of a huge variety of devices.

As illustrated in Fig. 2.2, nanofabrication techniques can be broadly categorized into two main approaches based on their starting point and process: top-down and bottom-up [45]. In the top-down approach, larger structures or materials are progressively patterned to create nanostructures. This method offers precise control over shapes, sizes, and locations. Conversely, the bottom-up approach involves building nanostructures by assembling individual atoms or molecules into desired configurations. It relies on self-assembly, molecular synthesis, and chemical reactions to form nanostructures from the ground up. While bottom-up methods are often cheaper, faster, and scalable to higher volumes compared to top-down approaches, they may lack precision. Some techniques, such as epitaxial crystal films, represent a hybrid of both approaches.

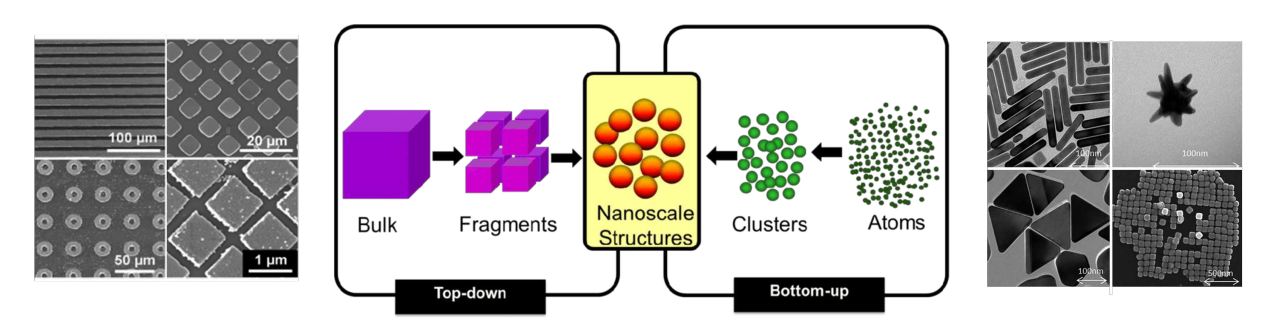


Figure 2.2: Nanofabrication approaches: top-down and bottom-up.

For the fabrication of the device implemented in this project, primarily topdown techniques, also known as micromachining, were employed. Below, some of these nanofabrication techniques are described, focusing on those used in this work.

2.2.1 Lithography

Lithography is the most widely used process for manufacturing micro and nanostructures. For many years, it has played a relevant role in microelectronics industry and, more recently, in nanotechnology [46]. This process is arguably one of the most expensive, requiring equipment that range from a few million dollars in a standard R&D laboratory to hundreds of millions in a foundry [45].

In general, lithography is used to transfer copies of a pattern onto the surface of a material. This technique can be applied with masks (photolithography) or maskless [43]. In the first case, photons coming from a UV light source pass through the mask and incident on a photosensitive resist, causing changes in its chemical properties. Subsequently, the resist is developed, removing either the exposed or unexposed areas and leaving behind the desired pattern. This approach allows the production of several structures simultaneously using the same mask. However, conventional photolithography equipment has a resolution of a few micrometers or - in the best case - several hundred nanometers, which complicates its use for the manufacture of nanostructures. On the other hand, maskless non-optical lithography techniques involve direct writing on the resist for pattern transfer, typically using charged beams. This approach is worthwhile when only a few amount of samples are required. Techniques include Electron Beam Lithography (EBL), Ion Beam Lithography (IBL), Nanoimprint Lithography (NIL), among others.

2.2.1.1 Electron Beam Lithography

Electron beam lithography consists of a beam of electrons that are accelerated to tens of kilovolts and focused to a small spot to induce localized chemical modification in the resist, tracing out the projected pattern. Depending on the type of resist (positive or negative), either the modified or non-modified areas are washed away during the development process, leaving the pattern defined [47]. One of the most common positive resists is Polymethyl Methacrylate (PMMA). When exposed to electron beams, PMMA molecules undergo fragmentation into smaller fragments. These smaller molecules become soluble in a solvent such as Methyl Isobutyl Ketone (MIBK), while the unexposed areas remain insoluble. In contrast, negative resists like SU-8 undergo a cross-linking reaction when exposed to electron beams, which increase their molecular network and decreases their solubility in the developer [45].

The EBL equipment consists of an electron gun, high-voltage accelerator, focusing optics, beam apertures, and deflectors all enclosed in a vacuum chamber, as shown in Fig. 2.3. The beam is electronically deflected by the coils to write the pattern [45]. The main attributes of this technique are the precise control of energy and dose, the ability to accurately record small areas of a substrate, not requiring a physical mask, the low defect densities and the large depth of focus [43]. The obtainable feature resolution of EBL is

between 10-20 nm and it is not limited by diffraction because the quantum mechanical wavelengths of high-energy electrons are extremely small. Thus, the resolution is primarily determined by the tendency of electrons to scatter - rather than remaining accurately parallel - as they travel through the resist. This phenomenon is called the proximity effect and it is responsible for the exposure of undesired areas [47].

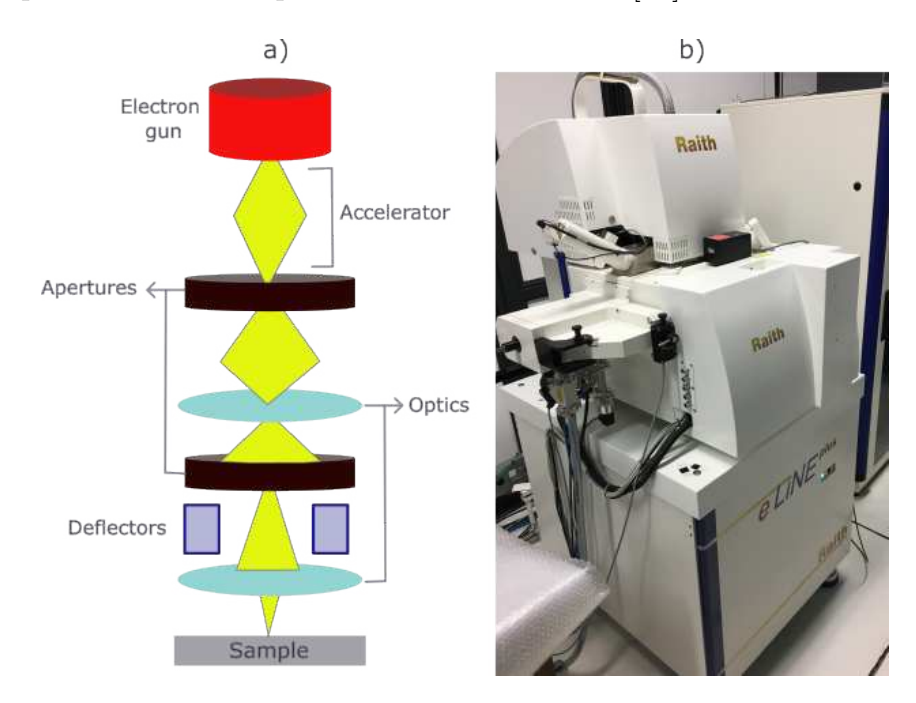


Figure 2.3: Electron beam lithography. a) Schematic diagram. b) Equipment.

2.2.2 Thin film deposition

The addition of materials, predominantly metals and dielectrics, onto a substrate is a broad and fundamental aspect of nanofabrication. Thin films serve various purposes, such as functional (conductive or insulating), sacrificial, and protective layers. Numerous techniques are used for depositing different types of materials to tailor the electrical, optical, chemical, and mechanical properties of a substrate surface. The selection of the deposition process depend on the material and functionality required for the device being manufactured. Generally, deposition processes can be categorized as physical or chemical [44]. Physical methods involve transferring the target material from a specific source to the substrate. These techniques include spin-coating and physical vapor deposition (PVD) methods such as evaporation and sputtering. Conversely, chemical methods entail the formation of solid materials on the substrate through chemical reactions. Processes in this category include electrodeposition and chemical vapor deposition (CVD) methods. The deposition processes employed in this work are detailed below.

2.2.2.1 Spin-coating

Spin-coating is a straightforward and widely employed technique for depositing liquid materials onto a flat surface. The process involves dispensing the resist onto the center of the substrate, which is secured by a vacuum chuck on a motorized rotating stage. Subsequently, the sample is rotated at high speeds to uniformly spread the material across the entire surface. The equipment used for this process is known as a spinner, and the deposited materials usually consist of electro and photoresists. These resists are organic polymers typically dissolved in a liquid solvent. The thickness of the film obtained is directly proportional to the material viscosity and inversely proportional to the rotation speed. Fig. 2.4 illustrates the operation of a spin coater.

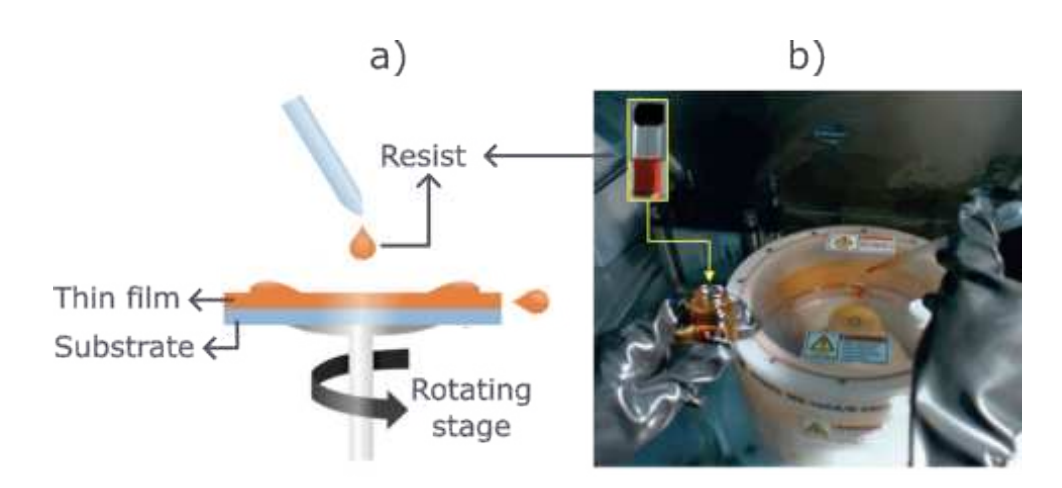


Figure 2.4: Spin coating process. a) Schematic of the operating principle. b) Spin coater. (Adapted from [48]).

2.2.2.2 Evaporation

Generally, this process is used for the deposition of conductive materials such as metals. The process consists of heating a solid source material to be deposited in a vacuum chamber containing the substrate. The goal is to elevate the temperature of the material to create a high enough vapor pressure that can condense on the substrate as a thin film [45]. Once evaporated, the material expands, and it is deposited throughout the chamber and the substrate, at a controlled rate. Vacuum is essential to ensure that atoms of the material move freely, thus they condense uniformly across the entire surface of the substrate. The energy source employed for vaporization is the main distinction between the different PVD techniques. They include resistor, electron beam, radio frequency and laser [43].

2.2.2.2.1 Resistive evaporation

In this method, the material in the form of pellets is placed on a "boat", which is a tungsten or molybdenum sheet or a wire basket. Then, a large DC current is applied through the boat to increase its temperature. Tungsten and molybdenum have a high melting temperature and low vapor pressure, so they generally do not deform or evaporate. However, due to their low resistance, a very large current (around 100 A) has to be supplied to create the required heating power [45].

2.2.2.2 Electron beam evaporation

In e-beam evaporation, the material is also used in pellet form, but it is placed in a crucible pocket, usually made of copper and lined with graphite, tungsten or molybdenum. Additionally, a tungsten filament is heated to generate a cloud of free electrons. Then, several beam-forming plates redirect the electrons away from the filament, and deflectors focus the electron beam toward the center of the crucible [45]. Therefore, the material to be deposited is locally evaporated by the bombardment of high-energy electrons. This makes the process more efficient because the evaporating surface, which is closer to the substrate, has the highest temperature. In addition, the crucible is water-cooled, avoiding the bulk material to reach high temperatures. This method results in better quality films and higher deposition rates than resistive evaporation [43]. However, it is more expensive to install and operate.

Some commercial vendors offer PVD equipment that can perform multiple deposition methods. Fig. 2.5 shows an equipment capable of performing both resistance-heated and e-beam evaporation on the same substrate.



Figure 2.5: PVD75 equipment from Kurt J. Lesker company, used in this work (adapted from [49]).

2.2.2.3 Electrodeposition

In contrast to previous techniques, electrodeposition is a chemical method, thus the deposition on the substrate involves chemical reactions. However, it is important to point out that this is not a CVD technique as it does not use vapor in the process. A large number of materials, such as metals and polymers, can be deposited with this technique. Electrodeposition achieves film thicknesses from a few hundred of nanometers to some millimeters at rates higher than those achieved by vapor methods [50]. The process requires electrically conductive substrates called electrodes, a coating solution containing charged micelles or atoms, and electrical biasing during the deposition process [43]. The electrodes are immersed in the solution, and a voltage is applied between them, generating a current that induces the reduction or oxidation of the ions in the solution. This process occurs on the surface of the substrate, allowing the deposition of small metals or polymer particles onto the sample. This method is simple, but it requires control of several parameters such as solution concentration, pH, temperature, etc.

When the material to be deposited is a conducting polymer, the process is called electropolymerization, which is one of the main topics of modern electrochemistry. The process leads to the formation of organic or organo-metallic films with precise spatial resolution over surfaces. Fig. 2.6 shows the typical setup for this method, which is composed of three electrodes called the working (WE), reference (RE) and counter (CE) electrodes, a source (galvanostatic or potentiostatic), and a solution that contains the monomers of the polymer [51]. The WE exchanges electrons with the solution, thus activating the monomers, while the CE closes the electrical circuit, allowing current to flow between both electrodes. The RE has a well-known electrochemical potential, and therefore, it is used as a reference.

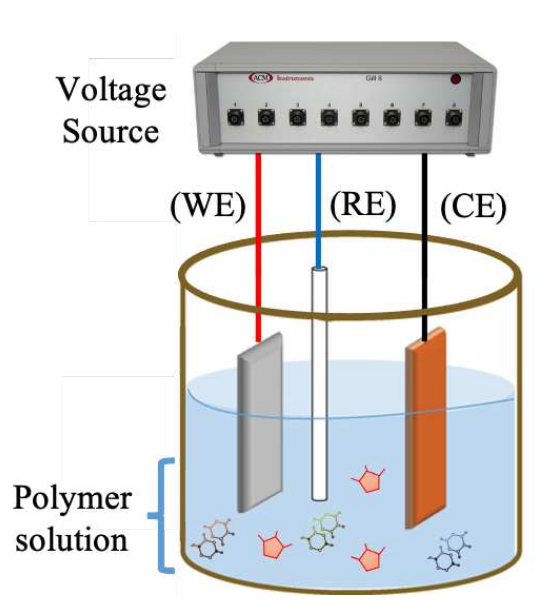


Figure 2.6: Schematic diagram of the electropolymerization setup.

2.3 Biosensing

Biosensing refers to the detection and measurement of chemical compounds in biological samples, typically by electrical, thermal, or optical signals [52]. It consists of three parts: a bioreceptor layer, a transducer, and a user interface, as shown in Fig. 2.7.

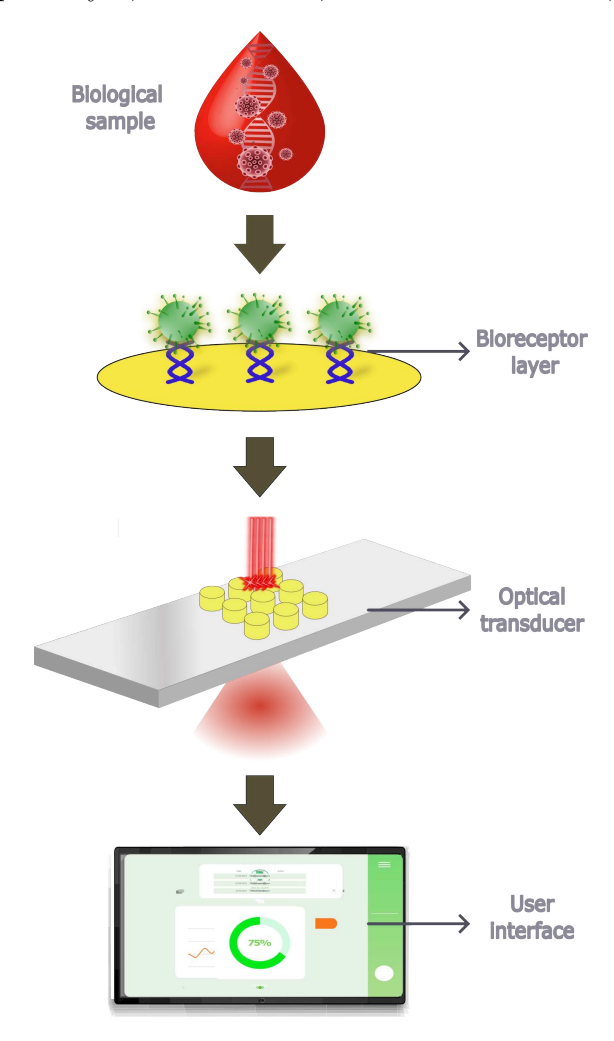


Figure 2.7: General scheme of an optical biosensor.

The bioreceptor layer contains immobilizers, such as antibodies or aptamers, that capture target molecules from a biological sample. This is achieved through a biofunctionalization procedure which involves treating a surface to ensure the binding of specific analytes [53]. The transducer is responsible for converting the biochemical reaction into a detectable signal. There are many types of transducers, such as electrochemical, mechanical, piezoelectric, and optical. An optical transducer translates the capture of the target molecule into a measurable variation of a light property, like phase, polarization, resonance wavelength, or intensity. Biosensors that use optical transducer are called optical biosensors [54]. Finally, the data obtained by the transducer is post-processed and displayed on a user interface. The format of this interface varies depending on the needs of the professional or end-user operating the equipment.

The main desired characteristics of an optical biosensor are [55]:

- **High selectivity and sensitivity**: The ability to exclusively detect the target analyte at the minimum concentration required to diagnose disease and its stage.
- Short response time: Ideally, some minutes or a few hours to have a reliable result, which is crucial for timely treatment.
- Easy to use: The simpler the device, the more personnel can operate it, leading to broader accessibility for diagnosis.
- Capacity for miniaturization: This allows for the development of portable devices that work with low sample volumes. In addition, nanometric scale biosensors can be implanted for *in-vivo* detections.
- **Versatility**: The ability to detect a wide range of analytes or achieve multiple functionalities with the same device.

The performance of LSPR-based biosensors is quantitatively evaluated by analyzing the transmittance spectra, as illustrated in Fig. 2.8. The main parameters used for performance assessment are sensitivity (S), figure of merit (FOM), and limit of detection (LoD). Sensitivity is defined as the ratio between the variation in the optical parameter used for detection and the variation in the cladding refractive index [56], as shown in 2.1. For resonant structures like plasmonic nanoparticles, the optical parameter is typically the resonance wavelength, making sensitivity as shown in 2.2. In other cases, intensities and phases may also be examined to evaluate sensing performance.

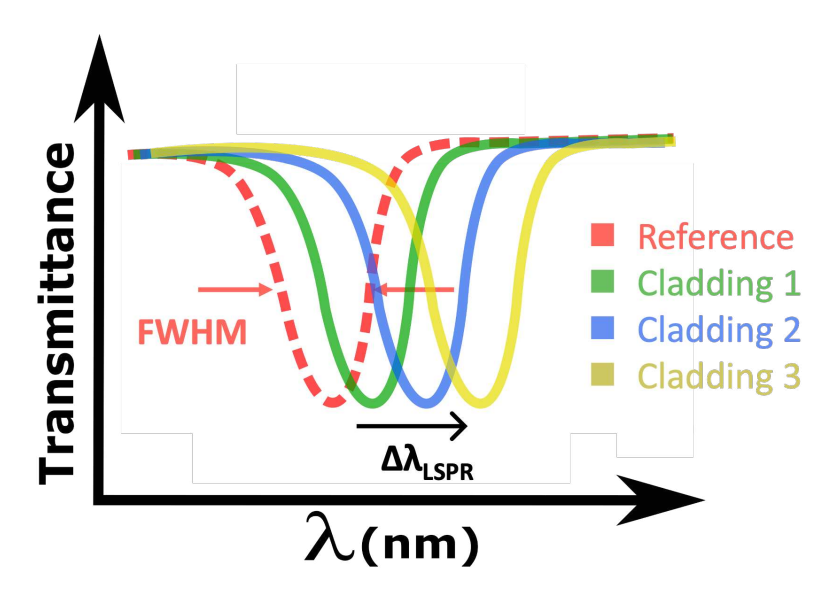


Figure 2.8: Transmittance spectra of an LSPR-based biosensor for detection purposes.

$$S = \frac{\partial(Opt. Param.)}{\partial n_{clad}} \tag{2.1}$$

$$S = \frac{\partial \lambda_{LSPR}}{\partial n_{clad}} \tag{2.2}$$

The figure of merit (FOM) is used to evaluate the device as a refractive index sensor during the proof-of-concept stage, before biofunctionalization. As shown in 2.3, the FOM is calculated as the ratio of sensitivity to the full width at half maximum (FWHM) of the resonance peak or dip [56]. FWHM refers to the width of a spectral peak or dip at half of its maximum or minimum value. In absorption, extinction and scattering spectra, the FWHM is applied to peaks, while in transmittance spectra, it is applied to dips. FWHM is critical in LSPR sensors because it directly influences the FOM. A narrower FWHM results in a higher FOM, indicating better sensitivity to changes in the refractive index. Additionally, narrow resonances allow for more precise determination of wavelength shifts, which is crucial for accurate sensing.

$$FOM = \frac{S}{FWHM} \tag{2.3}$$

Limit of detection is defined as the minimum concentration of the analyte that the device can reliably detect [57]. This parameter is used for evaluating the device as a biosensor after the biofunctionalization procedure. LoD is typically defined as the concentration at which the sensor signal is distinguishable from the noise by a certain factor, often three times the standard deviation (σ) of the noise level. It can be calculated using the dose-response equation, where the variation of the optical parameter is expressed in terms of the analyte concentration. Therefore, the LoD corresponds to the concentration that produces a change in the optical response equal to three times the standard deviation of the noise. A simplified method to calculate the LoD is by using equation 2.4, which is widely referenced in the literature [57,58]. As inferred by the equation, the more sensitive the biosensor, the lower its LoD, meaning it can detect lower concentrations of the analyte. However, if the system is highly noisy, the LoD increases, meaning the device would only be able to detect higher concentrations of the analyte.

$$LoD = \frac{3\sigma}{S} \tag{2.4}$$

The LoD is typically expressed as analyte concentration (e.g., in ng/ml or molarity), or as surface mass density (e.g., pg/mm^2). This value is not directly comparable among different sensors because it depends on the target molecule and its affinity constant.

2.4 Electrophysiological monitoring

Electrophysiological monitoring involves the measurement and analysis of electrical activity generated by living cells [59], particularly from the nervous system, muscles, and heart. This technique is crucial for understanding the electrical properties of these cells and diagnosing various medical conditions.

The electrical activity of neurons, often measured using techniques such as electroencephalography (EEG) or intracranial recordings, provides insights into brain function and disorders. In addition, electromyography (EMG) records the electrical activity of muscles, aiding in the diagnosis of neuromuscular disorders. Electrocardiography (ECG), by contrast, measures the electrical activity of the heart, helping diagnose arrhythmias, ischemia, and other cardiac conditions [60].

The most common method for recording bioelectric activity in the extracellular environment involves using metal electrodes [61]. Microelectrode arrays (MEAs) consist of a grid of small electrodes widely used for mapping brain activity [62] and sometimes for studying the electrical behavior of cardiac cells [63]. However, MEAs have drawbacks, such as the need to connect each electrode to an external processing unit and the high complexity of the electrical circuits required to reduce the footprint, which inevitably lead to unwanted cross-talk and increase impedance and thermal noise [64,65].

In this context, the use of light to probe bioelectrical signals exhibits relevant attributes that are worth leveraging [66,67]. Photons are extremely fast, offers outstanding spatial resolution and multiplexing capabilities, avoid the need for any physical connection with external devices (as light can travel through bones and penetrate tissues), and do not interfere with physiological functions [30,61]. Therefore, optical probes are highly potential candidates for detecting electrophysiological signals with high spatio-temporal resolution, minimal invasiveness, label-free operation, and wireless capabilities.

As discussed in section 2.1, plasmonic nanoparticles are employed in this work for electrophysiological monitoring. The operating principle is based on the modulation of the nanoparticles' scattering signal by an external electric field generated by excitable cells, as illustrated in Fig. 2.9. Initially, at rest, when a plasmonic nanoparticle located in the extracellular medium, close to the cell membrane, is illuminated by a suitable incident light source, localized surface plasmons are excited. This leads to a strong concentration of electromagnetic energy around the nanoparticle, which is then radiated as scattered light. As shown in the bottom left panel of Fig. 2.9 (red curves), the scattered light exhibits a resonant spectra response and a stable time-dependent signal in the absence of cellular activity. Upon stimulation, ionic currents are triggered across the membrane of the excitable cell. In neurons, for instance, the ions that control the membrane potential are sodium (Na^+) and potassium (K^+) . Large variations in charge density cause a high transient electric field, which can be measured as an action potential (AP) across the

membrane ($\sim 10^5$ V/cm) [68,69], or as an extracellular field potential (EFP) right outside the cell ($\sim 10^3$ V/cm) [70,71]. These biological low-frequency electric fields alter the local dielectric environment of the nearby plasmonic nanoparticle, leading to a measurable optical response. As illustrated in the bottom right panel of Fig. 2.9 (blue curves), this response manifests as a spectral shift and amplitude modulation in the time-dependent scattering signal, confirming the sensitivity of the plasmonic probe to electrophysiological activity.

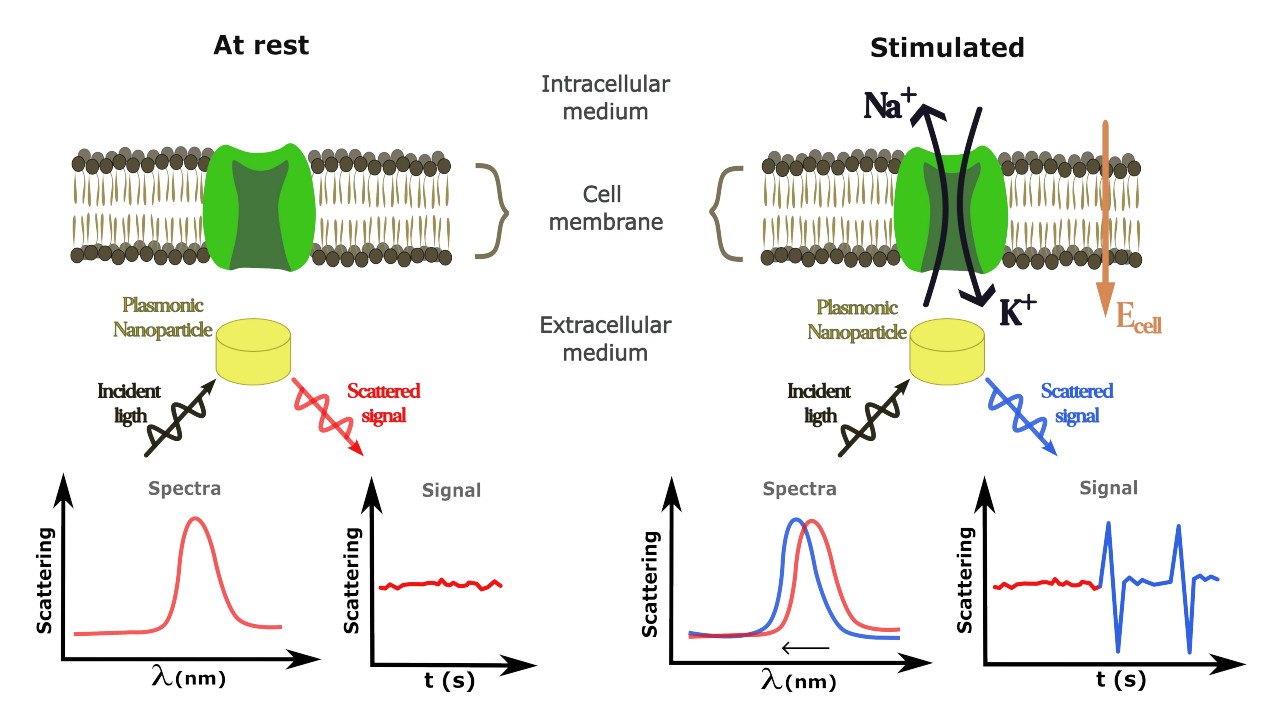


Figure 2.9: Operating principle of nanoantennas as electrophysiological probes.

To describe the changes in the scattering signal in terms of variations in the external electric field, a quasi-static model is used [20,21]. First, an analytical relation for the plasmon frequency modulation as a result of the electric field is demonstrated. Then, the differential scattering signal is approximated using this linear relation.

An external electric field, in this case generated by a cell, induces a surface charge density at the gold surface

$$\Delta \sigma_s = -\varepsilon E \tag{2.5}$$

where ε is the permittivity of the surrounding medium.

In a conductor, free electrons move in response to an external electric field, rearranging themselves to reduce the field within the material. This rearrangement is known as screening, and it is mathematically described by the Thomas-Fermi model. The Thomas-Fermi screening length (d_{TF}) is a distance over which the electric field is attenuated in a conductor due to the presence of free electrons. Assuming the change in the surface charge density $(\Delta \sigma_s)$ of the gold nanoparticles is localized in the Thomas-Fermi

region, the change in the electron density can be written as

$$\Delta N_{Au} = -\frac{\Delta \sigma_s}{e d_{TF}^{Au}} \tag{2.6}$$

where e is the elementary charge and d_{TF}^{Au} is the screening length in gold.

The modulation of the electron density results in a change in the gold plasma frequency, which are related by

$$\omega_P = \sqrt{\frac{e^2 N_{Au}}{\varepsilon m}} \tag{2.7}$$

where m is the effective electron mass.

Thus, a linear relationship between the variation of plasma frequency due to charge density changes can be established

$$\Delta\omega_P = \frac{\omega_P}{2N_{Au}} \Delta N_{Au} \tag{2.8}$$

In addition, the dielectric function of gold is described by the Drude model

$$\varepsilon(\omega) = \varepsilon_{\infty} - \frac{\omega_P^2}{\omega(\omega + i\gamma)} \tag{2.9}$$

where the constants ε_{∞} and γ are the relative permittivity at the high frequency limit and the damping coefficient, respectively. Using this equation, the LSPR frequency can be found considering the resonance condition

$$Re[\varepsilon(\omega_{LSPR})] = \frac{\varepsilon_D(L-1)}{L}$$
 (2.10)

where ε_D is the real part of the dielectric constant of the surrounding medium and L is a geometrical factor [29].

Thus, the resonance frequency of the plasmonic nanoparticle can be written as

$$\omega_{LSPR} = \sqrt{\frac{\omega_P^2}{\varepsilon_\infty + \varepsilon_D \left(\frac{1-L}{L}\right)} - \gamma^2}$$
 (2.11)

and the resonance frequency modulation due to changes in plasma frequency of the gold surface is given as

$$\Delta\omega_{LSPR} = \frac{\omega_P}{\omega_{LSPR} \left(\varepsilon_{\infty} + \varepsilon_D \left(\frac{1-L}{L}\right)\right)} \Delta\omega_P \tag{2.12}$$

Combining equations 2.5, 2.6, 2.8 and 2.12, the resonance wavelength shift as a result of an external electric field can be expressed as

$$\Delta \lambda_{LSPR} = -\frac{\omega_P^2 \lambda_{LSPR}^3}{8\pi^2 c^2} \frac{1}{\left(\varepsilon_\infty + \varepsilon_D \left(\frac{1-L}{L}\right)\right)} \left(\frac{\varepsilon}{e N_{Au} d_{TF}^{Au}}\right) E \tag{2.13}$$

where λ_{LSPR} is the LSPR wavelength and c is the speed of light in vacuum. The negative sign represents the blue shift of the scattering spectrum as a result of the stiffening of the resonant free electron spring.

As mentioned above, once the plasmon frequency modulation is expressed as a function of the external electric field, the differential scattering signal caused by this spectral shifting can be approximated.

Since the LSPR shift is very small, on the order of 10^{-3} nm for a typical extracellular electric field intensity, the change in the shape of the transmission spectrum can be ignored, and it can be assumed that the entire spectrum shifts rigidly by $\Delta \lambda = \Delta \lambda_{LSPR}$.

Approximating the scattered intensity by

$$S_c = 1 - T \tag{2.14}$$

where T is the transmitted signal of the gold nanoparticle, the differential scattering signal can be calculated by

$$\frac{\Delta S_c}{S_{c0}} = -\frac{1}{1 - T_0} \left(\frac{\Delta T}{\Delta \lambda}\right) \Delta \lambda \tag{2.15}$$

where ΔS_c is the change in the scattered light intensity, $\Delta T/\Delta \lambda$ is the derivative of the transmission spectrum, and S_{c0} and T_0 are the scattered and transmitted signals without an external electric field, respectively.

Therefore, given the transmitted signal and transmission spectrum of the gold nanoparticle, as well as the spectral shifting, it is possible to approximate the variations in the scattered signal caused by an external electric field.

Chapter 3

Engineering of plasmonic nanoantenna arrays

3.1 Working principle

The proposed device consists of a square array of gold nanodisks on a transparent substrate. These nanoparticles function as optical nanoantennas, operating analogously to radio frequency (RF) antennas. They resonate with light waves, enhance local electromagnetic fields, and control light directivity at the nanoscale, in a manner similar to how traditional antennas interact with RF waves.

When the nanoparticle array is irradiated by a suitable light beam, it excites collective oscillations of the electrons at the gold surface, known as localized surface plasmons. This electron cloud formed at the metal-dielectric interface leads to a high concentration of electromagnetic field a few nanometers away from the nanoantenna surface, which is called the near field. The enhanced field in this region is highly sensitive to changes in the surrounding medium, which is leveraged for the two applications of the developed device.

As shown in Fig. 3.1, the array of plasmonic nanoantennas implemented in this work is a dual-purpose device. Firstly, it operates as a biosensor for detecting specific molecules, and secondly, as an electrophysiological probe for monitoring the electrical activity of certain cells. For the first purpose, as a biosensor, the gold nanoparticles were specialized to detect cortisol, often referred to as the "stress hormone". Cortisol is produced by the adrenal glands in response to stress. Low cortisol levels are associated with symptoms such as depression and weakness, while high levels are related to increased blood pressure, weight gain and a higher risk of osteoporosis [72–74]. For the second purpose, as an electrophysiological probe, tests were conducted with isolated rat cardiomyocytes. Cardiomyocytes are the excitable muscle cells of the heart, responsible for pumping blood throughout the body and represent the smallest natural unit capable of responding to field

stimulation [75,76]. Monitoring their electrical activity offers insights into heart function under both normal and pathological conditions, and allows the study of drug and therapy effects. Similar experiments can also be performed with other excitable cells, such as neurons.

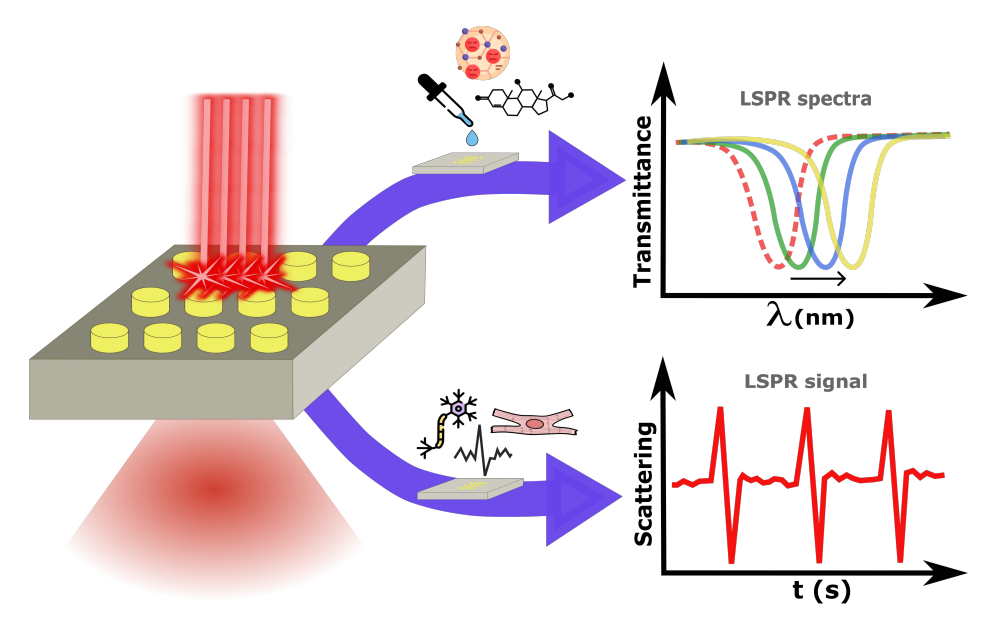


Figure 3.1: Working principle of the plasmonic nanoantenna array as a two-purpose device: biomolecular sensor and electrophysiological probe.

For biosensing application, variations in transmittance are used to detect target molecule at different concentrations. A broadband light beam passes through the nanoparticle array, and the transmitted light is collected by a spectrometer. Due to the excitation of localized surface plasmons, a portion of the incident light is absorbed and scattered at specific wavelengths. In this work, the nanoparticles are large enough for scattering to be the predominant effect over absorption. Consequently, as the scattered light is redirected to different directions, less light is transmitted through the array, resulting in a dip in the transmittance spectrum at the resonance wavelength. When a solution containing cortisol is dropped onto the sensor, the refractive index of the surrounding medium changes, causing variations in the resonance wavelength of the device, which are visualized as a red-shift in the spectrum. Higher concentrations of cortisol result in larger red-shifts in transmittance. By analyzing these shifts in dip position due to changes in analyte concentration, the sensitivity and limit of detection of the biosensor can be calculated.

For monitoring the electrical activity of cells, the time-dependent scattering signal of the nanoantenna array is employed. Similar to the biosensing application, a broadband light beam is used to illuminate the sample, but in Dark-Field (DF) mode. Thus, the beam is manipulated to form a hollow cone, ensuring oblique incidence. This setup allows only scattered light to be collected in the normal direction while transmitted light, which propagates at a certain angle, is avoided. The temporal response of the

plasmonic array is recorded by an optical power meter set at the resonance wavelength. When excitable cells, such as cardiomyocytes, are placed on the sample and properly stimulated, they generate a local electric field that causes a small variation in the resonance frequency of the plasmonic nanoparticles. This effect can be clearly visualized in the time-dependent scattering signal, which is modulated in amplitude by the extracellular field potential of the cardiomyocytes.

3.2 Design of the device

At this stage, design conditions such as the operation wavelength, materials, geometry, dimensions and distribution were defined. The chosen wavelength range for operation is within the first biological window of the near-infrared band (NIR-I), specifically from 650 to 950 nm [77]. Its low reflection from bones and reduced absorption in biological tissues make this band particularly suitable for this application, unlike the visible spectrum. Additionally, near-infrared lasers induce less photo-damage compared to ultraviolet (UV) or visible lasers. Although the project initially aims to perform *in vitro* and *ex vivo* biological tests, the NIR-I band was selected to facilitate future *in vivo* experiments.

For the plasmonic nanoantennas, gold was chosen as the functional material because it is a well-known noble metal with outstanding biocompatible properties, unlike silver, which is cytotoxic and thus unsuitable for use in cell cultures over extended periods [37]. These nanoparticles were arranged on a conductive substrate, enabling the proof-of-concept as an electrophysiological probe, as it functioned as an electrode to which an external electric field was applied. Hence, indium tin oxide (ITO) coated glass slides has been employed as the substrate. In addition, a thin layer of titanium was used to enhance the adhesion of gold to the substrate. Fig. 3.2a illustrates a scheme of the designed device.

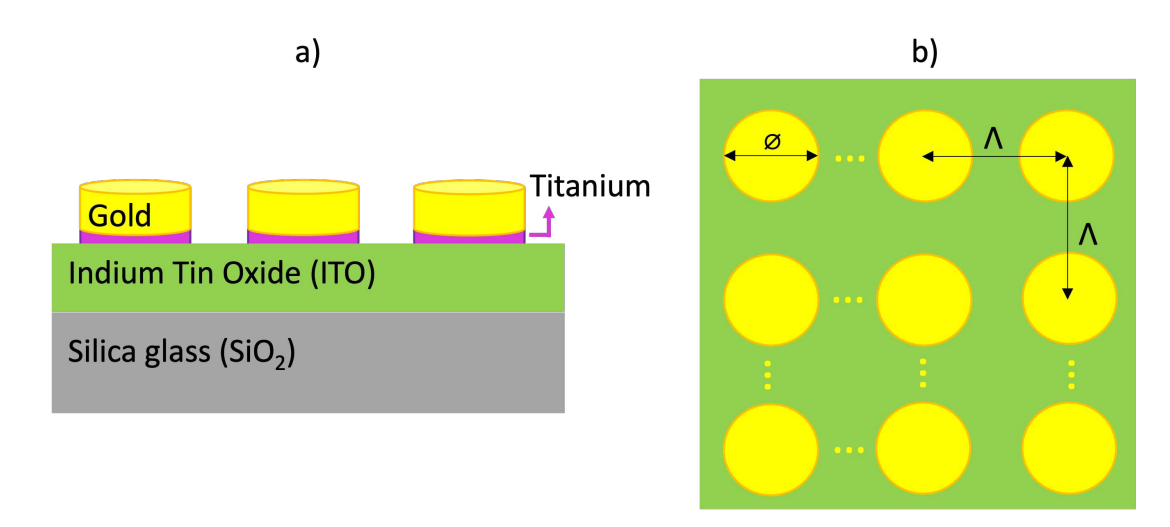


Figure 3.2: Scheme of the nanoantenna array. a) Side view. b) Top view.

Regarding to geometry, nanodisks were employed to simplify the fabrication process, avoiding corners and sharp features that are difficult to achieve by lithographic techniques. Besides, a circular cross-section minimizes the dependence of incident light polarization in the plane transverse to the propagation direction. This shape also allows for the use of suitable boundary conditions to leverage symmetries and reduce simulation resources.

The dimensions and distribution of the nanoantennas (see Fig. 3.2b) were determined using electromagnetic simulations, always taking into account the constraints of available nanofabrication technologies. The nanoantenna single element and the array were modeled using the Finite Difference Time Domain (FDTD) solver from Ansys Lumerical, and the Finite Element Method (FEM) solver from COMSOL Multiphysics, in collaboration with the Materials Physics Center (CFM) and the Donosti International Physics Center (DIPC) in the Basque Country. Targeting a resonance in the NIR-I band, sweeps of diameter (D) and height (H) were performed as shown in Fig. 3.3. The performance parameter was the scattering cross-section, often denoted as σ_{scat} , which is a theoretical area that describes how large a nanoparticle appears to an incoming light wave in terms of its ability to scatter light. As can be seen, the resonance corresponds to the maximum value of the scattering cross-section.

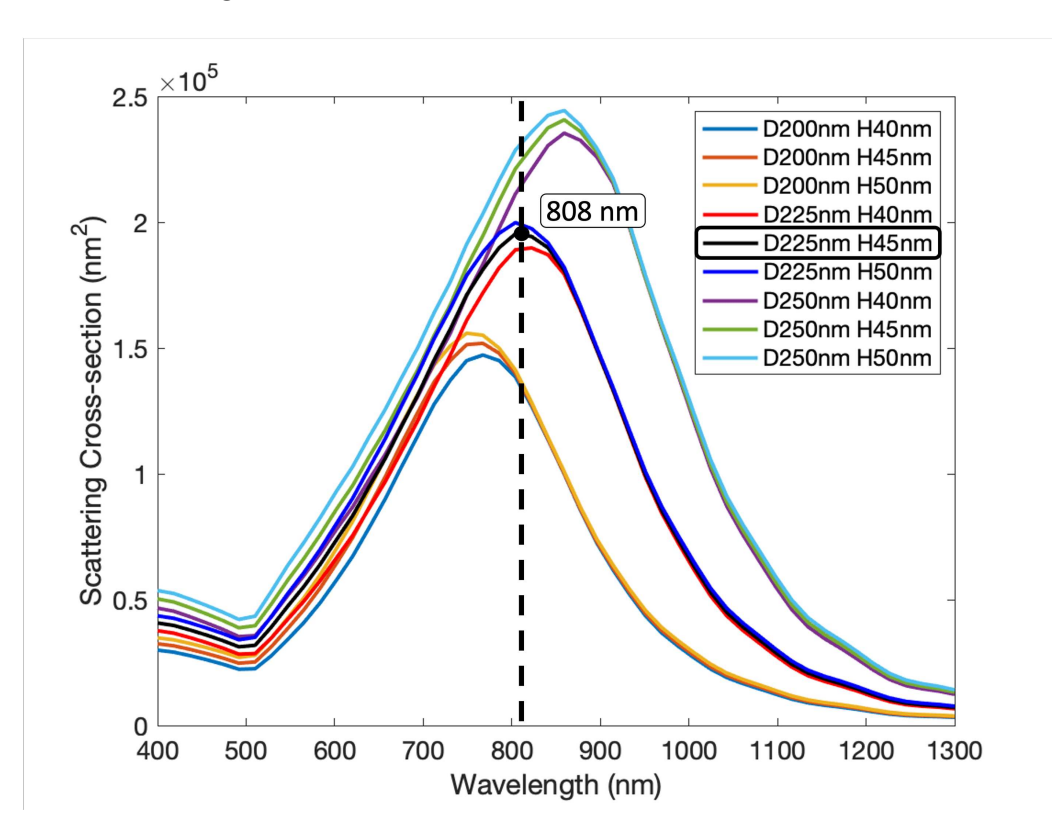


Figure 3.3: Simulated scattering spectra of plasmonic gold nanodisks, obtained with Ansys Lumerical. Sweeps in diameter from 200 nm to 250 nm, and in height from 40 nm to 50 nm.

A nanodisk with a diameter of 225 nm and a height of 45 nm was chosen, showing a broad resonance in the desired band, with a peak around 808 nm, which is a common wavelength for commercial optical sources. Furthermore, the values of the scattering cross-section are exceptionally high, much greater than the typical values of voltage-sensitive dyes ($\sim 10^{-2} \text{ nm}^2$) [20], also used for monitoring the electrical properties of cells. Moreover, considering the resolution capabilities of electron beam lithography and evaporator-based gold deposition, the selected dimensions did not pose a complex challenge.

As explained in the previous chapter, nanoantennas confine and enhance the electromagnetic field within a narrow region surrounding them. Fig. 3.4 illustrates the near-field enhancement of a cylindrical gold nanoantenna. The intensity of the incident field was set to 1 V/m to facilitate the evaluation of the light-matter interaction. Additionally, in accordance with the resonance observed in the scattering analysis, the simulation was conducted at a wavelength of 808 nm. These results around the gold nanodisks demonstrate the plasmon excitations and suggest a high sensitivity of the nanoantennas to detect subtle changes in the surrounding medium.

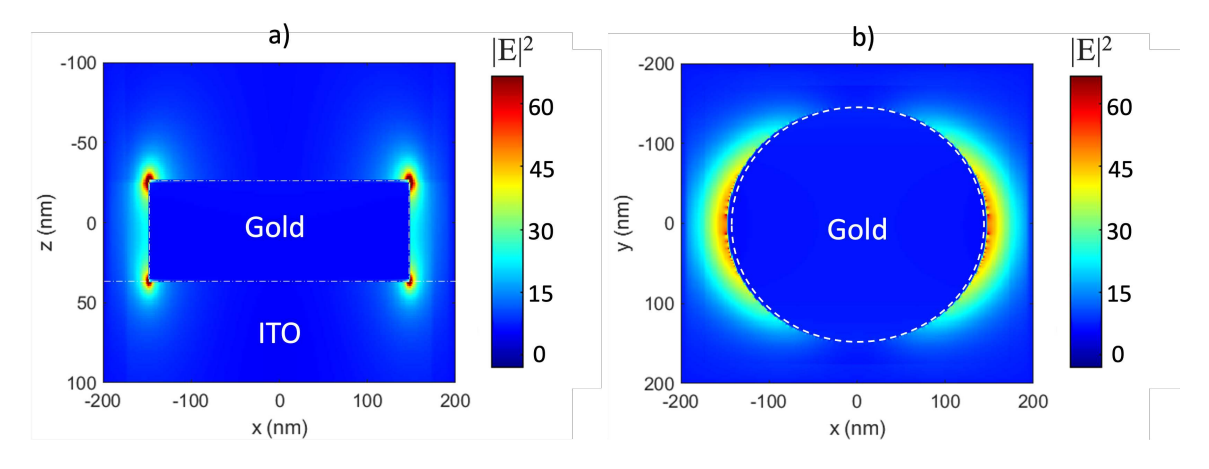


Figure 3.4: Simulated local electric field enhancement of gold nanodisks using Ansys Lumerical. a) Side view. b) Top view.

Uniform arrays of nanoparticles ensure consistent results at different test points on the same device, which improves both repeatability and accuracy. In addition, periodic arrays of plasmonic nanoparticles enhance the performance of LSPR devices, particularly through the phenomenon of Surface Lattice Resonance (SLR). This resonance occurs when the plasmons of individual nanoparticles interact coherently with diffraction orders of the array.

When arranged into a grating, nanoparticles can diffract light in-plane, meaning the light travels tangentially along the grating surface, which is known as the Rayleigh anomaly. This phenomenon causes a sudden drop in transmittance at a specific wavelength. SLR is excited next to Rayleigh anomalies due to the constructive interference of the scattered fields from the nanoparticles. This interaction results in sharper and more intense resonance peaks, as well as higher electromagnetic field enhancement compared to single nanoparticles. By changing the lattice period, the Rayleigh anomaly can be shifted resulting in a tuning of the SLR.

The array of nanodisks was simulated as a square periodic array using the periodic boundary conditions available in the softwares. Fig. 3.5 shows the transmittance spectra of gold nanodisk arrays with periods ranging from 300 nm to 700 nm. The results clearly demonstrate the effect of the lattice period on resonance. As the period increases, the resonance dip becomes narrower and experiences a red-shift. The periods selected for fabrication ranged from 400 nm to 600 nm because, at these values, the resonance dips are sufficiently narrow, have a good amplitude, and remain within the desired band. It is important to note that for biological experiments, a red-shift is expected for all the curves due to the higher refractive index of the predominantly aqueous surrounding medium.

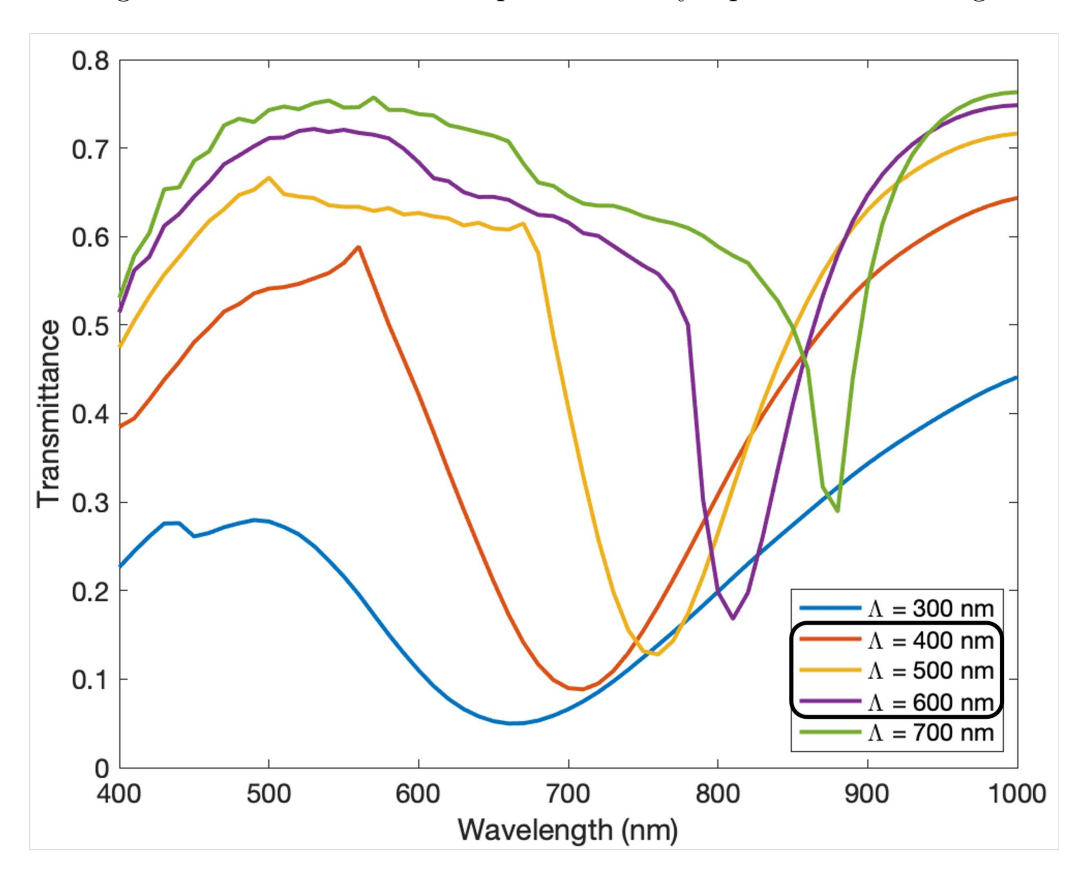


Figure 3.5: Simulated transmittance spectra of a nanoantenna arrays with varying lattice periods. Single element: gold nanodisks with 225 nm diameter and 45 nm thickness. Simulations were performed in COMSOL Multiphysics and validated with Ansys Lumerical.

Fig. 3.6 illustrates the electric field enhancement of the designed gold nanodisk when arranged in an array configuration with the lattice period of 600 nm. As expected, the enhancement factor $|E|^2$ in the array is significantly higher - by a factor of 2.6 - compared to that of an isolated nanoparticle. This increased enhancement is attributed to the collective interactions of the nanodisks within the array, which amplify the local electromagnetic fields more effectively than a single nanodisk alone.

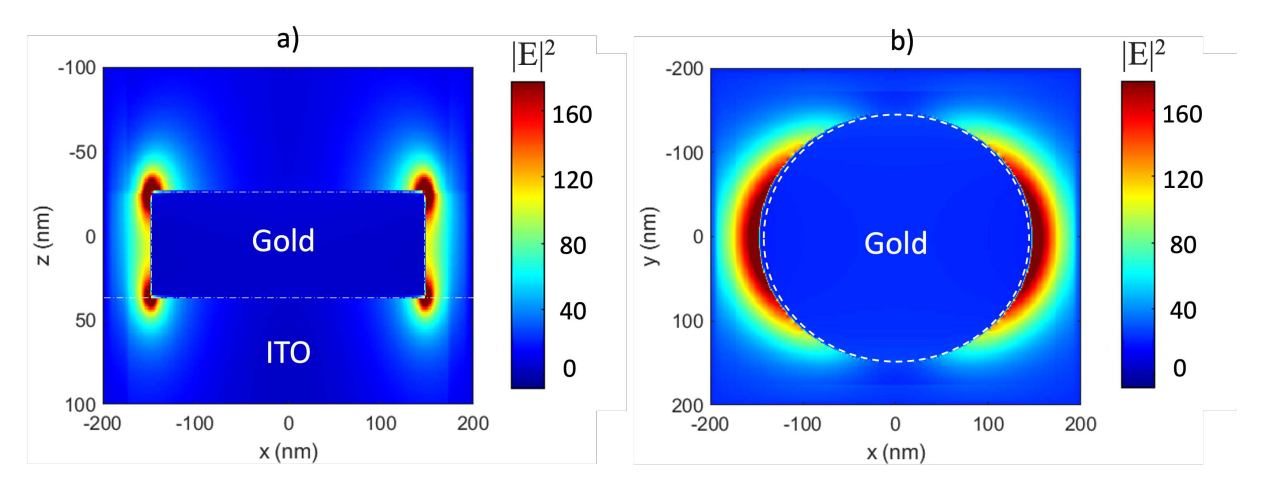


Figure 3.6: Simulated local field enhancement of the gold nanodisks in array configuration using Ansys Lumerical. a) Side view. b) Top view.

Furthermore, the far-field radiation pattern was simulated to analyze the impact of the lattice period on the directivity of the nanoantenna array. Fig. 3.7 illustrates the results for lattice periods ranging from 400 nm to 600 nm, highlighting variations in the directional light distribution. The array was excited by a plane wave incident from above. In addition, considering the experimental setup was designed in transmission mode to collect both transmitted and forward scattered light, the 600 nm lattice period proved to be most suitable. This configuration exhibited minimal reflectivity and maximal transmission, aligning well with the intended experimental design.

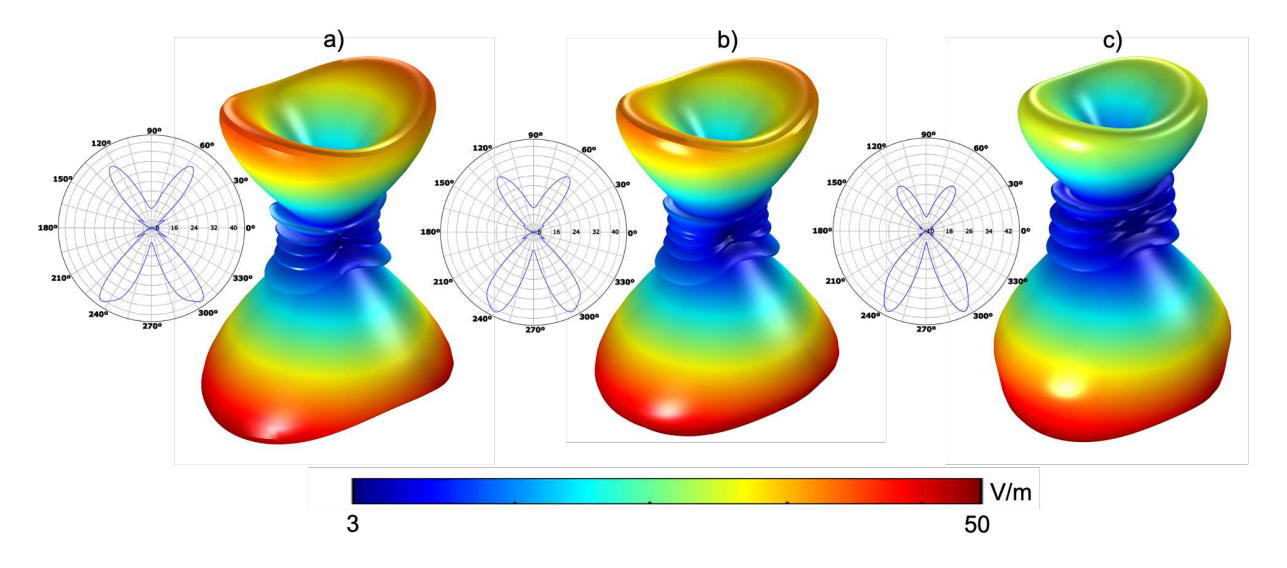


Figure 3.7: Polar and 3D far-field radiation patterns of gold nanodisks in array configuration with different lattice periods: a) 400 nm, b) 500 nm, and c) 600 nm. All patterns are plotted at their respective resonance wavelengths. Simulations performed using COMSOL Multiphysics.

3.3 Fabrication of the device

Gold nanoparticles can be synthesized either via chemical reactions (bottom-up approach) or by lithographic techniques (top-down approach). The latter is particularly suited for creating large and spatially controlled arrays. In this work, electron beam lithography (EBL) was used to fabricate the device designed in the previous section. Fig. 3.8 illustrates the workflow of the fabrication process, conducted in collaboration with the Nanoengineering group led by Prof. A. Seifert at the NanoGUNE research center in the Basque Country.

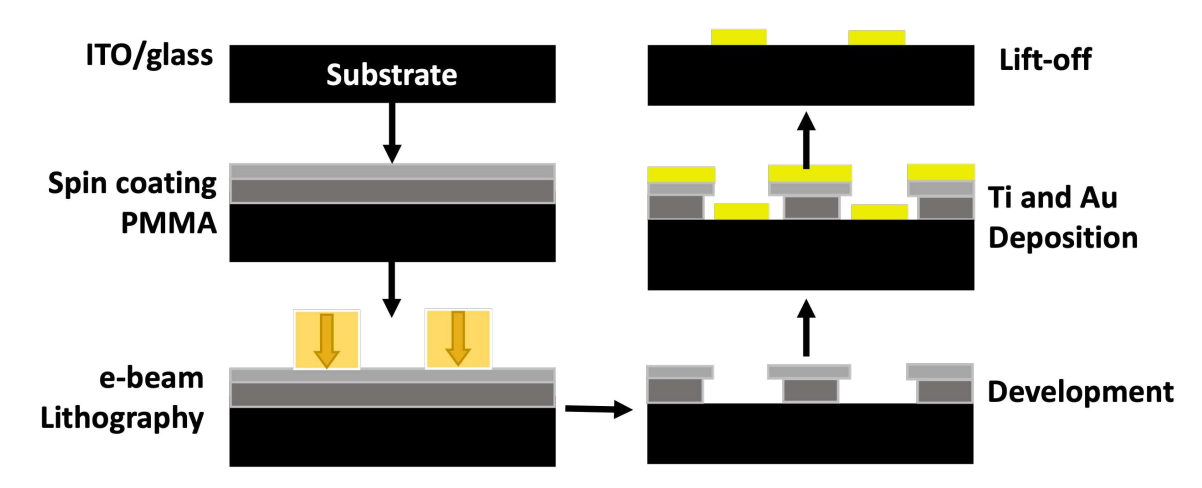


Figure 3.8: Workflow of the nanofabrication process based on electron beam lithography to manufacture the gold nanoantenna array.

ITO-coated soda lime glass (Biotain Crystal Co.) was employed as the substrate. A low resistance of 4 - $5~\Omega/sq$ was chosen to minimize charging effects during EBL, and a high transmittance greater than 83% was opted to facilitate transmission measurements during experiments. Initially, the ITO glass slides were rubbed with a cotton swab and isopropyl alcohol (IPA) to remove surface imperfections from the ITO deposition process. They were then cleaned in ultrasonic bath with acetone and IPA for 5 minutes. After removal from the bath, the slides were dried with a nitrogen jet. A subsequent dehydration step was performed at 180° C for 2 minutes on a hot plate. Finally, oxygen plasma treatment for 5 minutes was applied to remove organic contaminants.

The electron resist was deposited on the clean substrates via spin coating. First, PMMA 495 A4 (MicroChem) was spin-coated at 4,000 RPM for 1 minute and then soft-baked on a hot plate at 180°C for 1.5 minutes. Next, a second PMMA layer was added to create a bilayer resist configuration to ensure high-resolution patterning and enhanced edge definition. Thus, PMMA 950 A2 (MicroChem) was spin-coated and soft-baked under the same conditions as the bottom layer.

The e-beam lithography was carried out using RAITH150 Two system. Dose tests were required to achieve the desired geometry and dimensions. This procedure involved calibrating the exposure dose to determine the optimal electron beam dosage for the designed pattern. Fig. 3.9a shows the layout used for the dose test, where rows correspond to varying diameters of nanodisks and columns refer to the energy delivered per unit area. Each element is a square array of $100 \times 100~\mu m^2$. Fig. 3.9b displays the results after the fabrication process. Lower doses did not sufficiently sensitize the resist, resulting in no patterning, while higher doses did achieve patterning but, in some cases, led to overexposure. The detailed analysis was conducted using Scanning Electron Microscopy (SEM). The dots observed in the image correspond to substrate imperfections, which were removed in subsequent tests by rubbing the slides with a cotton swab and IPA, as previously mentioned.

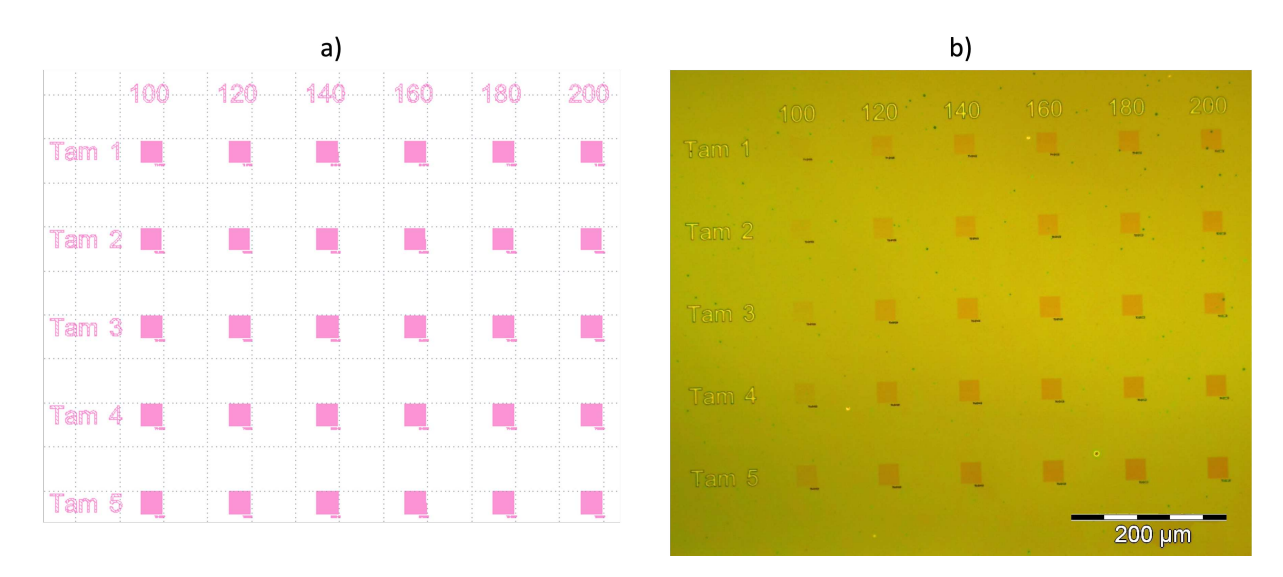


Figure 3.9: Dose test. a) Pattern designed in KLayout software. b) Optical microscope image of the exposed dose test.

After performing the dose tests and optimizations, the main parameters were set as follows:

• Extra High Tension (EHT) or Accelerating Voltage: 10 KV

• Aperture: $30 \ \mu m$

• Area Dose: $100 \ \mu C/cm^2$

• Dose Factor: 1.5

• Step Size: 10 nm

• Beam Speed: 10 - 20 mm/s

The time required to pattern a 2×2 mm² array varied based on the lattice period: for a 600 nm period, the process took 4 hours to pattern over 11 million nanodisks; for a 500 nm period, approximately 6 hours were needed to pattern over 16 million nanodisks; and for a 400 nm period, the patterning took 9 hours to produce more than 25 million nanodisks.

Once the lithography process was completed, the sample was removed for development. This step involved immersing the sample in a 1:3 solution of MIBK (Methyl Isobutyl Ketone) and IPA for 2 minutes to remove the exposed regions of the resist. Subsequently, the sample was rinsed in pure IPA for 1 minute and dried using a nitrogen jet.

The subsequent metal depositions were carried out on the developed substrates using the PVD75 evaporator (Kurt J. Lesker Company). First, a thin titanium layer of 4 nm thickness was deposited using electron beam evaporation at a rate of 0.5 Å/s and at a pressure of 5.7×10^{-6} torr. Next, a 45-nm-thick gold layer was deposited over the titanium layer. This deposition was performed by thermal (or resistive) evaporation at a rate of 0.8 Å/s under the same pressure conditions.

The last step is the lift-off process, which involves removing the PMMA resist layers to leave behind the gold nanoantenna array on the substrate. For this, the sample is taken out of the evaporator and soaked in acetone for 24 hours. Afterward, the acetone is replaced, and the substrate is placed in an ultrasonic bath for 3 minutes. This procedure is then repeated with IPA for another 3 minutes. Following this, the sample is rinsed with water and dried with a nitrogen jet. A final dehydration step is carried out at 100°C for 1 minute, followed by an oxygen plasma treatment for 5 minutes to remove any remaining resist residues.

It is important to highlight that the nanofabrication recipe presented in this work is the result of an extensive and iterative optimization process. Over a period of eight months, sixteen test samples were fabricated to evaluate and refine each step of the fabrication workflow. Several challenges were systematically addressed, including: reducing defects on the ITO substrate through chemical and physical treatments; calibrating the electron beam dose factor and the nanodisk diameter in the design layout to match the intended dimensions; minimizing patterning astigmatism to achieve circular — rather than elliptical — nanodisk shapes; and optimizing the development time to ensure complete resist removal while avoiding the formation of empty sites where nanodisks were unintentionally detached. After this refinement process, the nanodisk removal rate was reduced to just 1%. A list of common mistakes along with recommendations to avoid them is provided in Appendix B.

Fig. 3.10a shows a photograph of the fabricated device, while Fig. 3.10b shows it mounted in a 3D printed sample holder. These pictures indicate that the square array of nanoantennas is easily visible to the naked eye due to its large dimensions of 2×2 mm². In addition, the entire substrate size of 15 mm \times 7.5 mm is convenient for sample manipulation during characterization, and the use of a customized sample holder simplifies handling.

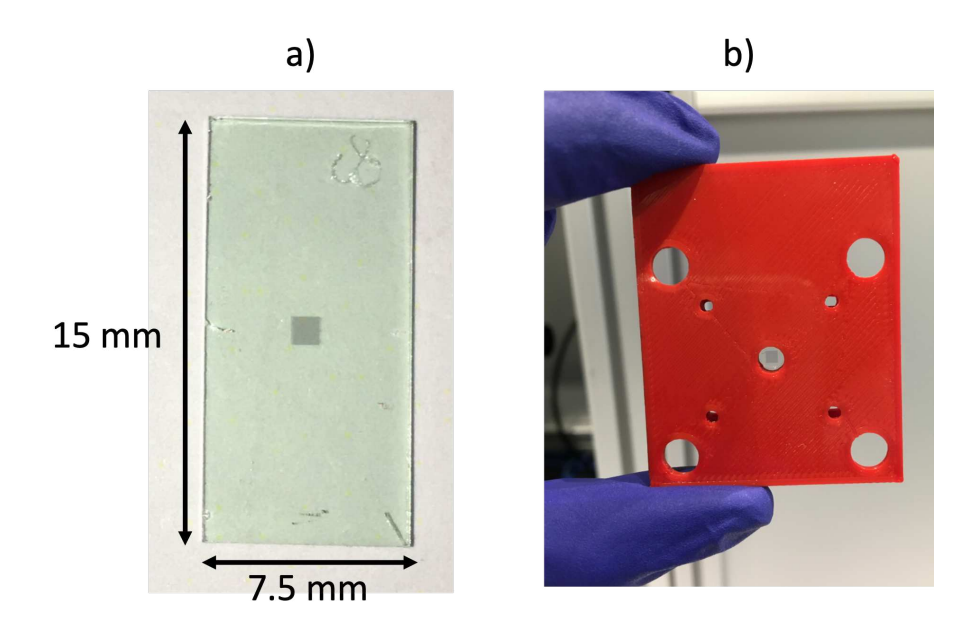


Figure 3.10: Photographs of the fabricated device. a) Substrate featuring the $2 \times 2 \text{ mm}^2$ gold nanoantenna array. b) Rear view of the 3D-printed sample holder with the device installed.

The gold nanodisks in the array were examined using an environmental scanning electron microscope (eSEM-FEI Quanta 250), as shown in Fig. 3.11. The top view analysis confirmed the circular geometry of the nanodisks, with a mean diameter of approximately 225 nm, and verified a uniform distribution across the array. Fig. 3.11a corresponds to a lattice period of 500 nm, one of the configurations studied in this work. To analyze the vertical profile of the nanostructures, the sample was tilted at an angle of 80°, as illustrated in Fig. 3.11b. Although this side-view image reveals that the vertical sidewalls of the nanodisks are not sharply defined — likely due to the inherent roughness of the ITO substrate — the general morphology is preserved. Despite these imperfections, a plasmonic resonant behavior is still expected by the fabricated nanoparticles. Thus, the combined top and tilted views offer a comprehensive morphological assessment, validating the fabrication process and confirming the suitability of the nanoantenna array for its intended optical and biological applications.

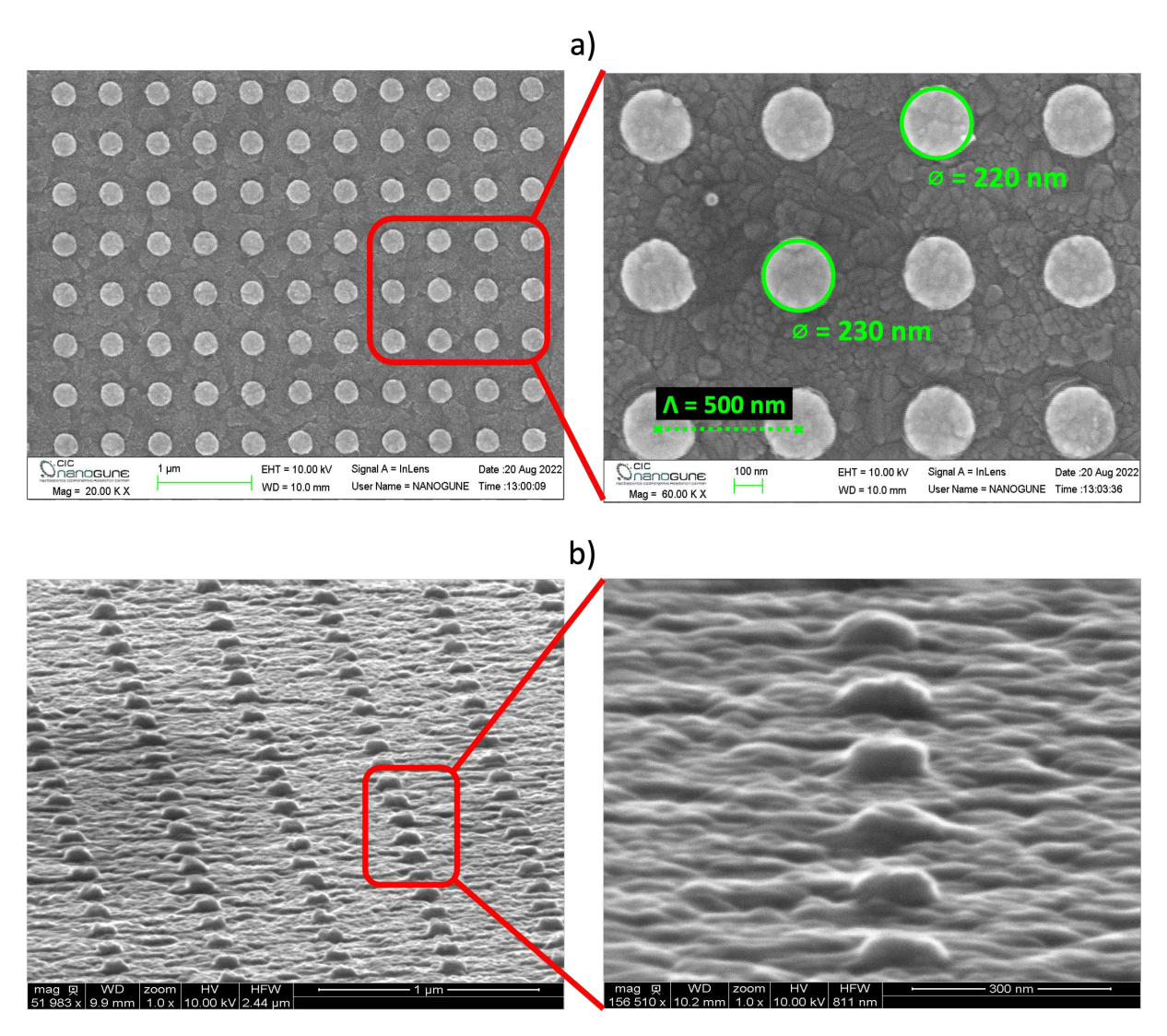


Figure 3.11: SEM micrographs of the fabricated periodic array. a) Top view. b) Tilted view.

An aperiodic array was also fabricated to experimentally analyze the effect of lattice periodicity on the resonance behavior of the device. It is expected that by eliminating periodicity, the response of the array will resemble the pure LSPR spectrum of a single nanoantenna [78], without the SLR effect. Fermat's spiral was chosen for its simple mathematical description, with the following coordinates for the *n*-th element:

$$\rho_n = \frac{d}{d_{14}}\sqrt{n} \tag{3.1}$$

$$\phi_n = n\pi(3 - \sqrt{5}) \tag{3.2}$$

where $d_{14} = \sqrt{5 - 4\cos\phi_3}$, n is the index of the element, and d is the minimum distance between them.

Fig. 3.12 shows the fabricated aperiodic array with the same unit element as the periodic array, a 225 nm-diameter gold nanodisk. In Fig. 3.12a, the complete spiral is shown, with a minimum distance of 400 nm, containing 50,000 elements and covering a total area of $100 \times 100 \ \mu m^2$. Unfortunately, it was not possible to fabricate a larger array due to technical problems with the EBL equipment. Fig. 3.12b shows the central region of the same array at a higher magnification.

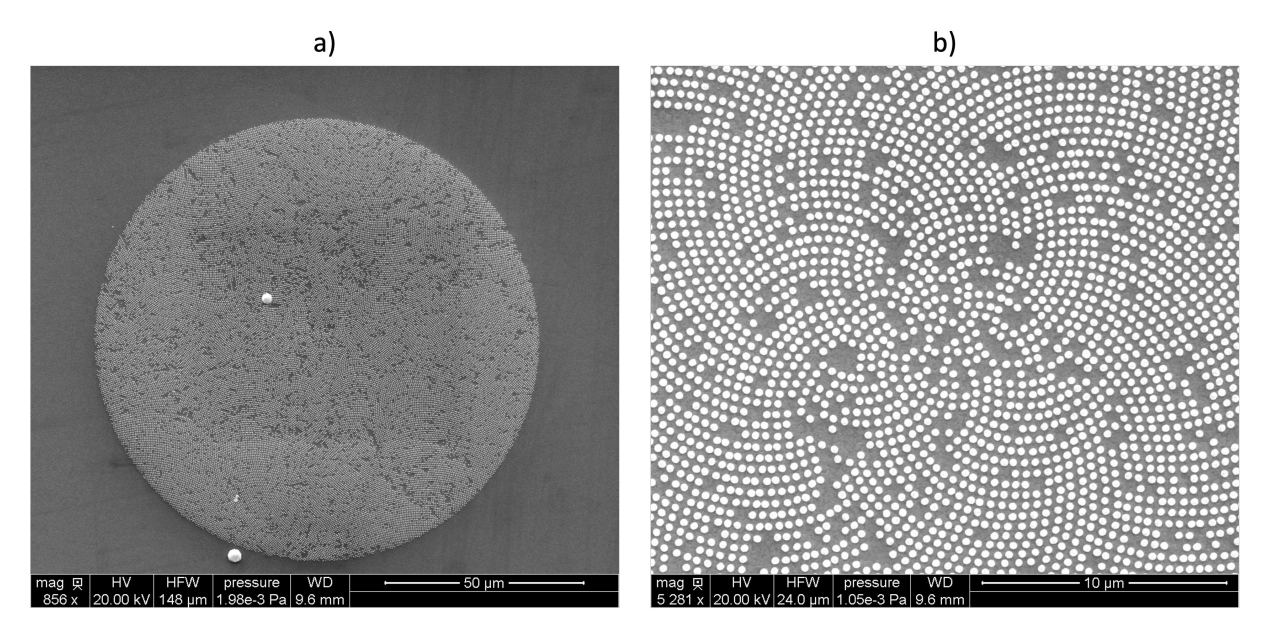


Figure 3.12: SEM micrographs of the fabricated aperiodic array: (a) Entire array and (b) high-magnification view.

3.4 Optical characterization

In this stage, we aimed to measure the resonance of the fabricated nanoantenna arrays in order to verify the occurrence of the expected optical phenomenon, LSPR and SLR, and compare the experimental performance with the results simulated in the design process. A spectroscopic setup in transmission configuration was employed to optically characterize the device, thus transmittance spectrum was used for the analysis.

As shown in the schematic of the Fig. 3.13, the spectroscopic setup consisted of a white-light source, a collimator, a pinhole, an objective lens and a spectrometer. The source was a tungsten-halogen lamp (SLS201L, Thorlabs) with a band ranged from 360 nm to 2,600 nm which has a divergent beam that was directed towards the collimator (LC-075, Newport) to align the light rays to be parallel to each other, reducing their divergence. Then, a pinhole was placed to limit the amount of light interacting with the sample for ensuring it illuminates precisely the region of the array and avoiding the saturation of the detector. The sample was placed in a 3D-printed sample-holder to facilitate the manipulation. Subsequently, the transmitted light was collected by an objective lens

(RMS40X, Olympus) and a 400- μ m multimode optical fiber patch cable. Finally, the collected light was measured using a fiber-coupled CCD spectrometer (CCS175, Thorlabs) ranged from 500 nm to 1,000 nm. This was connected to a personal computer with the suitable software for data analysis and visualizing the transmittance spectrum. Fig. 3.14 shows the implemented optical characterization setup.

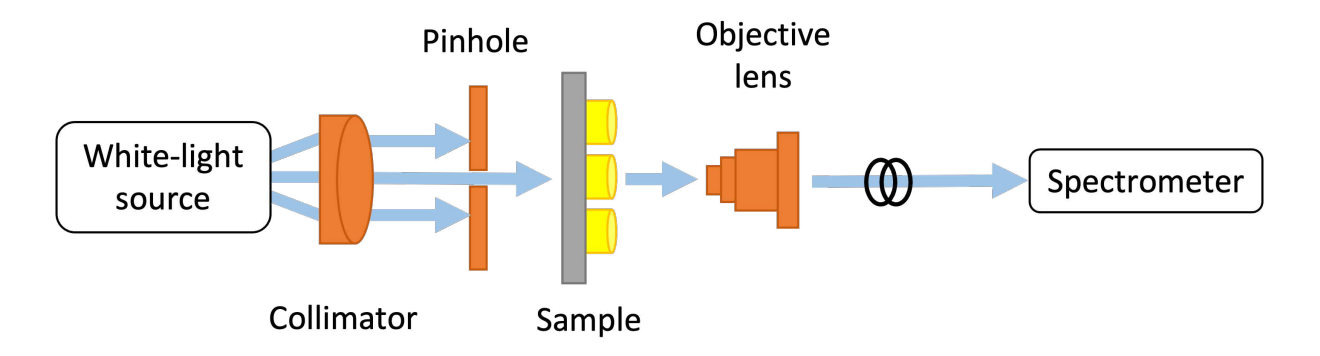


Figure 3.13: Schematics for optical characterization.

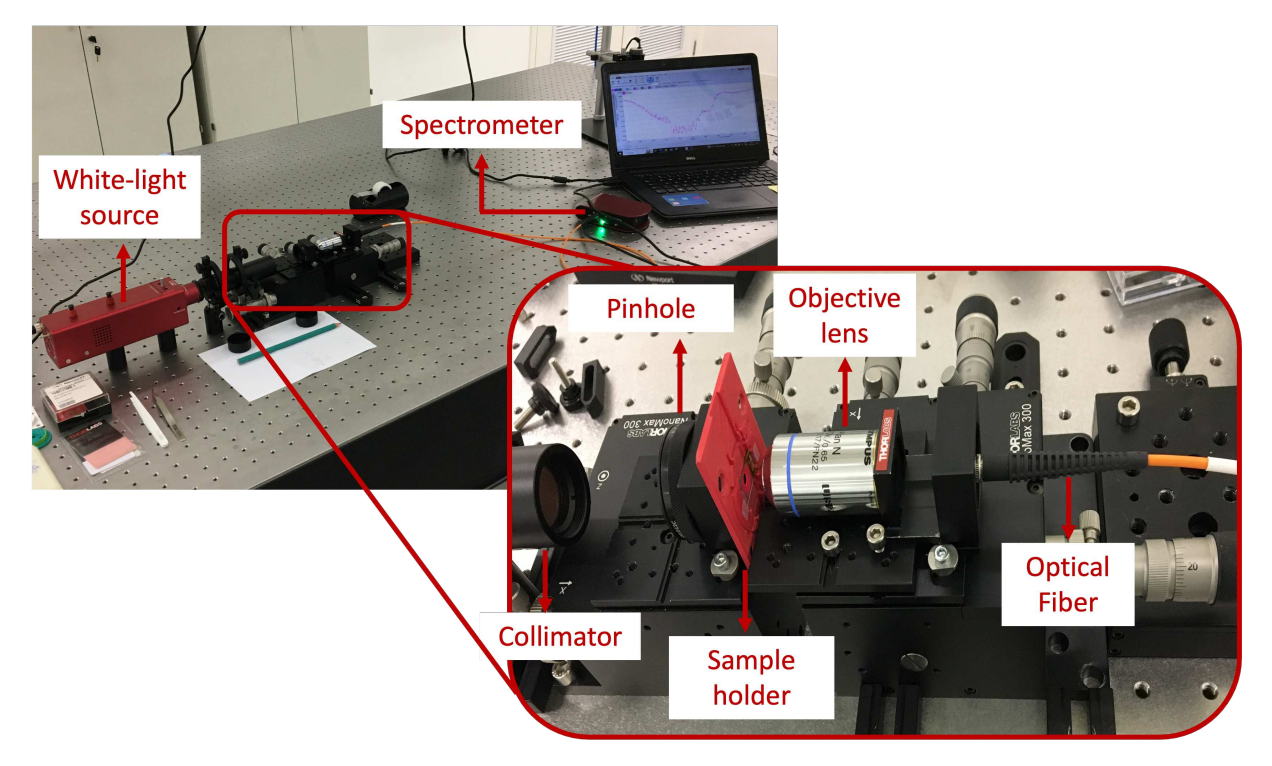


Figure 3.14: Setup for optical characterization.

As shown in 3.3, transmittance is a relative measurement that consists of a ratio between the light intensity passing through the sample (I) and the light intensity passing through a reference (I_0) , commonly called the blank. In this work, the sample refers to the fabricated nanoantenna array, whereas the blank is either a separate ITO-coated glass slide or the unpatterned region of the same sample.

$$T(\lambda) = \frac{I(\lambda)}{I_0(\lambda)} \tag{3.3}$$

Fig. 3.15 shows the transmittance spectra measured for each fabricated nanoantenna array. As explained in the design and fabrication sections, the samples consist of arrays of gold nanodisks with a diameter of 225 nm and a height of 45 nm. The aperiodic array consists of a disordered arrangement using a Fermat's spiral configuration, while the periodic arrays are square arrangements with lattice periods of 400 nm, 500 nm, and 600 nm.

As expected, a clear difference in the spectral response between the aperiodic and periodic arrays was observed. The aperiodic array (black curve) displays a broad dip centered at 865 nm, which corresponds to the localized surface plasmon resonance (LSPR). Although the curve is not completely flat outside the resonance band, no distinct secondary dips are visible, indicating the absence of diffractive effects typically associated with periodic lattice structures. This suggests that the resonance profile closely resembles that of an isolated nanoparticle. In contrast, the transmittance spectra of the periodic arrays (colored curves) exhibit a hybrid spectral response that clearly reflects the influence of the lattice on the plasmonic behavior of the nanodisks. This coupling between the LSPR and diffraction effects gives rise to surface lattice resonances (SLRs), which modify the resonance shape and position compared to the aperiodic case.

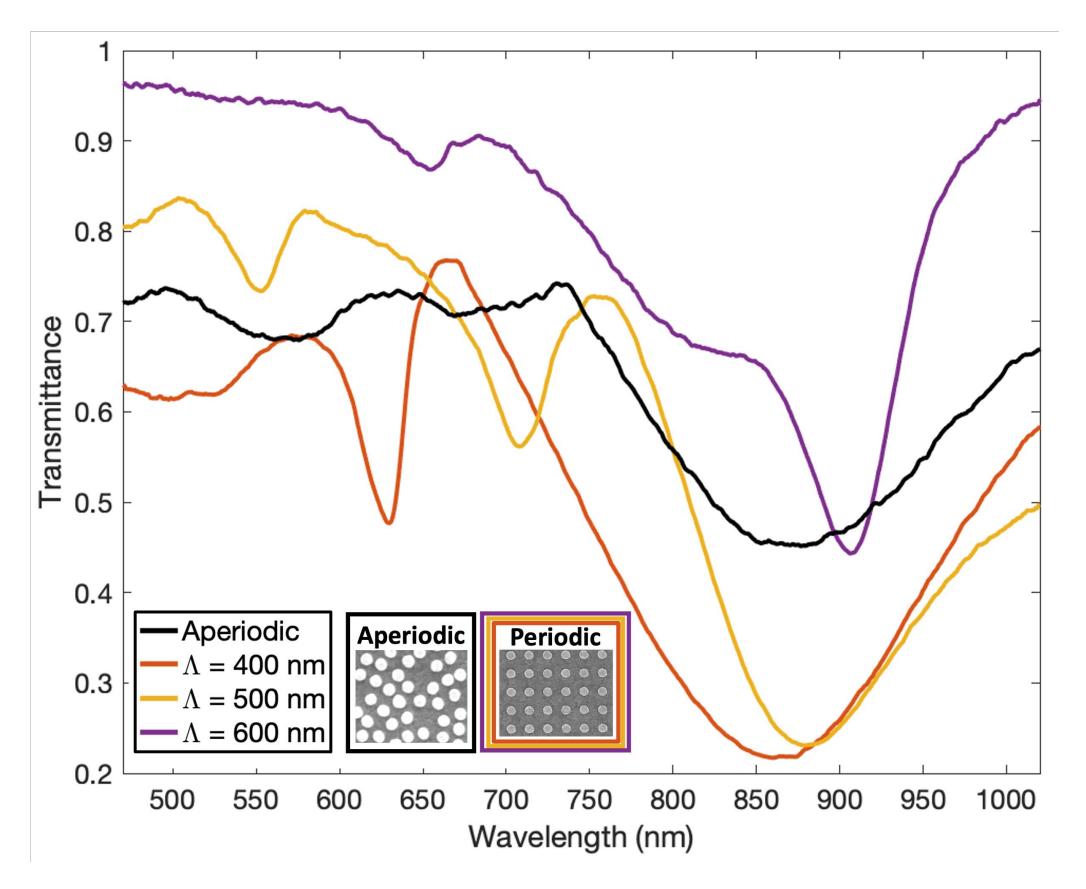


Figure 3.15: Measured transmittance spectra of fabricated nanoantenna arrays.

For the 400-nm period array (orange curve), a non-plasmonic dip is observed around 630 nm. This feature arises from the diffraction of incident light as it interacts with the array of nanodisks, which behaves like a grating at that wavelength. Since this dip is sufficiently distant from the broad plasmonic resonance centered at 860 nm, it does not significantly affect the resonance. The 500-nm period array (yellow curve) shows two distinct dips, around 550 nm and 705 nm, respectively. As in the previous case, these dips are caused by diffraction, with their spectral positions shifting due to the increased lattice period. While the first dip remains non-interacting with the plasmonic mode, the second lies closer and interacts slightly with the broad resonance, now red-shift to 880 nm. This interaction results in a typical Fano-like spectral profile, characterized by the asymmetric splitting of the broad plasmonic resonance due to interference with the narrow diffraction-induced dip. This effect becomes more pronounced in the 600-nm period array (purple curve), which exhibits a small dip at 654 nm due to the diffraction, along with a narrow hybrid resonance dip red-shifted to 906 nm. This latter feature results from the coupling between the localized surface plasmon resonance (LSPR) and the diffracted modes. This interaction gives rise to a surface lattice resonance (SLR), which is particularly desirable for sensing applications, as narrower resonances lead to higher figures of merit.

Compared with the previous simulations, the experimental results did not display the exact resonance wavelength but showed a strong qualitative agreement. For larger lattice periods, the resonance undergoes a red-shift and becomes narrower as a result of coherent coupling between the nanoantennas. The discrepancies between modeling and measurements can be attributed to imperfections in the ITO substrates, differences between the material parameters used in the simulations and those employed in the fabrication process, variations between the designed and fabricated shapes of the nanodisks, and slight deviations from normal incidence during characterization. Despite these differences, the results are relevant as they experimentally demonstrate the impact of the nanoantenna distribution within the array. Additionally, the aperiodic array provides insights into the spectral response of single nanoparticles, which is challenging to obtain through experiments.

Based on the experimental findings, the device selected for biosensing and electrophysiological monitoring experiments was the periodic array with a 600-nm lattice period. Among the different tested arrays, this particular geometry exhibited a well-defined transmittance spectrum characterized by a strong amplitude and the narrowest dip within the NIR-I band, which is our region of interest.

3.5 Conclusions

This chapter described the working principle of the proposed plasmonic device as a biomolecular sensor and an electrophysiological probe. Furthermore, it detailed the modeling, fabrication and optical characterization of the nanoantenna array to identify the optimal configuration for the intended applications.

Using electromagnetic simulations, the geometry and dimensions of the gold nanoantennas were designed to operate within the NIR-I band, while also considering fabrication constraints. The distribution of nanoantennas in the array was evaluated to analyze the lattice effect on resonance and the electric field enhancement factor. The scattering cross-section of a single nanoantenna was found to be significantly large approximately four times greater than that reported in a recent similar work [20] and several million times larger than those of genetically encoded voltage indicators (GEVIs) [79]. The transmittance spectrum of the nanoantenna array confirmed operation within the desired band, and near-field simulations verified substantial local field enhancement, concluding that the designed device has strong potential as a sensor and probe.

The fabrication process utilized e-beam lithography, enabling precise spatially controlled arrangements. Large nanoantenna arrays, with a 2×2 mm² footprint containing more than 11 million gold nanodisks, were produced to facilitate optical characterization and biological experiments. Both periodic square arrays and an aperiodic array were fabricated to comparatively analyze the lattice effect.

Optical characterization of the nanoantenna arrays was conducted using a custom-built spectroscopic setup. The measured transmittance spectra demonstrated both Localized Surface Plasmon Resonance (LSPR) and Surface Lattice Resonance (SLR), confirming the successful excitation of these plasmonic phenomena in the fabricated structures. The aperiodic array exhibited an LSPR response, providing insights into the spectral behavior of a single nanodisk. In contrast, the periodic arrays displayed a hybrid response due to the interplay between LSPR and Rayleigh anomalies, leading to the formation of SLRs. The resonance features varied according to the different lattice periods. While some discrepancies were observed between simulated and experimental resonance wavelengths, the overall trends of the lattice effect on the resonance dip showed strong agreement. Based on the experimental results, the periodic nanoantenna array with a 600 nm lattice period was selected for biosensing and cell monitoring applications, as this configuration exhibited the narrowest resonance within the desired spectral range, thereby ensuring a more precise detection process.

Finally, it is important to emphasize that this study focuses on a case analysis of a nanodisk array to evaluate the impact of periodicity and the formation of SLR, rather than providing an exhaustive optimization across various nanoparticle geometries. Although further refinement involving different shapes could enhance performance, this

work clearly demonstrates that substantial improvements can be achieved through lattice effects alone, without intricate nanostructuring [80–84]. This highlights the powerful role of diffractive coupling in enhancing optical performance. In addition, the structural simplicity and fabrication feasibility of the proposed design offer practical advantages for scalable and cost-effective implementations, particularly in applications where ease of manufacture and reproducibility are critical.

Chapter 4

Biosensing

As explained in the previous section, the developed device has dual functionality. The first function is the detection of specific molecules in biological samples, which is highly valuable for diagnostics and comprehensive study of living systems. In this chapter, this application was tested and evaluated using the fabricated nanoantenna array. Initially, a proof of concept was conducted using sucrose solutions at different concentrations. Subsequently, the biological experiment was performed with the device specialized for detecting the cortisol hormone.

4.1 Proof of concept

The proof of concept demonstrates the device operation as a refractive index sensor. The test involves varying the refractive index of the surrounding medium and detecting changes in the optical response of the device. A microspectroscopic setup based on an upright microscope (Axio Examiner, Carl Zeiss) was employed for this procedure. While this setup included components similar to those used in the optical characterization of the nanoantenna arrays, equipment from different vendors was utilized because this test was carried out in collaboration with the NanoGUNE research center in Basque Country. Specifically, we used a halogen lamp (HL-2000, Ocean Optics) with a wavelength range from 360 nm to 2,400 nm and a fiber-coupled CCD spectrometer (Maya2000Pro, Ocean Optics) ranged from 165 nm to 1,100 nm.

The employed configuration offered several advantages compared to the previous one. First, it allowed the sample to be placed in a horizontal position, making it suitable for dropping solutions onto the device. Second, a portion of the transmitted light was directed to the microscope eyepiece, enabling sample visualization. Fig. 4.1a and 4.1b show the schematic and the implemented setup for this proof of concept, respectively.

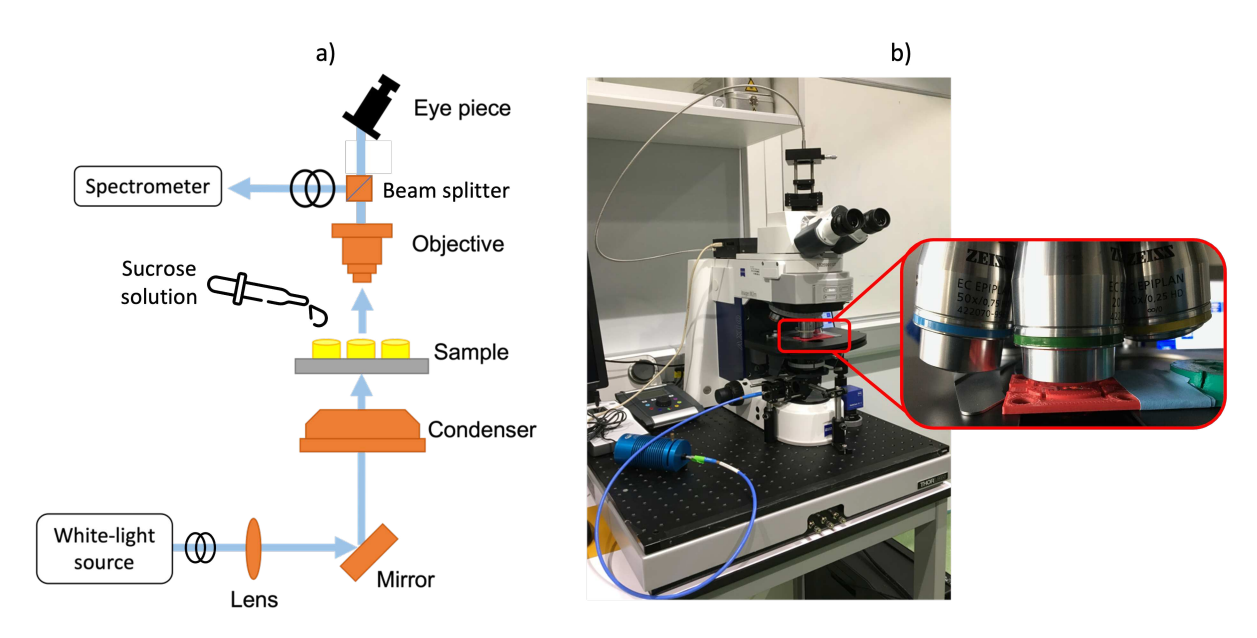


Figure 4.1: a) Schematic and b) implemented setup for the proof of concept of the device as a index refractive sensor.

To apply a surrounding medium with varying refractive indices, solutions of sucrose (S0389, Sigma-Aldrich) in deionized (DI) water were prepared at concentrations of 2%, 5%, 8%, and 10%. The refractive index of each sucrose solution was measured using a refractometer (PCE-DRH 1, PCE Instruments), with a resolution of ± 0.0001 RIU, resulting in the calibration curve shown in Fig. 4.2. Additionally, since measurements in sensing applications are relative, the value obtained at 0% concentration (pure DI water) was assumed as the reference. Table 4.1 shows the refractive index values of the sucrose solutions and their variations relative to that reference.

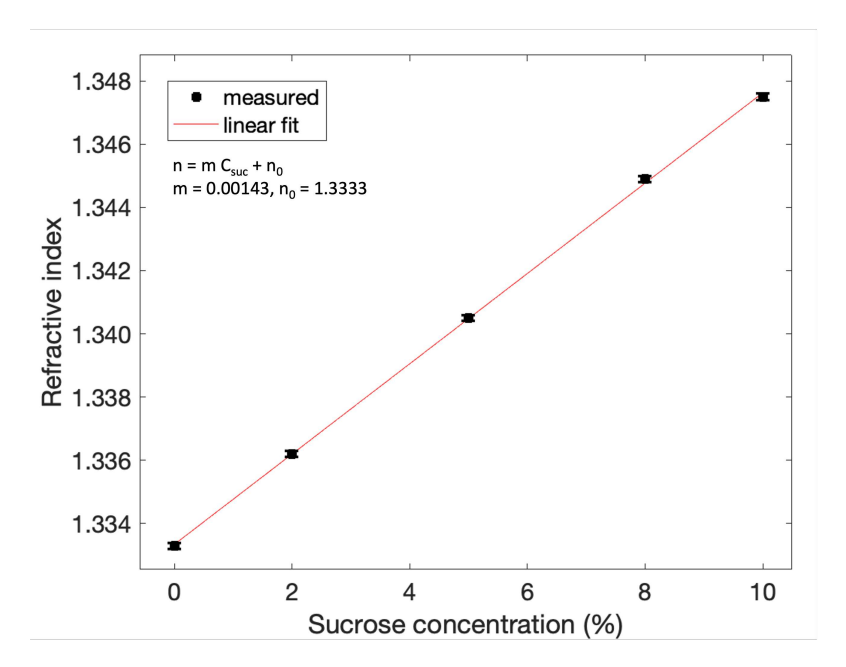


Figure 4.2: Calibration curve of the refractive index as a function of sucrose concentration in DI water. Single measurements; error bars reflect ± 0.0001 RIU resolution.

Solution	$\mathbf{n}_{sucrose}$	$\Delta \mathbf{n}_{sucrose} = \mathbf{n}_{sucrose} - \mathbf{n}_{water}$
2% Sucrose	1.3362	2.90×10^{-3}
5% Sucrose	1.3405	7.20×10^{-3}
8% Sucrose	1.3449	1.16×10^{-2}
10% Sucrose	1.3475	1.42×10^{-2}

Table 4.1: Refractive indices of aqueous sucrose solutions

As previously shown in equation 2.1, the sensitivity of the device is defined as the ratio between the variation of an optical parameter and the change in the refractive index of the medium. In this proof of concept, the optical parameter was obtained from the transmittance of the nanoantenna arrays. The transmitted light through the sample was collected by the spectrometer and normalized to transmitted light through the unpatterned area of the substrate. Fig. 4.3 shows the transmittance spectra obtained for the reference and all the aqueous sucrose solutions. These spectral curves were rescaled from 0 to 1 for better visualization of the wavelength shift.

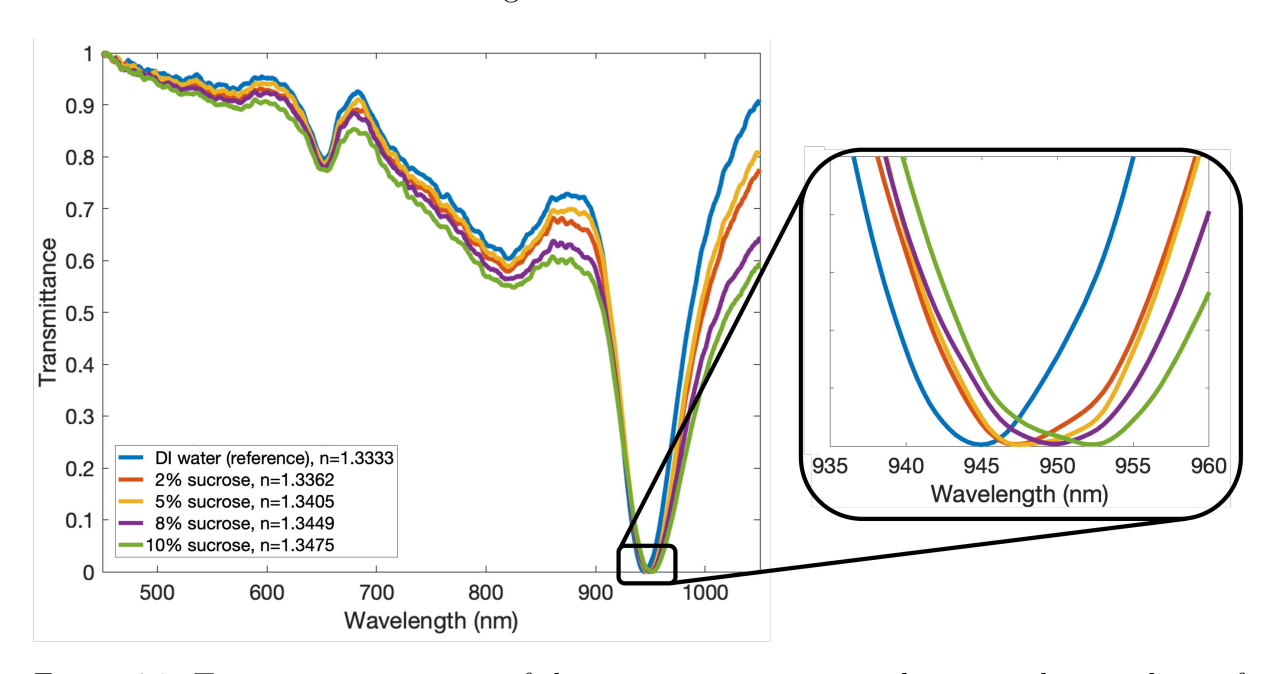


Figure 4.3: Transmittance spectra of the nanoantenna array with surrounding medium of sucrose solutions at different concentrations.

As illustrated in the inset of Fig. 4.3, increasing the concentration of sucrose solutions caused a red-shift in the resonance dip due to the higher refractive indices of the medium. From these measurements, the calibration curve of the device was generated, as shown in Fig. 4.4. This curve shows the resonant wavelength shift as a function of the refractive index change. After a suitable linear fitting was done, the experimental sensitivity was given by the slope of the curve, resulting in a value of 471 nm/RIU.

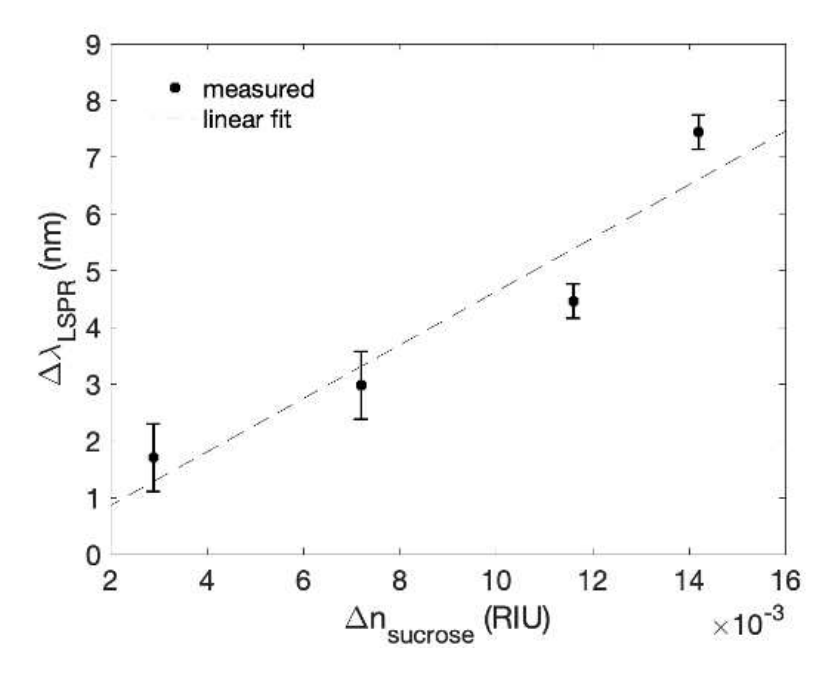


Figure 4.4: Sensitivity curve of the device for refractive index sensing.

To determine the figure of merit (FOM) of the device as a refractive index sensor, equation 2.3 was applied. The full width half maximum (FWHM) was obtained using the reference curve of DI water. Fig. 4.5 illustrates how this parameter was determined [82]. The transmittance value at the dip is denoted as T_2 , and the local maximum transmittance value at the left shoulder is denoted as T_1 . The FWHM was taken at the transmittance value of $(T_1+T_2)/2$, as indicated by the red arrowed line, resulting in 57 nm. From the experimental sensitivity and FWHM, the calculated FOM was 8.3 RIU⁻¹.

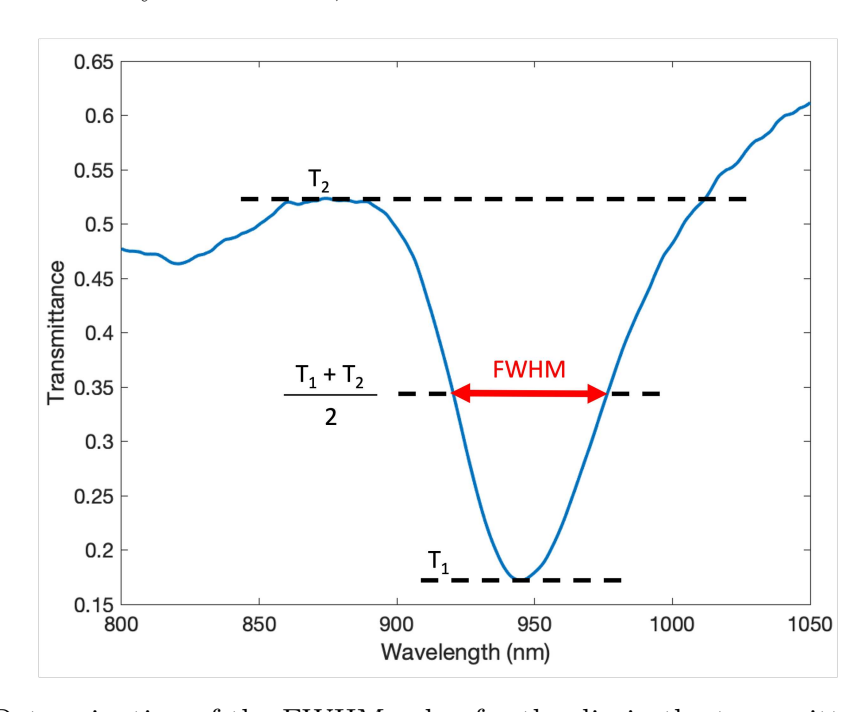


Figure 4.5: Determination of the FWHM value for the dip in the transmittance spectrum.

Table 4.2 presents a comparison of the sensing performance of this work against previously reported plasmonic sensors. Our results surpass those reported by [80, 85, 86], which utilized silver nanotriangle arrays, gold elliptic nanodisk-ring structures, and silicon nanodisk oligomers, respectively. Although the gold nanoring design proposed by [84] demonstrate superior performance, it remains at the simulation stage with many parameters strictly controlled. Meanwhile, the experimental results from [81] exhibited higher sensitivity, but our device significantly outperforms it in terms of FOM. Other notable studies include [83] and [82], which achieved excellent results by optimizing the shape and configuration of the nanostructures. The former combined nanorings with a flat gold film to simultaneously excite gap and lattice plasmons, while the latter utilized mushroom-shaped nanoparticles to approach the theoretical limit of FOM.

Overall, the sensing performance demonstrated here is competitive with devices reported in the literature, validating the suitability of the proposed structure for refractive index sensing. While there remains room for further optimization, particularly in terms of nanoparticle shape and array configuration, this work deliberately focused on a simple and reproducible nanodisk array. This choice emphasizes the significant benefits that can be achieved through periodic nanoparticle arrangements and the exploitation of SLR.

Material and geometry	Sensitivity (nm/RIU)	${ m FOM} \ ({ m RIU}^{-1})$	Type of study	Reference
Au nanodisk array	471	8.3	Experimental	This work
Ag nanotriangle array	210	Not reported	Experimental	[85]
Au elliptic nanodisk-ring	440	7.95	Simulated	[80]
Si nanodisk oligomers	150	3.8	Experimental	[86]
Ag nanorings	524.3	10.024	Simulated	[84]
Au nanoring array	577	6.1	Experimental	[81]
Au nanoring-on-film	386 - 615	5 - 44	Experimental	[83]
Au mushroom array	1015	80 - 108	Experimental	[82]

Table 4.2: Performance metrics of plasmonic refractive index sensors.

4.2 Cortisol detection

After successfully completing the proof of concept, the next stage involved conducting a biosensing experiment focused on detecting a specific molecule: the cortisol hormone. This stage required specialization of the nanoantenna array, adapting it for the precise detection of cortisol. Cortisol is widely recognized as a critical biomarker of stress, which is triggered by feelings of anxiety or threats arising from psychologically or physically challenging situation [87]. The body's production of cortisol is a natural response to these stressors, but when levels remain elevated for long periods, it can lead to

significant implications. Therefore, the development of reliable tools for monitoring cortisol levels in real-time is crucial for diagnosing and preventing stressed-induced mood disorders that can lead to mental illnesses, including depression, mania and bipolar disorder [88].

To specialize the device for detecting the target molecule, a biofunctionalization procedure was required. In this work, cortisol aptamers were used to capture the cortisol molecules, as illustrated in Fig. 4.6. While several previous studies have utilized antibodies for cortisol capture, these have some disadvantages. Antibodies may denature during long-term storage, exhibit high variability, and show cross-reactivity. Moreover, detecting low concentrations of cortisol in the nanomolar range typically requires additional materials, such as secondary antibodies and fluorescent indicators [89]. Aptamers, on the other hand, are short, single-stranded DNA or RNA molecules that exhibit high affinity and specificity toward a unique target analyte. Upon interaction with the analyte, aptamers undergo a conformational change, which can be detected by monitoring the optical response of the sensor [90]. Unlike antibodies, aptamers are chemically synthesized, making them more stable across a wider range of temperatures and pH levels.

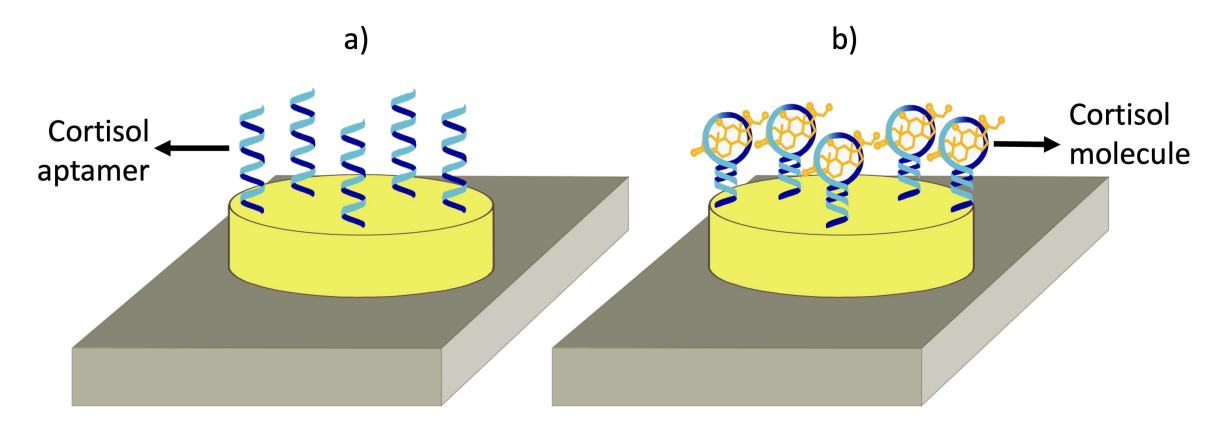


Figure 4.6: Schematic of aptamer-based biofunctionalization of a gold nanodisk. a) Cortisol aptamer application. b) Capturing of cortisol molecules.

The biofunctionalization of the gold nanodisks was conducted in collaboration with the Laboratory of Electrochemistry, Electroanalytics and Sensor Development (LEEDS), led by Prof. Dr. L. Kubota (*in memoriam*) at UNICAMP. The procedure followed the protocol outlined below:

- 1. Cleaning: The sample was soaked for 5 minutes in 5% Extran detergent (107553, Merck) in Milli-Q water, rinsed with IPA, and dried with a nitrogen jet.
- 2. Aptamer pretreatment: Cortisol aptamer (U541KFL040-1, GenScript) with the sequence 5'-ATGGGCAATGCGGGGTGGAGAATGGTTGCCGCACTTCGGC-3 and 5' Thiol Modifier C6 S-S was diluted to 5 μM in 10 mM Tris buffer (327360050, Acros Organics) pH 7.4 containing 100 mM NaCl (31434, Sigma-Aldrich) and pretreated with 3 mM TCEP (580560, Merck) in a thermal cycler (T100, BioRad) at 37°C for 30 minutes to reduce the S-S bonds.

3. **Aptamer immobilization**: 10 μ L of pretreated aptamer solution was applied to the sample and left in a cleanroom for 18 hours (overnight) under suitable humidity conditions to prevent the solution from drying out. The sample was rinsed with the buffer solution, and dried with a nitrogen jet.

In addition, cortisol solution was prepared from hydrocortisone (H4001, Sigma-Aldrich) at 10 mg/mL (27.6 mM) in ethanol (1.11727, Merck) and diluted at concentrations of 500 nM, 1 μ M, 5 μ M, 100 μ M and 3 mM in the buffer solution.

The biosensing experiments were carried out using a vertical microspectroscopic setup at the Photonicamp research center at UNICAMP. The schematic is illustrated in Fig. 4.7, and the implemented setup is shown in Fig. 4.8. The illumination source consisted of a tungsten-halogen lamp (SLS201L, Thorlabs) with a spectral range from 360 nm to 2,600 nm, and a bright field condenser (Abbe, Nikon Instruments) used to shape the emitted light into a cone that uniformly illuminated the sample. The transmitted light was collected by an objective lens (RMS20X, Olympus) and split by a 45° tilted cover slip, which directed around 4% of light to a CCD camera (DMK 23U445, Imaging Source). The remaining transmitted light was guided by optical components (a 45° tilted mirror, an aspheric lens, and a 400- μ m multimode optical fiber patch cable) to a spectrometer (CCS175, Thorlabs) ranged from 500 nm to 1,000 nm. The transmittance was obtained by normalizing this measurement against those from the unpatterned area of the substrate.

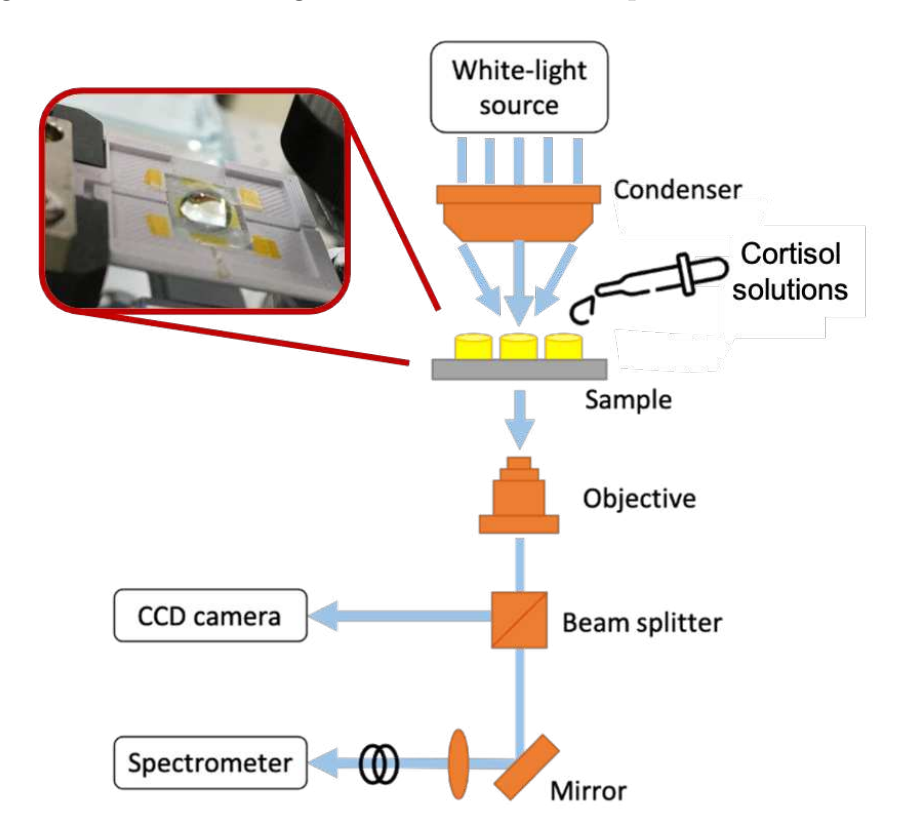


Figure 4.7: Schematic of the microspectroscopic setup used in the biosensing experiment for cortisol detection.

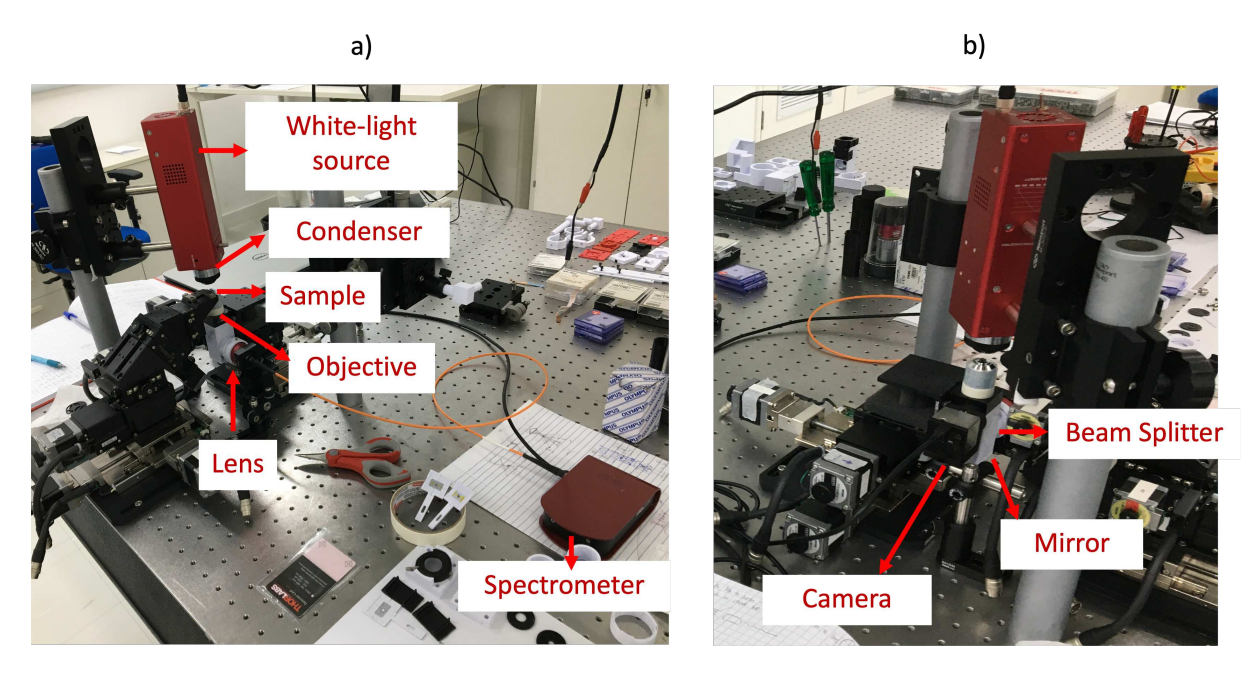


Figure 4.8: Setup used for the biosensing experiment to detect cortisol. a) Front view. b) Rear view.

The following protocol was employed for the biosensing experiment designed to detect cortisol using the nanoantenna array:

- 1. **Initial measurement:** After completing the biofunctionalization procedure, the transmittance of the sample was measured. This initial measurement served as the control of the experiment, providing a reference point against which any subsequent shifts in the resonance wavelength were calculated.
- 2. Application of cortisol solution: A 500 nM cortisol solution was applied to the sample and left for 25 minutes, allowing the aptamers immobilized on the surface of the gold nanodisks to capture cortisol molecules from the solution. Following this incubation period, the sample was rinsed with the buffer solution to remove unbound molecules and subsequently dried with a nitrogen jet to ensure the surface was free of excess liquid.
- 3. **Transmittance measurement:** The transmittance of the sample was measured again and recorded as the response curve corresponding to the 500 nM cortisol concentration. This measurement was critical for understanding how the biosensor responded to this specific concentration of cortisol.
- 4. Incremental cortisol concentration testing: Steps 2 and 3 were systematically repeated for cortisol solutions of progressively higher concentrations: 1 μ M, 5 μ M, 100 μ M and 3 mM. These steps were conducted in order from the lowest to the highest concentration to prevent premature saturation of the device, which could compromise the accuracy and sensitivity of the measurements.

Fig. 4.9 shows the transmittance spectra obtained from the biosensor, initially with only the aptamer layer (black curve) and subsequently after applying cortisol solutions at various concentrations (colored curves). As seen, increasing the cortisol concentration results in a red-shift in transmittance. This red-shift is attributed to the increasing number of cortisol molecules captured by the aptamer layer on the surface of the gold nanodisks, which results in a higher refractive index of the surrounding medium. As demonstrated during the proof of concept, such an increase in the refractive index causes the plasmonic resonance to shift to longer wavelengths. However, beyond a cortisol concentration of 5 μ M, no further wavelength shifts were observed, indicating that the biosensor had reached its saturation point. At this stage, the aptamer layer was fully occupied by cortisol molecules, leaving no available bioreceptors to bind additional molecules from higher concentration solutions.

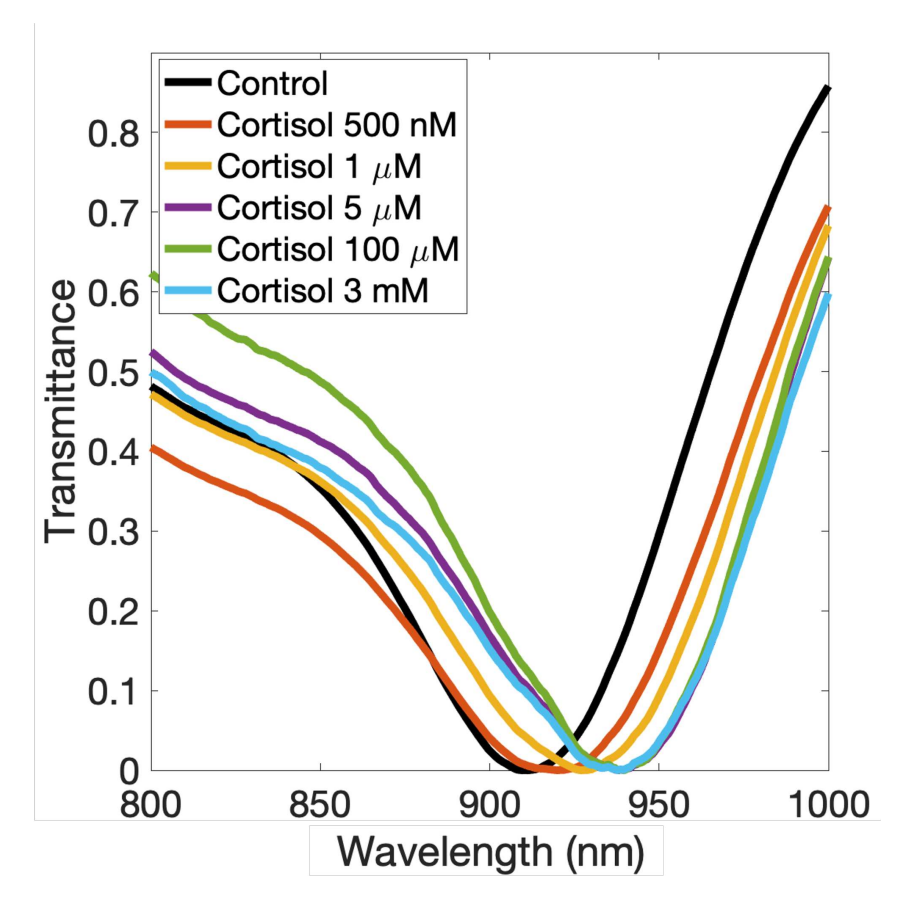


Figure 4.9: Transmittance spectra of the biofunctionalized nanoantenna array for cortisol solutions at different concentrations.

From the transmittance spectra results, the dose-response curve shown in Fig. 4.10 was generated, displaying the resonance wavelength shift as a function of cortisol concentration in logarithmic format. In the linear region, before saturation range, a linear fit was performed using the results for the concentrations of 500 nM, 1 μ M and 5 μ M, yielding the dose-response equation shown in the inset. As observed, $\Delta \lambda_{LSPR}$ increased in correlation with higher cortisol levels, exhibiting a strong linear relationship, with a

coefficient of determination r²=0.989. In addition, the limit of detection (LoD) of the biosensor was estimated by assuming that the smallest detectable signal corresponds to three times the standard deviation of the noise level of the system, as detailed in chapter 2. The standard deviation, calculated from 15 measurements of the sample without containing the analyte, was found to be 0.299 nm. Using the dose-response equation, the cortisol concentration that would produce a wavelength shift equal to three times this standard deviation was determined to be 166.6 nM. This value represents the lowest cortisol concentration that the biosensor can reliably detect, highlighting the potential of the nanoantenna array as an effective tool for measuring cortisol at low concentrations. Such responsiveness is crucial for monitoring stress levels in biological samples where cortisol may be present in minimal amounts.

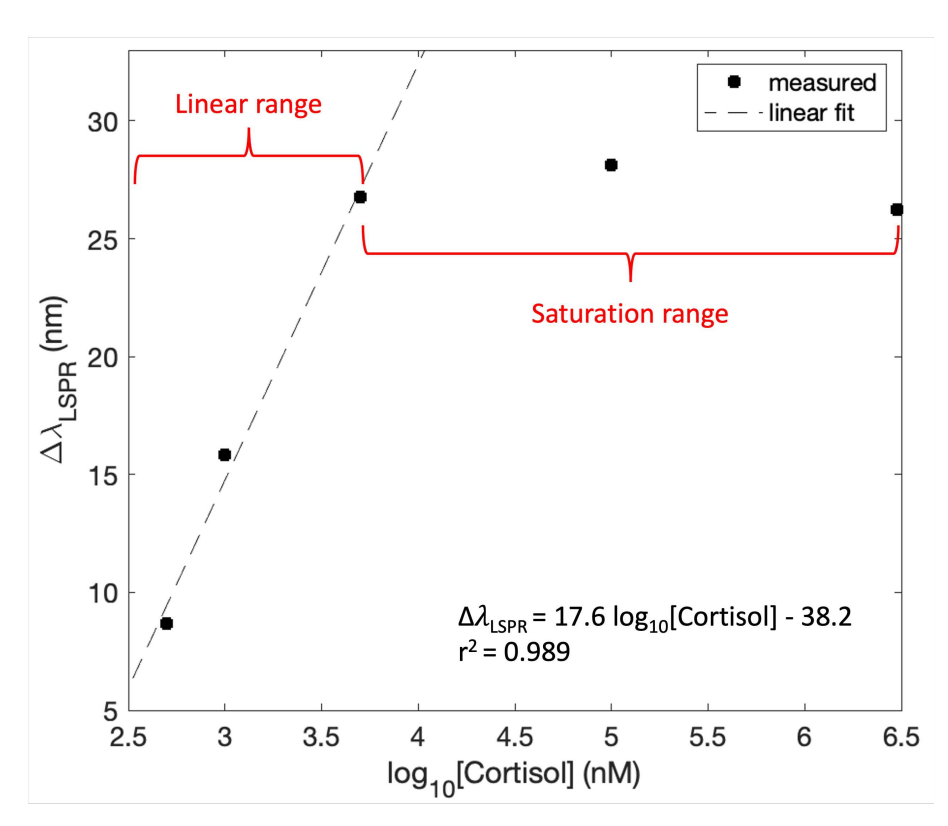


Figure 4.10: Dose-response curve for cortisol detection in the biosensing experiment.

4.3 Conclusions

This chapter detailed the application of the developed plasmonic nanoantenna array as both a refractive index sensor and a biosensor for cortisol detection. The successful proof of concept demonstrated the capability of the device to detect changes in the refractive index of the surrounding medium using sucrose solutions at varying concentrations. The transmittance spectra exhibited a clear red-shift in resonance wavelength with increasing sucrose concentration, confirming the high sensitivity of the nanoantenna array to refractive

index variations. The device achieved a sensitivity of 471 nm/RIU and a figure of merit (FOM) of 8.3 RIU⁻¹, demonstrating a competitive performance compared to previously reported experimental and simulated studies. These results highlight the potential of the developed nanoantenna array for precise and reliable sensing applications.

The biosensing experiment was conducted by biofunctionalizing the nanoantenna array with cortisol-specific aptamers to detect cortisol, a key biomarker for stress. The transmittance spectra obtained during the experiment exhibited a red-shift in resonance wavelength with increasing cortisol concentrations, up to a point of saturation. The dose-response curve showed a good linear relationship between the resonance shift and cortisol concentration. In addition, the limit of detection (LoD) was calculated to be 166.6 nM, indicating the capability of the biosensor to detect small amounts of cortisol, which is crucial for monitoring stress levels in biological samples.

While the LoD obtained in this study is within the nanomolar range, it remains higher than the typical values achieved by the gold-standard Enzyme-Linked Immunosorbent Assay (ELISA) used in clinical settings, which ranges from 0.09 ng/mL to 30 ng/mL, equivalent to 0.25 nM to 82.8 nM [91]. However, it is important to note that aptamer-functionalized LSPR-based biosensors offer several advantages over traditional ELISA methods, such as label-free detection, which reduces complexity and reagent costs, and potential for miniaturization and portability [92]. Compared to other LSPR-based biosensors [89,93], our LoD is higher, but there are techniques that can be easily implemented to optimize it. For instance, reducing the pH of the buffer solution to concentrate the aptamers on the gold nanodisks rather than the substrate, or applying a positive voltage to the conductive substrate to strengthen the thiol linkage with the gold nanodisk.

In conclusion, these findings underscore the effectiveness of the plasmonic nanoantenna array as a biosensing platform. The device's good sensitivity, low LoD, and strong linear response make it a promising tool for various biomedical applications, including the detection of other biomarkers of living systems. Moreover, it is worth noting that the proposed nanoantenna array is a dual-purpose device, with its biosensing functionality complemented by electrophysiological monitoring, which will be detailed in the next chapter.

Chapter 5

Electrophysiological monitoring

In the previous chapter, one of the dual functionalities of the developed nanoantenna array consisting of biomolecular sensing was thoroughly demonstrated. This chapter focuses on the other functionality of the device, which involves monitoring the electrophysiological activity of living cells. The same nanoantenna array that was used for detecting biomolecules is now repurposed to sense electric fields generated by excitable cells. Similar to the approach taken in the biosensing application, the process began with the proof of concept, where a function generator applied an external electric field across the nanoantennas. After successfully monitoring this controlled electric field, the biological experiment was conducted using cardiomyocyte cells isolated from rats.

5.1 Proof of concept

The proof of concept aimed to demonstrate the ability of the nanoantenna array to function as an electro-optical probe, capable of monitoring external electric fields through the optical response of the nanoantennas. This was achieved using optoelectrochemical, also known as spectroelectrochemical, recordings. This technique allows for real-time monitoring of optical signals during electrochemical reactions, facilitating the observation of light-sample interactions under the influence of an electric field [94]. In this case, the scattering signal from the nanoantennas was recorded while an external electric field was applied.

A dark-field transmission setup was implemented to monitor the temporal scattering signal from the nanoantenna array. This setup uses oblique illumination to collect only the light scattered by the nanoparticles, while blocking the transmitted light traveling along the direct optical path. Fig. 5.1a and 5.1b illustrate the differences between traditional bright field and the dark field microscopy in transmission mode, both schematically and through the micrographs obtained by each configuration.

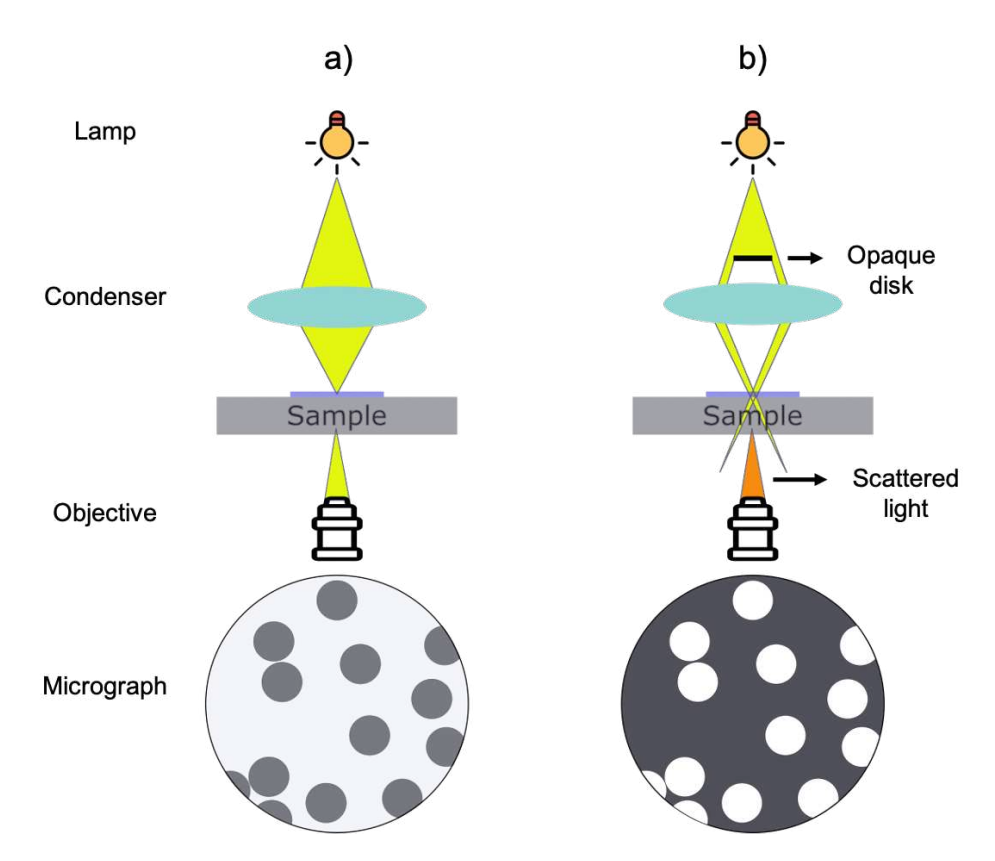


Figure 5.1: Comparison of schematics and micrographs for a) bright field and d) dark field microscopy.

Since a dedicated dark field microscope was unavailable for this work, the vertical microspectroscopic setup previously used for the cortisol detection was adapted to serve this purpose. To achieve dark field illumination, an opaque disk was custom fabricated from polylactic acid (PLA) using a 3D printer (Ender-3, Creality). This disk was carefully positioned in the filter holder of the tungsten-halogen lamp (SLS201L, Thorlabs). By introducing this opaque disk, we were able to block direct light from the source, thereby ensuring that only scattered light from the sample would be collected. This straightforward modification allowed the transition of the standard setup into a functional dark field system.

Moreover, a high numerical aperture (NA) condenser (Abbe, Nikon Instruments) was placed at the output of the light source, creating a hollow cone of light to illuminate the sample obliquely, from the sides rather than along the central optical axis. In dark field setups, the condenser's NA must be higher than that of the objective lens to ensure only the scattered light is collected, while direct transmission of light is prevented from entering the objective. For this setup, a 1.3 NA condenser and a 0.4 NA objective lens (RMS20X, Olympus) were employed to achieve the desired dark field measurements. Fig. 5.2a illustrates the illumination configuration, and 5.2b shows the resulting micrographs, highlighting the scattered light captured against a dark background.

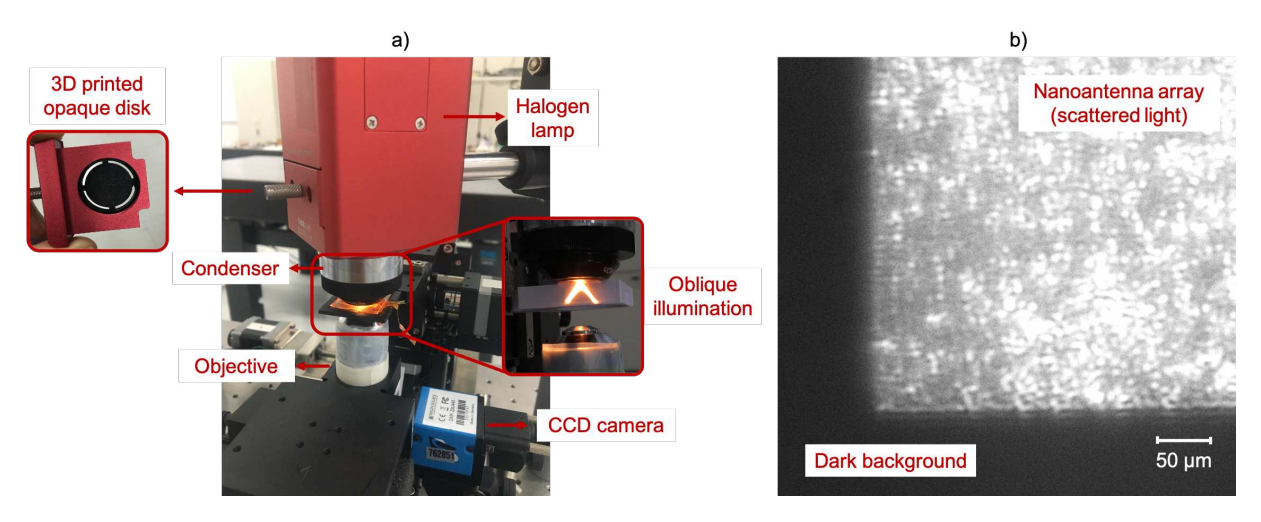


Figure 5.2: Customization of the microspectroscopic setup to dark field transmission setup. a) Illumination configuration. b) Micrograph of the sample.

With the dark field illumination established, the setup was completed to record the time-dependent scattering signal from the nanoantenna array. The same components of the cortisol detection setup were employed, but replacing the spectrometer by a power meter to measure a temporal optical signal instead of a spectrum. The scattered light collected by the objective lens was split by a 45° tilted cover slip (304.107.002, Exacta), directing around 4% of the light to a CCD camera (DMK 23U445, Imaging Source). The remaining scattered light was guided to an optical power meter (PM400, Thorlabs) via a series of optical components, including a 45° tilted mirror, an aspheric lens, and a 400- μ m multimode optical fiber patch cable.

A two-electrode electrochemical cell was built to apply a controlled external electric field across the nanoantenna array. The system consisted of a platinum wire as the counter electrode (CE) and the conductive substrate of nanoantenna array serving as the working electrode (WE), both immersed in an electrolyte solution. To ensure reliable electrical contact with the WE, a copper tape was attached to the substrate. Tyrode solution, commonly employed in physiological experiments due to its ability to mimic the extracellular fluid environment, was selected as the electrolyte. The composition of the solution included 140 mM NaCl, 6 mM KCl, 1.5 mM MgCl₂, 1 mM CaCl₂, 11 mM glucose, 5 mM N-2-hydroxyethylpiperazine-N'-ethane-sulfonic acid (HEPES), with a pH of 7.4 at 23°C. A function generator (CFG280, Tektronix) was used to apply a potential difference between the two electrodes, while an oscilloscope (DSO1002A, Agilent) continuously monitored the voltage. This configuration facilitated the precise control of the applied electric field throughout the experiment. Fig. 5.3 and 5.4 illustrate the schematic and the implemented setup used for the optoelectrochemical recording, showing the arrangement and components of the system.

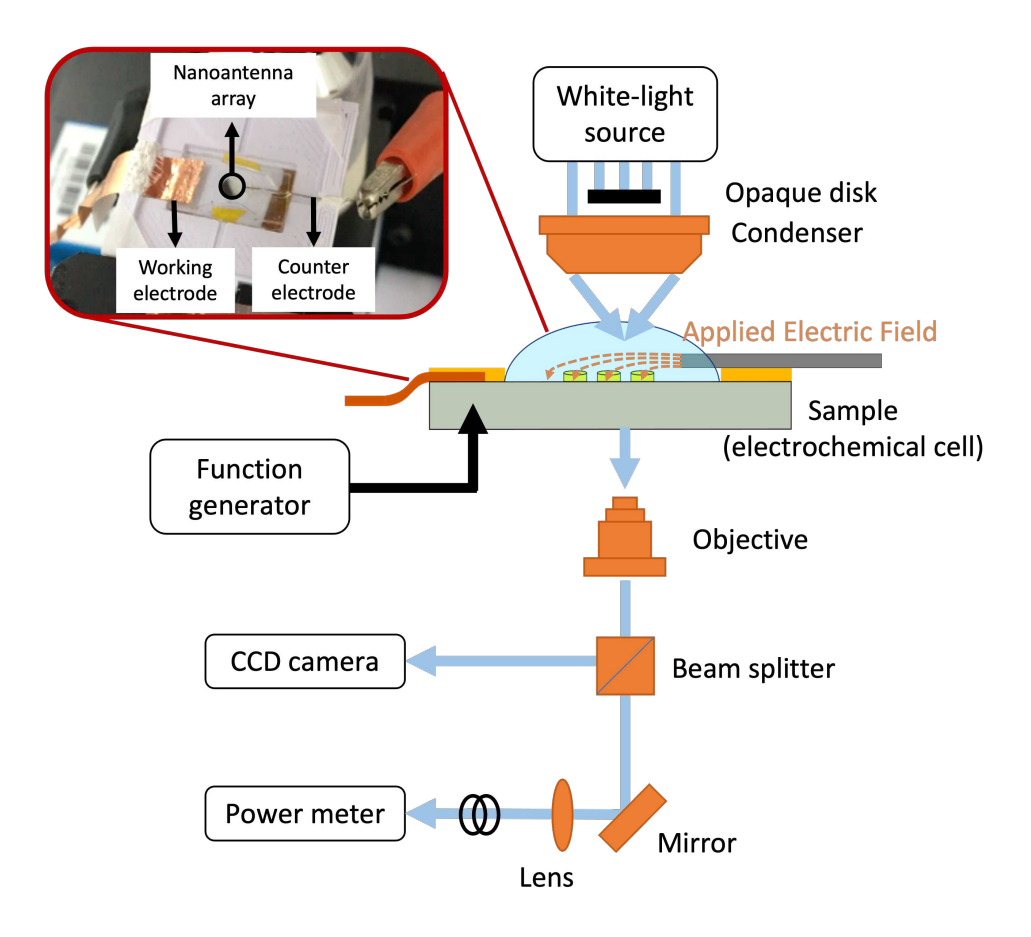


Figure 5.3: Schematics of the dark field setup used for optoelectrochemical recording.

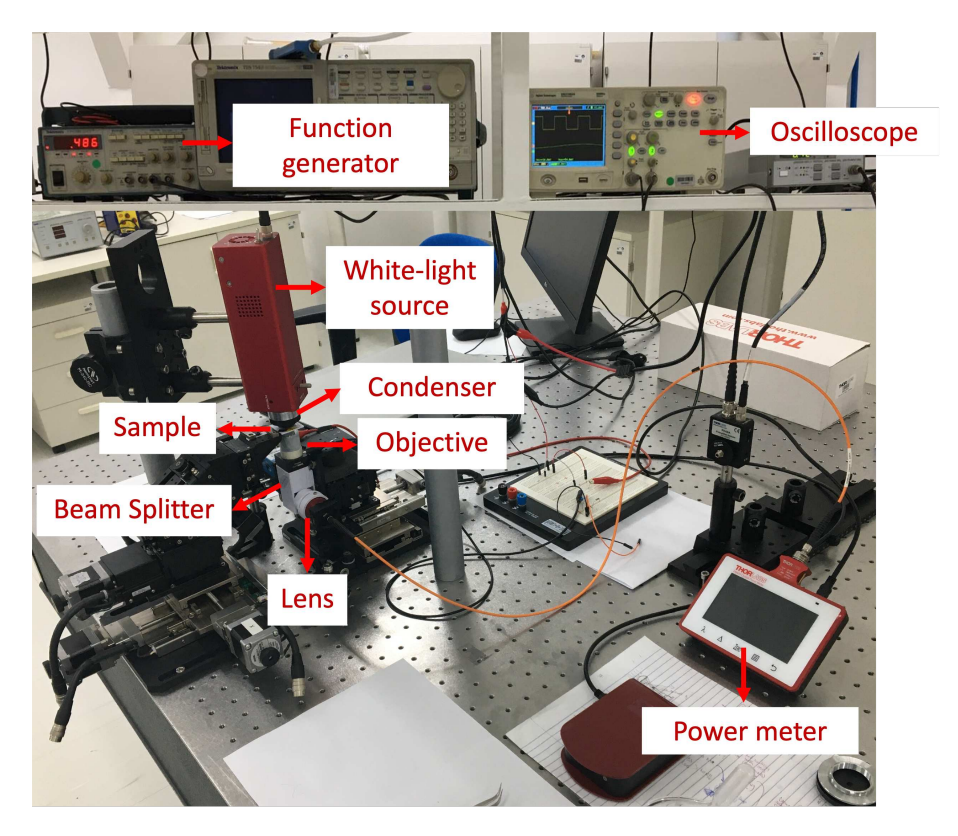


Figure 5.4: Implemented dark field setup for optoelectrochemical recording.

The proof of concept consisted of applying a square voltage of 2 Vpp at a frequency of 2.5 Hz with a 10% duty cycle, resulting in 40 ms square pulses, using the function generator. The potential difference between the electrodes generated an electric field that passed through the nanoantenna array. Simultaneously, the light scattered by the nanoantennas was collected and recorded by the optical power meter set to a wavelength of 850 nm, which was previously identified in the resonance band by the spectrometer. The optical data acquired by the power meter was post-processed with smoothing and baseline correction. In addition, rescaling and normalization to its maximum were applied to avoid negative values resulting from the baseline removal. Fig. 5.5 shows the outcome of the optoelectrochemical recording, illustrating the scattering signal and the applied voltage. These curves demonstrated that the scattering signal of the nanoantennas was modulated in amplitude by the voltage pulses applied to them.

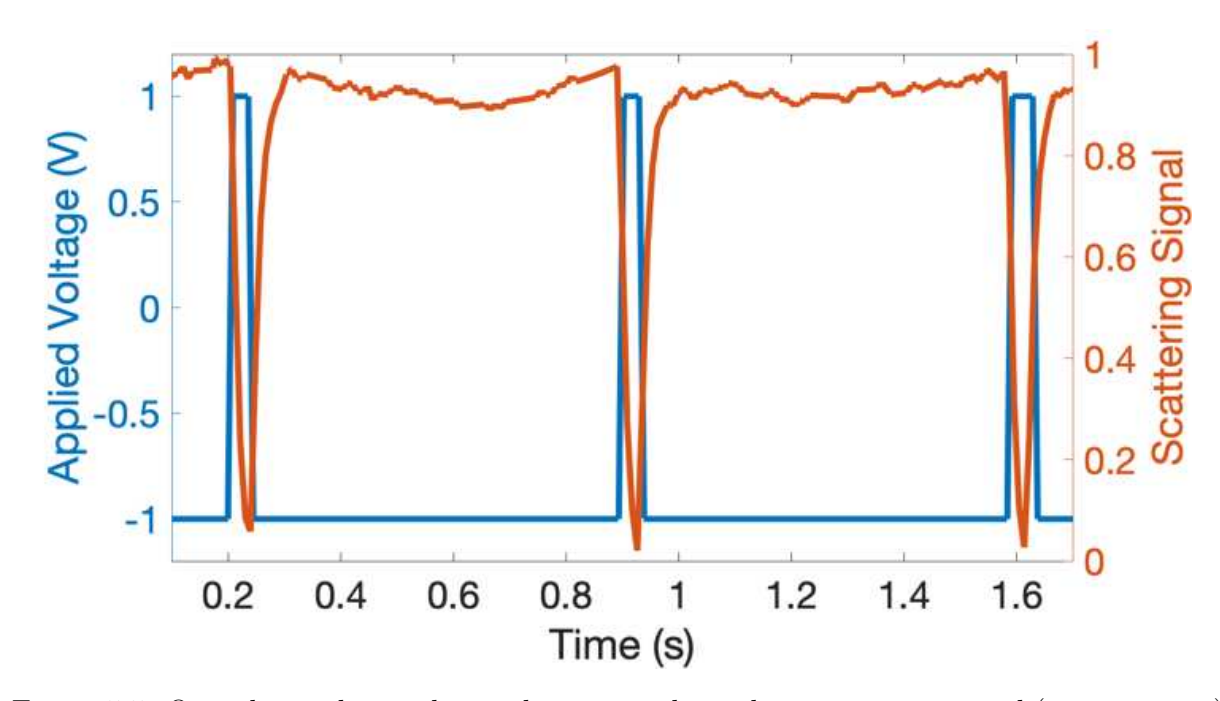


Figure 5.5: Optoelectrochemical recording: time-dependent scattering signal (orange curve) of the nanoantenna array under the application of a square voltage (blue curve).

The obtained results highlight the capability of the plasmonic nanoantenna array to optically monitor electrical activity. With the applied voltage at 2 Vpp and the electrode separation of $\sim 280\,\mu\text{m}$, the applied electric field was approximately 7×10 V/cm. Given that biological extracellular field potentials (EFPs) typically range between 10^2 to 10^3 V/cm, the developed device shows significant potential for detecting such fields, highlighting its promise as a wireless electrophysiological probe.

5.2 Monitoring of cardiomyocyte cells

After successfully completing the proof of concept by monitoring a controlled electric field, the biological experiment was conducted with isolated cardiomyocyte cells from rats. These cells are responsible for generating and transmitting electrical signals that regulate the heartbeat. Since cardiomyocytes are the minimal natural unit of the heart capable of being stimulated, their single-cell monitoring is crucial for demonstrating the high spatial resolution of the proposed plasmonic-based electro-optical technique. The isolation of the cells and the experiments were carried out in collaboration with the Laboratory of Cardiovascular Research at the Center for Biomedical Engineering (LPCV/CEB) under the supervision of Prof. J. W. Bassani at UNICAMP. The experiments were approved by the institutional Committee for Ethics in Animal Use (protocol n° 5470-1/2020).

The isolation of cardiomyocytes from rats was carried out according to the following protocol (see Fig. 5.6) [95]:

- 1. Rats were rendered unconscious by cerebral concussion and euthanized by rapid exsanguination. The heart was then immediately removed.
- 2. Cardiomyocytes were isolated from the left ventricle using coronary perfusion at 37°C with collagenase [96]. In this procedure, the heart was perfused with modified Krebs-Henseleit solution (composed by 115 mM NaCl, 4.6 mM KCl, 1.2 mM KH₂PO₄, 25 mM NaHCO₃, 2.4 mM MgSO₄, 11 mM glucose, pH 7.4, and gassed with 95%O₂/5%CO₂) for 5 minutes, followed by perfusion with the same solution containing 0.8 1 mg/mL collagenase (Type 1, Worthington Biochemical) for approximately 15 minutes, and a final perfusion with the enzyme-free solution for 5 minutes.
- 3. The left ventricle was excised, and the cells were dissociated and kept at 4°C in a storage solution, composed by 30 mM KCl, 70 mM glutamic acid, 10 mM KH₂PO₄, 5 mM 4-(2-hydroxyethyl)-l-piperazine-ethanesulfonic acid (HEPES), 1 mM MgCl₂, 11 mM glucose, and 20 mM taurine, with a pH of 7.4.

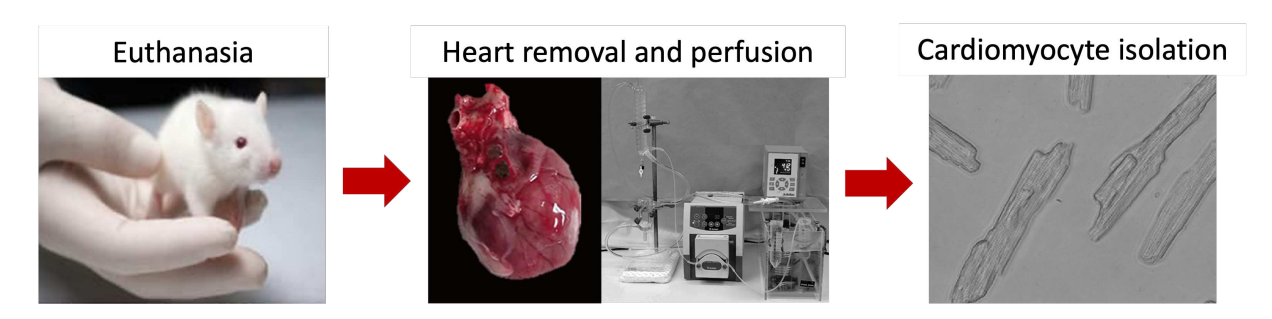


Figure 5.6: Schematic of the protocol for the isolation of cardiomyocytes from rats (adapted from [97,98]).

The setup employed for the biological experiment was similar to that used for the proof of concept, but with modifications to adapt the custom-built electrochemical cell into a suitable platform for exciting cells via an electrical stimulator. Fig. 5.7a and 5.7b illustrate the schematic and the implemented platform used in the experiments, respectively.

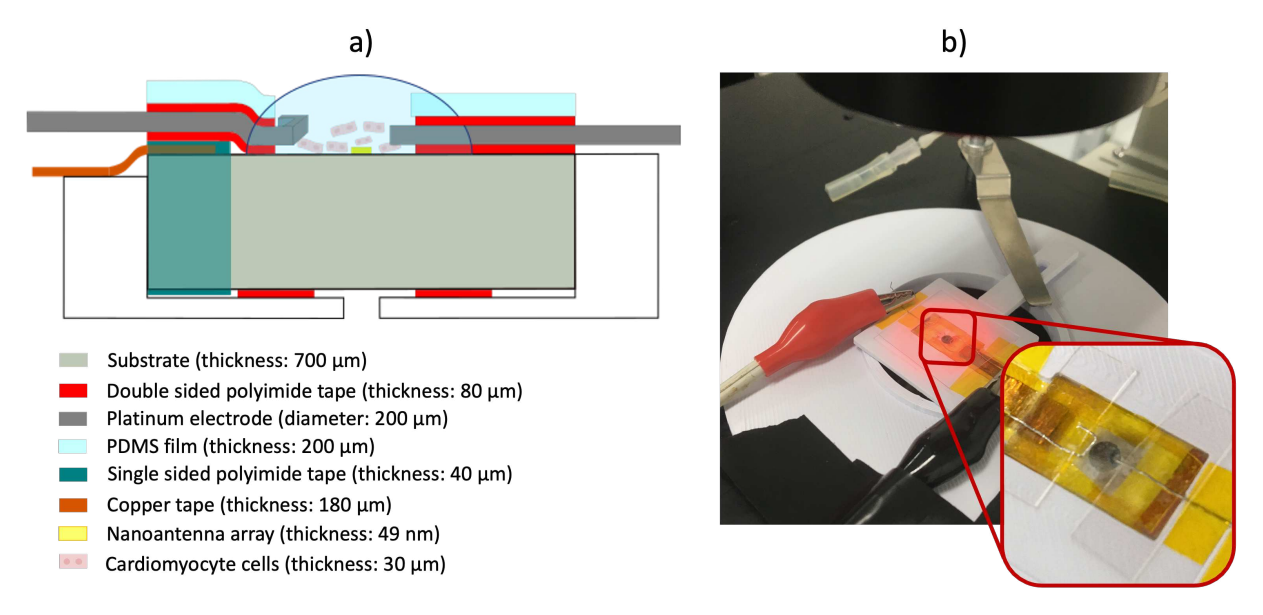


Figure 5.7: a) Schematic and b) implemented custom-built platform for experiments with cardiomyocyte cells.

A 3D-printed sample holder was designed to support the substrate containing the nanoantenna array, featuring a central hole to allow illumination and light collection. To secure the substrate to the sample holder, double-sided polyimide tape was applied to its back, ensuring stable placement during the experiment. Two platinum electrodes were positioned on top of the sample, separated from the substrate by a layer of double-sided polyimide tape. As the substrate is conductive, the tape prevented direct electrical contact between the electrodes while keeping them securely fixed in place. The platinum coils were arranged face-to-face on the lateral sides of the nanoantenna array, with one coil folded into a U-shape to increase the electric field lines passing through the cells. In addition, a film of polydimethylsiloxane (PDMS) was placed over each electrode, also separated by the double-sided polyimide tape, creating a 560- μm thick microfluidic chamber into which the cells were pipetted. A cover slip was placed over the PDMS layer to seal the chamber and protect the sample from the dark field condenser, which has a short working distance of 1.6 mm. To optimize the optical path, oil was applied between the condenser and the cover slip, as the condenser is an oil-immersion type with a NA of 1.3. Additionally, copper tape was attached to the substrate for auxiliary testing, though it was primarily used during the previous proof of concept involving the electrochemical cell.

An electrical stimulator developed by Prof. Bassani's group [99] was used to excite the isolated cardiomyocytes. The applied voltage consisted of a biphasic truncated exponential waveform, with each pulse lasting 2.5 ms at a frequency of 1 Hz. First, to ensure the platform was suitable for biological experiments, cardiomyocyte contraction was monitored to verify proper stimulation. Therefore, a mixture of 40 μ L of the storage solution containing the isolated cardiomyocytes and 500 μ L of Tyrode solution, which provides the necessary ions for the cells generate action potentials, was prepared. Fig. 5.8a and 5.8b show three cardiomyocytes before and after stimulation (a video recording is available online, see video 1). In these figures, the red and blue rectangles indicate the length of the cells before and after contraction, respectively. The visible shortening between the red and blue rectangles confirms the successful stimulation of the cardiomyocytes. Although each cell has its own voltage threshold for stimulation, the average voltage threshold observed in our experiments was 7.7 ± 1.7 V.

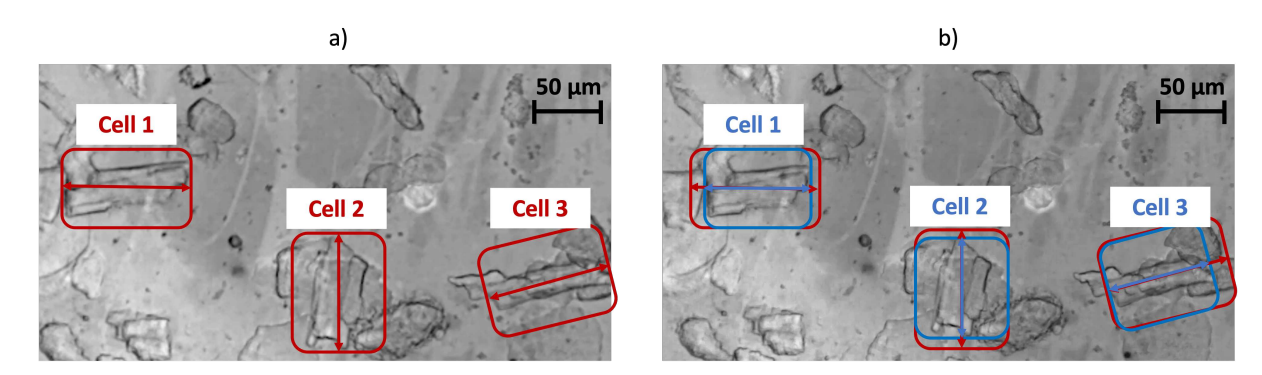


Figure 5.8: Isolated rat cardiomyocytes a) before (at rest) and b) after (contracted) electrical stimulation. The red rectangles indicate the total length of the cells at rest, while the blue rectangles show the new length when the cells are contracted.

After validating the cell stimulation platform, the complete ex-vivo biological experiment was performed. Fig. 5.9 and Fig. 5.10 illustrate the schematic and the complete setup, respectively. The experiment consisted of applying 500 μ L of the Tyrode solution, containing isolated cardiomyocyte cells, onto the substrate with the nanoantenna array. Simultaneously, the sample was illuminated by a white-light source and monitored through the CCD camera software to ensure the precise positioning and real-time observation. The electrical stimulator then applied voltage pulses between the platinum electrodes to excite the cells. Using the micropositioners of the setup, the sample was gradually adjusted to locate an area of the nanoantenna array where a single cardiomyocyte was present. Once the field of view (FOV) was established, the optical power meter was activated to record the scattered light generated by the nanoantennas, which responded to the electrical activity of the single cell. The procedure was repeated for a group of two cardiomyocytes, with the sample moved to a region containing two isolated cells. This allowed for the comparison of signals between individual cells and cell groups, showcasing the device's ability to monitor both scenarios with high spatial resolution.

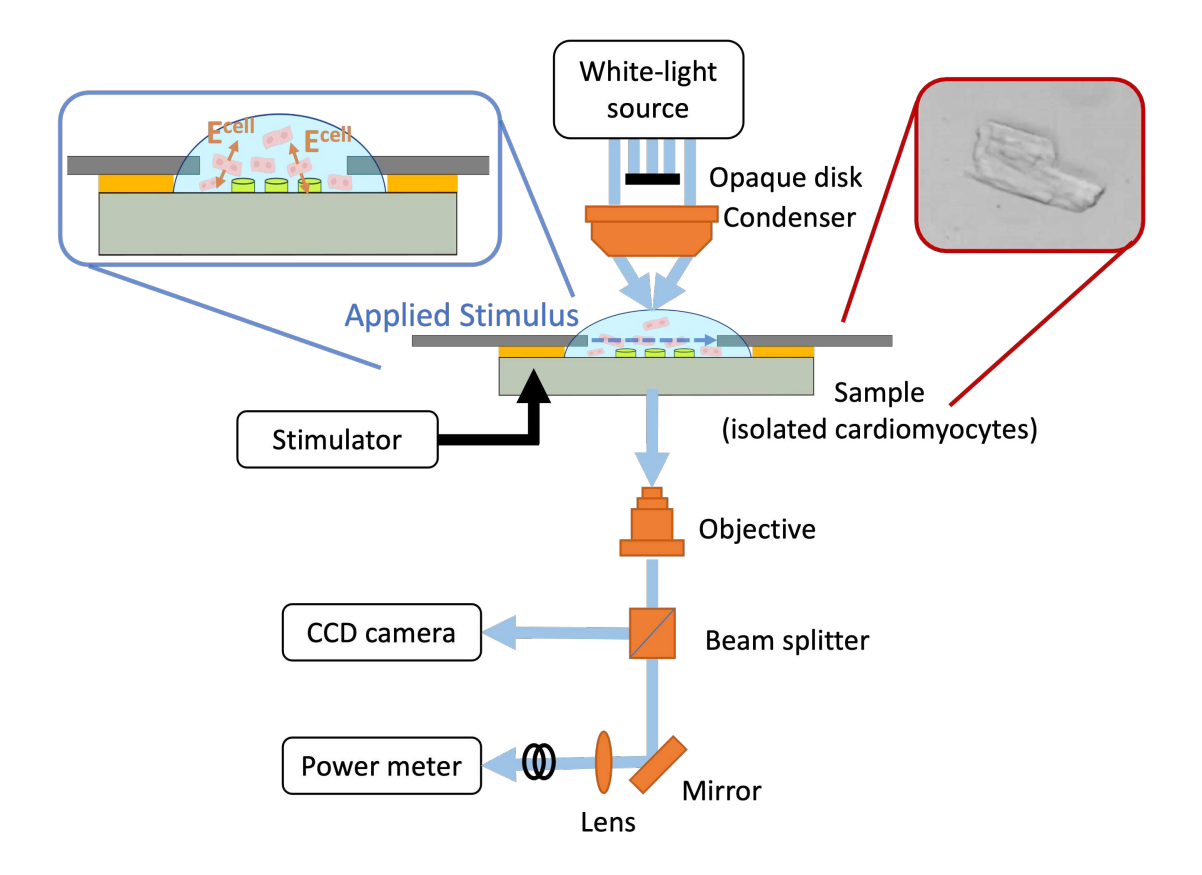


Figure 5.9: Schematic of the setup used for the plasmonic-based electrophysiological monitoring of cardiomyocytes.

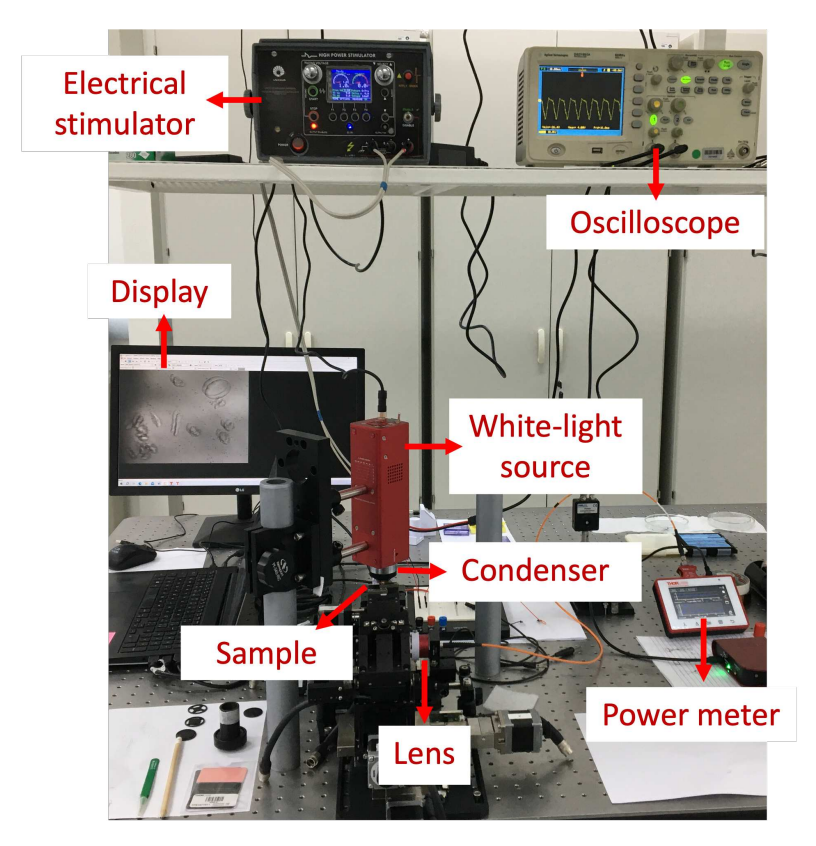


Figure 5.10: Implemented setup for the plasmonic-based electrophysiological monitoring of cardiomyocytes.

Fig. 5.11 shows the scattered light from the nanoantenna array when monitoring a single cardiomyocyte. As expected, the scattering signal was modulated in amplitude by the electric field generated by the stimulated cell. Since the nanoantennas are located just outside the cells (not on the cell membrane), the optical measurement corresponds to the extracellular field potential (EFP) of the rat isolated cardiomyocyte. Similarly, Fig. 5.12 illustrates the scattering light obtained from monitoring two cardiomyocytes. The profile of the optical signal differed from that of the single cell due to the spatial and temporal integration of the EFP from each individual cell, leading to a more complex waveform. These results demonstrate the capability of the plasmonic nanoantennas to monitor the electrophysiological activity of cells in real time, with high spatial resolution, label-free operation and wireless capabilities.

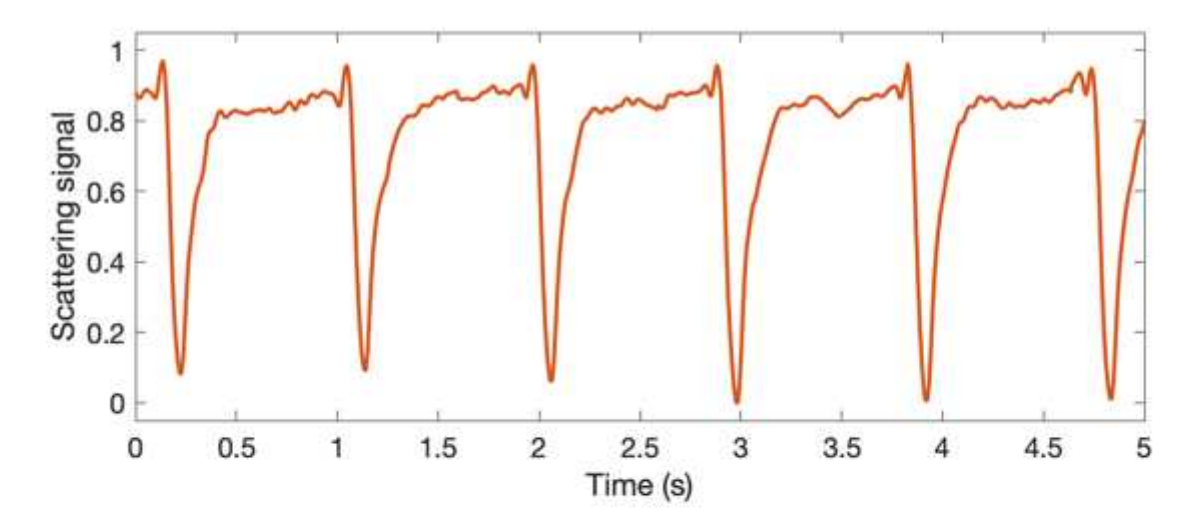


Figure 5.11: Scattering signal in response to the electrophysiological activity of a single cardiomyocyte.

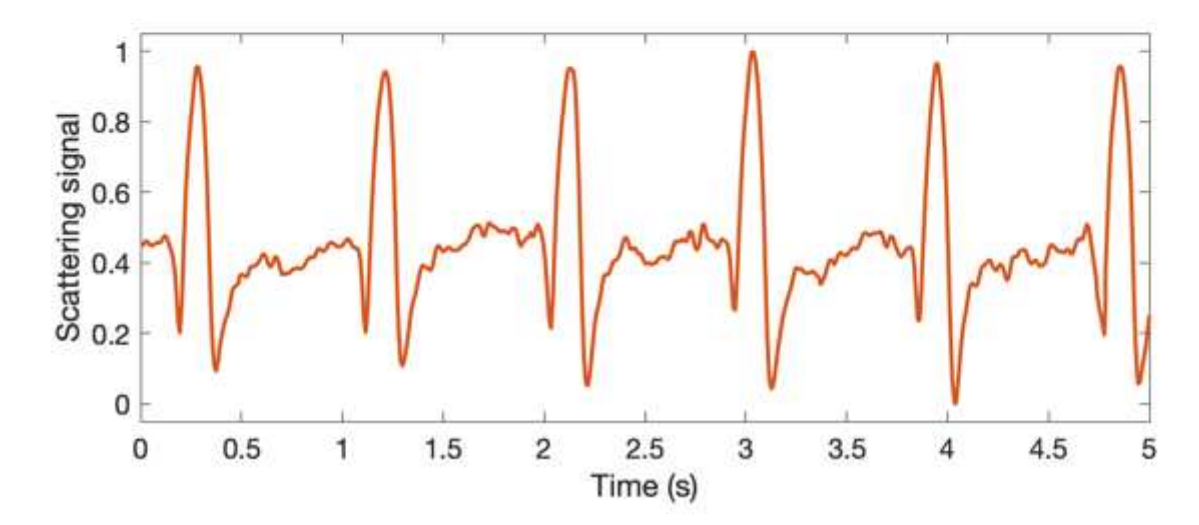


Figure 5.12: Scattering signal in response to the electrophysiological activity of a group of two cardiomyocytes.

To exclude the possibility that the recorded signal was due to the electric field directly generated by the stimulator rather than the cardiomyocytes, we conducted a control experiment. The optical response of the nanoantennas was recorded while voltage pulses were applied between the two platinum electrodes in the presence of Tyrode solution, but without any cells. As shown in Fig. 5.13, the scattering signal (blue curve) was not modulated by the applied electric field, indicating that the field did not reach the nanoantennas sufficiently. In contrast, when the same stimulus was applied between one platinum electrode and the conductive substrate, the electric field did pass through the nanoantennas, resulting in clear modulation of the scattered light (orange curve). This experiment confirmed that the optical signal obtained during the biological tests arises from the electrical activity of living cells and not from the externally applied stimulus.

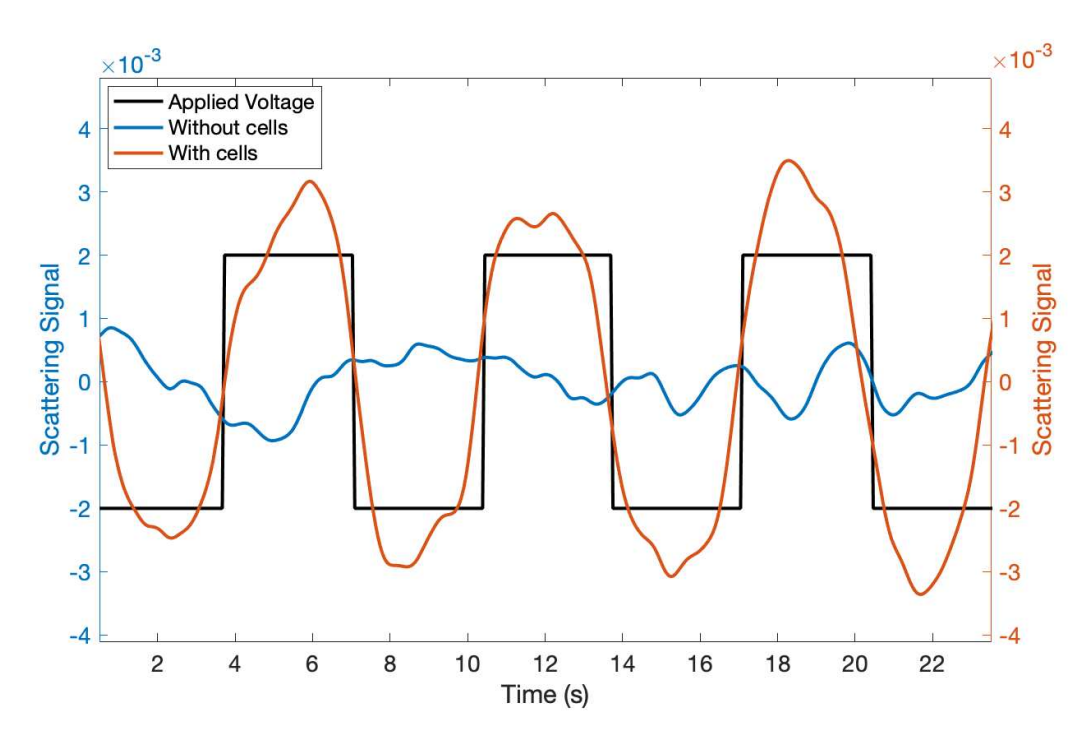


Figure 5.13: Validation that the optical far-field response corresponds to the electric field generated by the cardiomyocytes and not to the external stimulation. Control measurements without cells show no modulation (blue curve), confirming the recorded optical signal arises from cellular activity.

The modulation effect of the scattered light can also be qualitatively observed through computer vision analysis. The video available online (see video 2) shows the intensity variation in dark-field optical micrographs of the nanoantenna array during the electrical activity of cardiomyocytes. However, it is important to emphasize that this method does not offer the most precise measurement of the device's optical response. The CCD camera used in this study operates in the visible range, whereas the power meter employed for quantitative analysis was specifically tuned to detect the near-infrared (NIR) signal at 850 nm — within the resonance band of the nanoantennas. Furthermore, the video was not recorded directly through the CCD camera's acquisition software, but rather

from a computer monitor using a smartphone, as part of a longer documentation of the experiment. This limitation arose because computer vision analysis was not originally planned within the scope of the project. Despite these limitations, the observed variations in image intensity strongly suggest that computer vision techniques could serve as a valuable complementary tool for evaluating the optical modulation of the device. This opens a promising direction for future research focused on integrating image-based analysis with quantitative optical measurements.

In addition, to refine the experiment, a contraction inhibitor could be used to eliminate noise caused by the mechanical motion of the cells. In this study, the optical signal generated solely by the mechanical movement of the cells was compared to the signal produced by their electrical activity to assess the influence of contraction on the measurements. For this test, a solution containing cardiomyocytes was applied to a substrate without the nanoantenna array, and the field of view was adjusted to focus on a single cell. Using the same setup, the light passing through the substrate with the cardiomyocyte was recorded by the optical power meter. Variations in the collected light were observed due to the mechanical motion of the cells. This signal was then compared to the scattering signal recorded in the previous measurement by using the nanoantenna array, where the light was modulated by the extracellular electrical field of the cardiomyocytes. Fig. 5.14 shows the optical signals corresponding to the electrophysiological activity and the contractile movement of the cardiomyocytes.

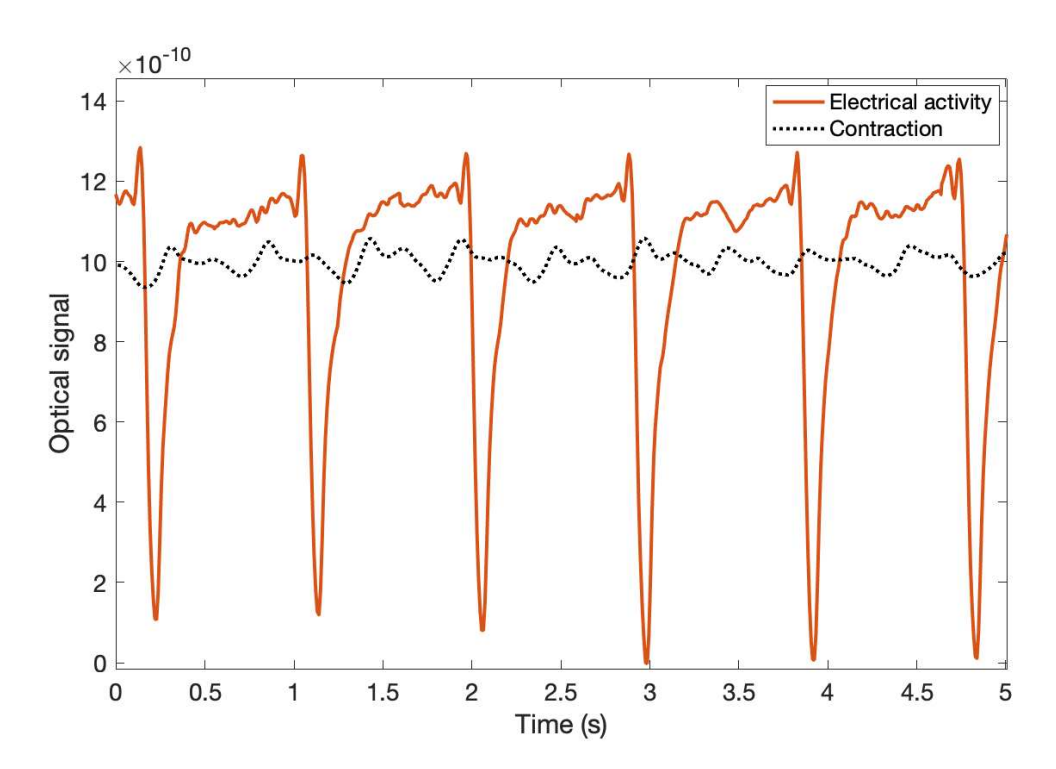


Figure 5.14: Comparison of optical signals corresponding to the electrophysiological activity and contractile movement of cardiomyocytes. The curves are presented without normalization to allow for direct comparison of signal intensity.

As seen, the two curves differ significantly in intensity and waveform. Moreover, the correlation coefficient between them is 0.0075, indicating a very weak linear relationship between the two signals. This confirms the reliability of the measurements, demonstrating that the detected optical signal primarily reflects the electrical activity of the cells rather than mechanical artifacts.

Although this experiment was carried out with cardiomyocytes, the proposed technique can also be applied to other excitable cells, such as neurons. In this case, the use of an inhibitor would not be necessary, as neurons do not exhibit contractile activity. Neurons can be stimulated electrically, but chemical methods involving neurotransmitters and pharmacological agents are also commonly employed.

Furthermore, to contextualize the most relevant outcomes of this study, Table 5.1 presents a comparative analysis between our results and previous works reported in the literature. Notably, all earlier studies demonstrated the functionality of plasmonic arrays as electrophysiological probes through *in-vitro* experiments. In these works, either stem cells [20] or embryonic-stage cells [21–23] were cultured under controlled conditions to form functional networks of neurons or cardiomyocytes. While these approaches are highly relevant and informative, our work advances toward a more physiologically realistic scenario. To the best of our knowledge, this is the first demonstration of a plasmonic device successfully performing ex-vivo electrophysiological measurements. Specifically, we isolated cardiomyocyte cells from adult rats and immediately recorded their electrical activity using the plasmonic nanoantennas - without requiring weeks of cell culturing or cellular differentiation. In addition, prior studies such as [20, 22] focused on networks of cardiomyocytes, capturing the collective electrical signals of large cell populations. In contrast, our device demonstrated the ability to resolve the electrical activity of a single cardiomyocyte, as well as a pair of cells, thereby evidencing the exceptionally high spatial resolution achieved by the nanoantenna array.

Table 5.1: Overview of plasmonic nanoantenna arrays for electrophysiology: experimental context and spatial precision.

Device format	Type of experiment	Spatial resolution	Reference
Nanodisk array	$In ext{-}vivo$	Single cardiomyocyte	This work
Nanodisk array	$In ext{-}vitro$	Network of cardiomyocytes	[20]
Pancake array	$In\mbox{-}vitro$	Single neuron	[21]
Nanowire array	In-vitro	Network of cardiomyocytes	[22]
Nanograting	In-vitro	Network of neurons	[23]

5.3 Conclusions

In this chapter, the second functionality of the developed nanoantenna array, focused on monitoring the electrophysiological activity of cells, was successfully demonstrated. First, a proof of concept was conducted using optoelectrochemical recordings. A controlled electrical field was applied across the nanoantenna array using a function generator, while the scattered light from the nanoantennas was recorded. The results showed that the scattering signal was clearly modulated in amplitude by the applied voltage pulses, validating the working principle of the device. Pulses with a duration of up to 40 ms were successfully monitored, though the technique is capable of sub-millisecond temporal resolution due to the high speed of photons [20,21].

The biological experiment was performed using cardiomyocyte cells isolated from rats. The procedure involved applying the cells to the nanoantenna array and stimulating them with an electrical stimulator. As in the proof of concept, the scattering signal from the nanoantennas was collected simultaneously. The recorded optical signal clearly reflected the extracellular field potential (EFP) of the cardiomyocytes, capturing the activity of both a single cell and a group of two cells. This demonstrated the ability of the device to monitor the electrophysiological activity of cells in both scenarios with high spatial resolution.

This result is particularly significant as, to the best of our knowledge, it marks the first ex-vivo recording of the electrical activity of a single cardiomyocyte using a plasmonic nanoantenna array. Unlike previous studies, which demonstrated optical recordings from neural cells [21,23] or cardiomyocyte networks [20,22] grown in culture, this work was conducted with freshly isolated cells from a adult living organism, offering a much more physiologically realistic scenario. By avoiding the use of stem cell-derived or embryonic cultures, our approach brings the technology closer to clinical relevance and in-vivo applications. Furthermore, the ability to monitor the electrical activity of an individual cardiomyocyte, as well as small groups of cells, demonstrates the exceptional spatial resolution of the device, which is also an unprecedented achievement for cardiomyocyte recordings using plasmonic techniques.

In conclusion, the potential of the plasmonic nanoantenna array as an electrooptical probe for monitoring cells was successfully demonstrated. The device's high spatiotemporal resolution, label-free operation, wireless capabilities, and real-time monitoring
make it a promising technique for studying various electrophysiologically active cells, such
as neurons, skeletal muscle cells, and certain endocrine and epithelial cells. Combined with
the biosensing functionality demonstrated in the previous chapter, the proposed device
becomes a powerful tool for comprehensive analysis of biological systems at both microand nanoscale levels.

Chapter 6

Conclusions and future perspectives

6.1 Conclusions

Nanotechnology is an emerging area that is being applied in various fields with extraordinary results. Its potential in biomedical field is very high due the capacity to interact directly with living systems at molecular level. In this work, we aimed to design, fabricate and characterize a device based on a plasmonic nanoantenna array with two functionalities, biomolecular sensing and monitoring electrophysiological activity of cells. For this, we took advantage of the Localized Surface Plasmon Resonance (LSPR) of metallic nanoparticles, which consists of electron oscillations confined in the metal-dielectric interface. This phenomenon is enhanced by the Surface Lattice Resonance (SLR), which consists in diffractive coupling effects in periodic arrays of nanoparticles. Both, a target molecule and the electric field generated by cells cause variations in the plasmonic response of the nanoantennas, allowing its use for biosensing and electrophysiological monitoring.

The novel device developed in this work was designed to operate in the Near-Infrared region (NIR-I), benefiting from reduced tissue absorption and bone reflection, making it suitable for potential in-vivo applications. Extensive electromagnetic simulations guided the optimization of the nanoantenna geometry, dimensions, and lattice configuration. The successful fabrication of the device followed a top-down approach, based on electron beam lithography, resulting in a 2×2 mm² array of 225-nm diameter gold nanodisks on an ITO-coated glass substrate. The optical characterization validated the device's performance, showcasing strong localized surface plasmon resonance (LSPR) and surface lattice resonance (SLR) effects, leading to choose the 600 nm period as the most suitable for our dual-application.

The biosensing capability of the device was evaluated through both proof-of-concept experiments using sucrose solutions, and biological experiments for cortisol detection. The plasmonic nanoantenna array exhibited excellent performance, achieving a sensitivity value of $471 \, \text{nm/RIU}$ and a figure of merit (FOM) of $8.3 \, \text{RIU}^{-1}$ for detecting

refractive index variations. Furthermore, biofunctionalization with cortisol-specific aptamers enabled precise and selective molecular detection. The device demonstrated a limit of detection (LoD) of 166.6 nM for cortisol, proving its potential for real-time monitoring of stress biomarkers. This biosensor represents a significant advancement toward label-free, miniaturized, and portable diagnostic platforms.

The electrophysiological monitoring capability of he device was rigorously validated through optoelectrochemical recordings and biological experiments using isolated cardiomyocytes from rats. The proof of concept demonstrated the device's ability to monitor millisecond voltage pulses through the modulation in amplitude of the scattered light. Building on this, the unprecedented ex-vivo experiments confirmed that the nanoantenna array successfully detected extracellular field potentials (EFPs) generated by the cardiomyocytes in a physiologically realistic environment. By recording both single-cell and multi-cell activities, the experiments showcased the high spatial resolution and sensitivity of the device. This capability positions the plasmonic nanoantenna array as a promising tool for investigating excitable cells, such as neurons and cardiomyocytes, potentially replacing traditional electrode-based methods by this novel wireless and minimal invasive technique.

This research integrated knowledge from plasmonics, nanofabrication, optical characterization, chemistry and biological sciences. It was developed through a collaborative effort between the Laboratory of Applied and Computational Electromagnetics (LEMAC) at UNICAMP and leading nanoscience research centers in Spain, including nanoGUNE, Donostia International Physics Center (DIPC), and the Materials Physics Center (CFM). Additionally, partnerships with the Laboratory of Electrochemistry, Electroanalytics, and Sensor Development (LEEDS) and the Laboratory of Cardiovascular Research (LPCV) at UNICAMP enriched the experimental framework, playing a crucial role in the success of the biological tests. These collaborations highlight the multidisciplinary nature of the project and its potential impact across multiple fields.

In conclusion, this doctoral thesis contributes significantly to the advancement of nanotechnology and its applications in biomedical engineering, setting a foundation for the development of versatile tools capable of integrating sensing and monitoring functionalities into a single device. Its dual functionalities open new possibilities for understanding cellular dynamics, allowing for more complete studies of living systems. Moreover, the research outcomes open pathways for broader applications in neuroscience, cardiology, and beyond, while paving the way for more compact and efficient diagnostic systems.

6.2 Future perspectives

This doctoral thesis has demonstrated the feasibility of detecting specific molecules and monitoring the electrical activity of cells through proof-of-concept tests and biological experiments. With both functionalities successfully achieved using the developed nanoantenna array, future work will focus on enhancing the usability of the device and adapting it for broader studies of living systems.

Integration of microfluidic platforms

To automate experiments, facilitate sample handling, and ensure precise results, integrating a microfluidic platform [100] into the device is a critical next step. This stage is currently being addressed with the rapid prototyping strategy [101] using a cutting plotter and a polyester layer with acrylic adhesive. Partial results of this integration are shown in Fig. 6.1. This advancement would streamline experimental workflows and expand the device's potential for high-throughput applications.

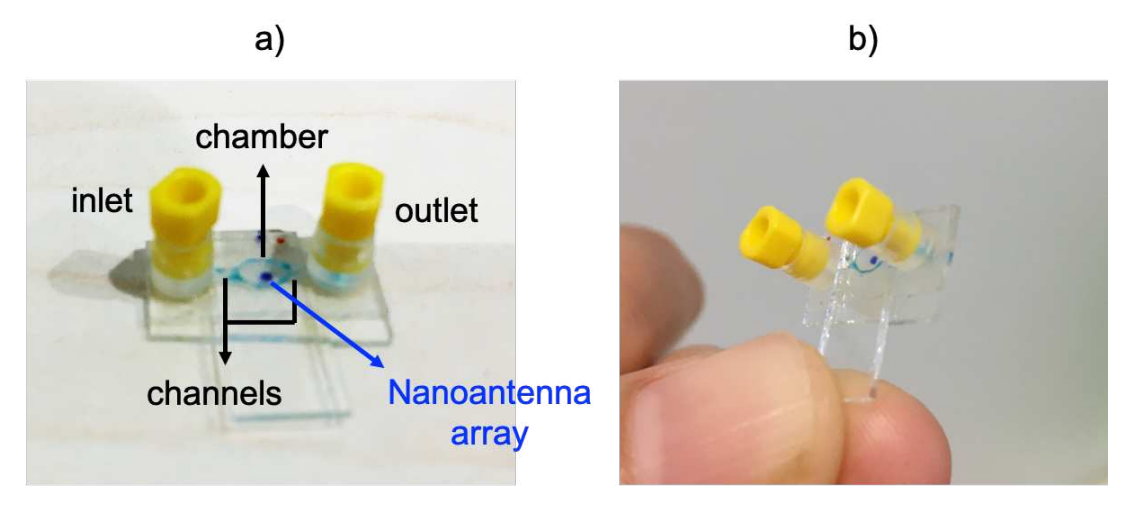


Figure 6.1: Integrated microfluidic platform with the nanoantenna array. a) Components. b) Visualization of the device, highlighting its scale.

Enhancing biosensing applications

Some strategies could be implemented during the biofunctionalization stage to reduce the limit of detection of the device:

- Using a lower pH buffer solution to increase the aptamer concentration on the gold regions.
- Applying a voltage to the substrate to strengthen the thiol linkage between the aptamers and gold nanodisks.

Additionally, multiplexed biodetection could be achieved by employing diverse aptamers to detect multiple analytes from the same biological sample through separate microfluidic channels and chambers. This approach could significantly broaden the device's utility in clinical and diagnostic settings.

Improving electrophysiological monitoring

Loading techniques could be employed to tune the optical response of the nanoantennas, thereby enhancing their performance. For instance, electro-optic polymers, which change their refractive index under an external electric field, could be used to increase the sensitivity of the electrophysiological probe [30]. As part of this effort, the polymer poly(3,4-ethylenedioxythiophene):polystyrene sulfonate (PEDOT:PSS) has been conformally deposited over the nanodisks using the electropolymerization technique. Fig. 6.2 illustrates the electropolymerization process and its results. Optical measurements and experiments are currently underway.

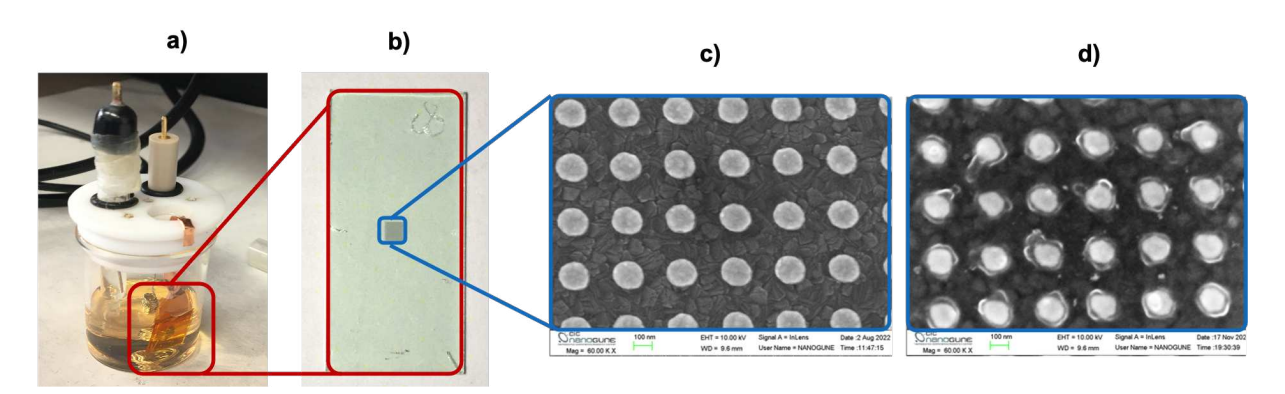


Figure 6.2: Nanoantenna array loaded with PEDOT:PSS. a) Electropolymerization process. b) Nanoantenna array configured as the working electrode. c) SEM image of the nanoantenna array before electropolymerization. d) SEM image after the PEDOT:PSS coating.

Expanding to other excitable cells

Future experiments will include measuring the electrical activity of other excitable cells, such as neurons. Given the complexity of the brain and its many unexplored mechanisms, this high spatio-temporal resolution technique has great potential for advancing neuroscience research. To this end, a glioma cell culture was successfully grown on a substrate with the nanoantenna array in collaboration with the Basque Health Research Biogipuzkoa. The micrographs in Fig. 6.3 illustrate the cells thriving in the array region. The next steps will involve culturing neurons and conducting experiments to assess their electrophysiological activity.

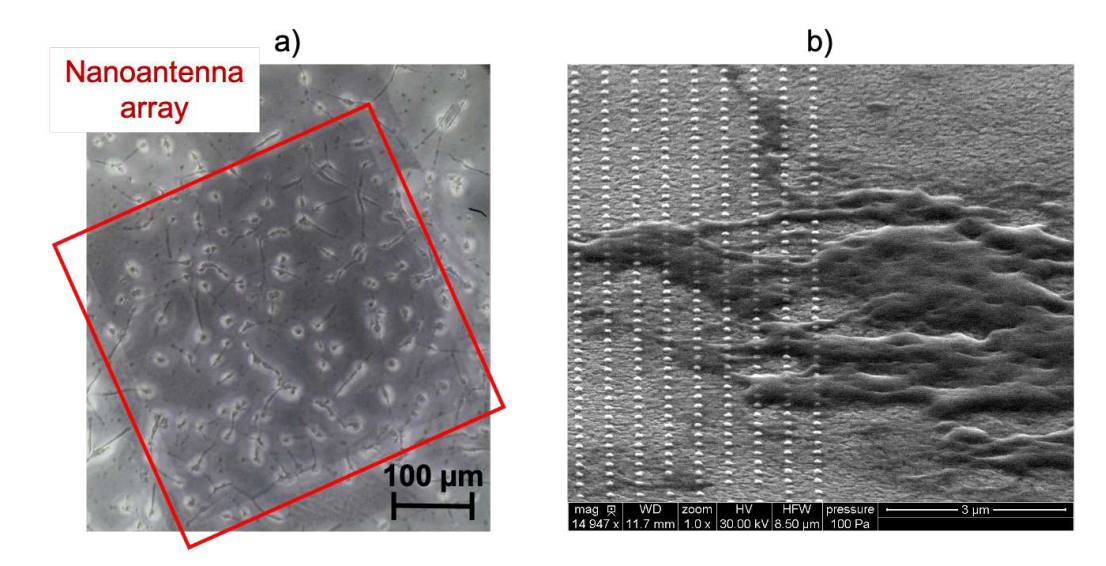


Figure 6.3: Glioma cell culture on the nanoantenna array. a) Optical micrograph showing the cell culture. b) SEM micrograph providing a closer view of the cells on the nanoantenna array.

Transitioning to *in-vivo* applications

Since the nanoantennas were designed to operate in the NIR-I band, they are well-suited for *in-vivo* applications due to the low scattering and absorption properties of deep tissues in this range. Future efforts will focus on designing and conducting *in-vivo* experiments through three potential approaches:

- Adapting the substrate to make it implantable.
- Fabricating the nanodisks directly onto optical fibers.
- Chemically synthesizing gold nanoparticles in colloidal form for easy delivery.

Exploring New Applications

The operating principle demonstrated in this work opens avenues for new applications of the developed device, including:

- Brain-computer interfaces (BCI) [102, 103] for advanced neural control.
- Monitoring organs for transplantation [104, 105].
- Complementing organ-on-a-chip (OoC) platforms [106] by providing high spatiotemporal resolution to study specific organ behavior.
- Multimodal integration [107], combining electrophysiological recordings with optical imaging, chemical sensing, and mechanical measurements to capture a wider spectrum of neural dynamics.

References

- [1] J. Kreuter, "Nanoparticles—a historical perspective," *International Journal of Pharmaceutics*, vol. 331, no. 1, pp. 1–10, 2007.
- [2] S. E. McNeil, "Nanotechnology for the biologist," *Journal of leukocyte biology*, vol. 78, no. 3, pp. 585–594, 2005.
- [3] M. Sharifi, F. Attar, A. A. Saboury, K. Akhtari, N. Hooshmand, A. Hasan, M. A. El-Sayed, and M. Falahati, "Plasmonic gold nanoparticles: Optical manipulation, imaging, drug delivery and therapy," *Journal of Controlled Release*, vol. 311, pp. 170–189, 2019.
- [4] B. Bhushan, "Introduction to nanotechnology," Springer handbook of nanotechnology, pp. 1–19, 2017.
- [5] M. Nasrollahzadeh, S. M. Sajadi, M. Sajjadi, and Z. Issaabadi, "Chapter 1 an introduction to nanotechnology," in *An Introduction to Green Nanotechnology* (M. Nasrollahzadeh, S. M. Sajadi, M. Sajjadi, Z. Issaabadi, and M. Atarod, eds.), vol. 28 of *Interface Science and Technology*, pp. 1–27, Elsevier, 2019.
- [6] R. P. Feynman, "There's plenty of room at the bottom [data storage]," *Journal of Microelectromechanical Systems*, vol. 1, no. 1, pp. 60–66, 1992.
- [7] A. Bogner, P.-H. Jouneau, G. Thollet, D. Basset, and C. Gauthier, "A history of scanning electron microscopy developments: Towards "wet-stem" imaging," *Micron*, vol. 38, no. 4, pp. 390–401, 2007. Microscopy of Nanostructures.
- [8] G. Binnig and H. Rohrer, "Scanning tunneling microscopy," Surface Science, vol. 126, no. 1, pp. 236–244, 1983.
- [9] C. Quate, "The afm as a tool for surface imaging," Surface Science, vol. 299-300, pp. 980-995, 1994.
- [10] J. T. Fourkas, J. Gao, Z. Han, H. Liu, B. Marmiroli, M. J. Naughton, J. S. Petersen, Y. Sun, A. Vagilio Pret, and Y. Zheng, "Grand challenges in nanofabrication: There remains plenty of room at the bottom," 2021.

[11] A. Kristoff, "How governments are fueling nanotech innovations." https://nano-magazine.com/news/2023/11/23/u4qsj8pro5yih98qe2rrmqp81ve6iu, 2023. Accessed: 2024-02-16.

- [12] National Nanotechnology Initiative, "Nni supplement to the president's 2023 budget," 2023.
- [13] NANORIGO, "Nanorigo overview." https://nanorigo.eu/about/, 2019.
- [14] EU-Japan Centre for Industrial Cooperation, "About nanotechnology." https://www.eu-japan.eu/eubusinessinjapan/sectors/nanotechnology/about-nanotechnology, 2023.
- [15] J. Qiu, "Nanotechnology development in china: challenges and opportunities," *National Science Review*, vol. 3, no. 1, pp. 148–152, 2016.
- [16] Ministério da Ciência, Tecnologia e Inovações (MCTI), "Plano de aÇÃo de ct&i para tecnologias convergentes e habilitadoras." https://antigo.mctic.gov.br/mctic/export/sites/institucional/tecnologia/tecnologiasSetoriais/Plano-de-Acao-em-CTI_Nanotecnologia_FINAL.pdf, 2019.
- [17] J. K. Wong, R. Mohseni, A. A. Hamidieh, R. E. MacLaren, N. Habib, and A. M. Seifalian, "Will nanotechnology bring new hope for gene delivery?," Trends in Biotechnology, vol. 35, no. 5, pp. 434–451, 2017.
- [18] A. Garcia-Etxarri and R. Yuste, "Time for nanoneuro," *Nature Methods*, vol. 18, no. 11, pp. 1287–1293, 2021.
- [19] K. E. Odening, A.-M. Gomez, D. Dobrev, L. Fabritz, F. R. Heinzel, M. E. Mangoni, C. E. Molina, L. Sacconi, G. Smith, M. Stengl, et al., "Esc working group on cardiac cellular electrophysiology position paper: relevance, opportunities, and limitations of experimental models for cardiac electrophysiology research," EP Europace, vol. 23, no. 11, pp. 1795–1814, 2021.
- [20] A. Habib, X. Zhu, U. I. Can, M. L. McLanahan, P. Zorlutuna, and A. A. Yanik, "Electro-plasmonic nanoantenna: A nonfluorescent optical probe for ultrasensitive label-free detection of electrophysiological signals," *Science advances*, vol. 5, no. 10, p. eaav9786, 2019.
- [21] J. Zhang, T. Atay, and A. V. Nurmikko, "Optical detection of brain cell activity using plasmonic gold nanoparticles," *Nano letters*, vol. 9, no. 2, pp. 519–524, 2009.
- [22] S. Akbari, S. Hamidi, H. Eftekhari, and A. Heirani-Tabasi, "Fast electro-plasmonic detection of heart signal in balb/c cells onto one-dimensional plasmonic grating," *PloS one*, vol. 18, no. 3, p. e0282863, 2023.

[23] H. J. Kadhim, H. Al-Mumen, H. Nahi, and S. Hamidi, "Dopamine-induced neural activity detection onto a cell-cultured plasmonic nanograting platform," *Applied Physics A*, vol. 129, no. 5, p. 323, 2023.

- [24] D. K. Gramotnev and S. I. Bozhevolnyi, "Plasmonics beyond the diffraction limit," Nature photonics, vol. 4, no. 2, pp. 83–91, 2010.
- [25] R. Ritchie, "Surface plasmons in solids," Surface Science, vol. 34, no. 1, pp. 1–19, 1973.
- [26] W. L. Barnes, A. Dereux, and T. W. Ebbesen, "Surface plasmon subwavelength optics," *nature*, vol. 424, no. 6950, pp. 824–830, 2003.
- [27] F. Tam, G. P. Goodrich, B. R. Johnson, and N. J. Halas, "Plasmonic enhancement of molecular fluorescence," *Nano letters*, vol. 7, no. 2, pp. 496–501, 2007.
- [28] M. L. Brongersma and P. G. Kik, Surface plasmon nanophotonics, vol. 131. Springer, 2007.
- [29] S. A. Maier, *Plasmonics: fundamentals and applications*. Springer Science & Business Media, 2007.
- [30] A. Habib, X. Zhu, S. Fong, and A. A. Yanik, "Active plasmonic nanoantenna: an emerging toolbox from photonics to neuroscience," *Nanophotonics*, vol. 1, no. ahead-of-print, 2020.
- [31] R. F. Graf, Modern dictionary of electronics. Newnes, 1999.
- [32] P. Muehlschlegel, H.-J. Eisler, O. J. Martin, B. Hecht, and D. Pohl, "Resonant optical antennas," *science*, vol. 308, no. 5728, pp. 1607–1609, 2005.
- [33] H. D. Herath and Y. S. Hu, "Unveiling nanoparticle-immune interactions: how superresolution imaging illuminates the invisible," *Nanoscale*, vol. 17, no. 3, pp. 1213–1224, 2025.
- [34] R. Boudries, H. Williams, S. Paquereau-Gaboreau, S. Bashir, M. Hojjat Jodaylami, M. Chisanga, L.-É. Trudeau, and J.-F. Masson, "Surface-enhanced raman scattering nanosensing and imaging in neuroscience," ACS nano, vol. 18, no. 34, pp. 22620–22647, 2024.
- [35] S. Abayzeed, D. Galvis, K. Regules Medel, O. Barajas Gonzalez, K. Setchfield, M. G. Somekh, K. C. Wedgwood, and P. A. Smith, "Plasmonic imaging of living pancreatic beta-cell networks," bioRxiv, pp. 2025–04, 2025.

[36] T. L. Vasconcelos, B. S. Archanjo, B. Fragneaud, B. S. Oliveira, J. Riikonen, C. Li, D. S. Ribeiro, C. Rabelo, W. N. Rodrigues, A. Jorio, et al., "Tuning localized surface plasmon resonance in scanning near-field optical microscopy probes," ACS nano, vol. 9, no. 6, pp. 6297–6304, 2015.

- [37] M. Dipalo, G. C. Messina, H. Amin, R. La Rocca, V. Shalabaeva, A. Simi, A. Maccione, P. Zilio, L. Berdondini, and F. De Angelis, "3d plasmonic nanoantennas integrated with mea biosensors," *Nanoscale*, vol. 7, no. 8, pp. 3703–3711, 2015.
- [38] B. Desbiolles, J. Hanna, R. Ausilio, M. A. Leccardi, Y. Yu, and D. Sarkar, "Organic electro-scattering antenna: Wireless and multisite probing of electrical potentials with high spatial resolution," *Science Advances*, vol. 10, no. 51, p. eadr8380, 2024.
- [39] H. Ahn, S. Kim, Y. Kim, S. Kim, J.-r. Choi, and K. Kim, "Plasmonic sensing, imaging, and stimulation techniques for neuron studies," *Biosensors and Bioelectronics*, p. 113150, 2021.
- [40] Y. Li, D. Li, C. Chi, and B. Huang, "Achieving strong field enhancement and light absorption simultaneously with plasmonic nanoantennas exploiting film-coupled triangular nanodisks," *The Journal of Physical Chemistry C*, vol. 121, no. 30, pp. 16481–16490, 2017.
- [41] M. L. De la Chapelle and A. Pucci, Nanoantenna: Plasmon-Enhanced Spectroscopies for Biotechnological Applications, vol. 1. CRC Press, 2013.
- [42] S. A. Maier and H. A. Atwater, "Plasmonics: Localization and guiding of electromagnetic energy in metal/dielectric structures," *Journal of applied physics*, vol. 98, no. 1, p. 10, 2005.
- [43] M. J. Madou, Manufacturing techniques for microfabrication and nanotechnology, vol. 2. CRC press, 2011.
- [44] S. Franssila, Introduction to microfabrication. John Wiley & Sons, 2010.
- [45] A. Sarangan, Nanofabrication: Principles to Laboratory Practice. CRC Press, 2016.
- [46] A. Pimpin and W. Srituravanich, "Review on micro-and nanolithography techniques and their applications," *Engineering Journal*, vol. 16, no. 1, pp. 37–56, 2012.
- [47] S. Boden and X. Shi, "Helium ion beam lithography for sub-10nm pattern definition," SPIE Newsroom, 2017.
- [48] Dracula Technologies, "Thin film processing method," 2024.

[49] Lesker, "PRO Line PVD 75 Deposition Platform." https://www.lesker.com/process-equipment-division/thin-film-systems/pro-line-pvd-75-deposition-platform.cfm#performance. [Accessed: May 16, 2024].

- [50] Y. B. Gianchandani, O. Tabata, and H. P. Zappe, *Comprehensive microsystems*, vol. 1. Elsevier Amsterdam, 2008.
- [51] O. Ostroverkhova, Handbook of Organic Materials for Electronic and Photonic Devices. Woodhead Publishing, 2018.
- [52] IUPAC, Glossary for chemists of terms used in biotechnology (IUPAC Recommendations 1992), vol. 64. 1992. p. 148.
- [53] H. K. Hunt and A. M. Armani, "Label-free biological and chemical sensors," Nanoscale, vol. 2, no. 9, pp. 1544–1559, 2010.
- [54] P. Patel, V. Mishra, and A. Mandloi, "Optical biosensors: Fundamentals & trends," *JERS*, vol. 1, no. 1, pp. 15–34, 2010.
- [55] A. B. González, A Bimodal Waveguide Interferometer Device Based on Silicon Photonics Technology for Label-free and High Sensitive Biosensing. PhD thesis, Universitat Autònoma de Barcelona, Barcelona, Spain, 2012.
- [56] M.-C. Estevez, M. A. Otte, B. Sepulveda, and L. M. Lechuga, "Trends and challenges of refractometric nanoplasmonic biosensors: A review," *Analytica chimica acta*, vol. 806, pp. 55–73, 2014.
- [57] J. D. J. Homola, "Springer ser chem sens biosens (2006) 4: 191–206," Surface Plasmon Resonance Based Sensors, vol. 4, pp. 191–206, 2006.
- [58] B. Bassols-Cornudella, P. Ramirez-Priego, M. Soler, M.-C. Estévez, H. J. D. Luis-Ravelo, M. Cardenosa-Rubio, and L. M. Lechuga, "Novel sensing algorithm for linear read-out of bimodal waveguide interferometric biosensors," *Journal of Lightwave Technology*, vol. 40, no. 1, pp. 237–244, 2022.
- [59] M. Carter and J. C. Shieh, "Chapter 4 electrophysiology," in Guide to Research Techniques in Neuroscience (M. Carter and J. C. Shieh, eds.), pp. 91–118, New York: Academic Press, 2010.
- [60] R. B. Reilly and T. C. Lee, "Electrograms (ecg, eeg, emg, eog)," *Technology and Health Care*, vol. 18, no. 6, pp. 443–458, 2010.
- [61] M. Scanziani and M. Häusser, "Electrophysiology in the age of light," Nature, vol. 461, no. 7266, pp. 930–939, 2009.

[62] J. Viventi, D.-H. Kim, L. Vigeland, E. S. Frechette, J. A. Blanco, Y.-S. Kim, A. E. Avrin, V. R. Tiruvadi, S.-W. Hwang, A. C. Vanleer, et al., "Flexible, foldable, actively multiplexed, high-density electrode array for mapping brain activity in vivo," Nature neuroscience, vol. 14, no. 12, p. 1599, 2011.

- [63] J. S. Choi, H. J. Lee, S. Rajaraman, and D.-H. Kim, "Recent advances in three-dimensional microelectrode array technologies for in vitro and in vivo cardiac and neuronal interfaces," *Biosensors and Bioelectronics*, vol. 171, p. 112687, 2021.
- [64] G. Hong and C. M. Lieber, "Novel electrode technologies for neural recordings," Nature Reviews Neuroscience, vol. 20, no. 6, pp. 330–345, 2019.
- [65] M. E. J. Obien, K. Deligkaris, T. Bullmann, D. J. Bakkum, and U. Frey, "Revealing neuronal function through microelectrode array recordings," Frontiers in neuroscience, vol. 8, p. 423, 2015.
- [66] J. Li, H. Ding, Y. Wang, and J. Yang, "Advances in optical recording techniques for non-invasive monitoring of electrophysiological signals," *Journal of Physics D: Applied Physics*, vol. 57, no. 49, p. 493001, 2024.
- [67] N. S. Mousavi, K. B. Ramadi, Y.-A. Song, and S. Kumar, "Plasmonics for neuroengineering," *Communications Materials*, vol. 4, no. 1, p. 101, 2023.
- [68] B. Hille, "Ion channels of excitable membranes third edition," (No Title), 2001.
- [69] C. Bédard and A. Destexhe, "Macroscopic models of local field potentials and the apparent 1/f noise in brain activity," *Biophysical journal*, vol. 96, no. 7, pp. 2589–2603, 2009.
- [70] G. Buzsáki, C. A. Anastassiou, and C. Koch, "The origin of extracellular fields and currents—eeg, ecog, lfp and spikes," *Nature reviews neuroscience*, vol. 13, no. 6, pp. 407–420, 2012.
- [71] S. Sylantyev, L. P. Savtchenko, Y.-P. Niu, A. I. Ivanov, T. P. Jensen, D. M. Kullmann, M.-Y. Xiao, and D. A. Rusakov, "Electric fields due to synaptic currents sharpen excitatory transmission," *Science*, vol. 319, no. 5871, pp. 1845–1849, 2008.
- [72] B. Sun, Y. Gou, Y. Ma, X. Zheng, R. Bai, A. A. A. Abdelmoaty, and F. Hu, "Investigate electrochemical immunosensor of cortisol based on gold nanoparticles/magnetic functionalized reduced graphene oxide," *Biosensors and Bioelectronics*, vol. 88, pp. 55–62, 2017.
- [73] A. Kaushik, A. Vasudev, S. K. Arya, S. K. Pasha, and S. Bhansali, "Recent advances in cortisol sensing technologies for point-of-care application," *Biosensors and Bioelectronics*, vol. 53, pp. 499–512, 2014.

[74] P. K. Vabbina, A. Kaushik, N. Pokhrel, S. Bhansali, and N. Pala, "Electrochemical cortisol immunosensors based on sonochemically synthesized zinc oxide 1d nanorods and 2d nanoflakes," *Biosensors and Bioelectronics*, vol. 63, pp. 124–130, 2015.

- [75] H. Windisch, H. Ahammer, P. Schaffer, W. Müller, and D. Platzer, "Optical multisite monitoring of cell excitation phenomena in isolated cardiomyocytes," *Pflügers Archiv*, vol. 430, pp. 508–518, 1995.
- [76] G. M. Roth, D. M. Bader, and E. R. Pfaltzgraff, "Isolation and physiological analysis of mouse cardiomyocytes," *JoVE* (*Journal of Visualized Experiments*), no. 91, p. e51109, 2014.
- [77] T.-M. Liu, J. Conde, T. Lipiński, A. Bednarkiewicz, and C.-C. Huang, "Revisiting the classification of nir-absorbing/emitting nanomaterials for in vivo bioapplications," *NPG Asia Materials*, vol. 8, no. 8, pp. e295–e295, 2016.
- [78] B. Auguié and W. L. Barnes, "Diffractive coupling in gold nanoparticle arrays and the effect of disorder," *Optics letters*, vol. 34, no. 4, pp. 401–403, 2009.
- [79] L. Kastrup and S. W. Hell, "Absolute optical cross section of individual fluorescent molecules," Angewandte Chemie International Edition, vol. 43, no. 48, pp. 6646–6649, 2004.
- [80] H. Bahador and H. Heidarzadeh, "A new proposal for highly sensitive refractive index sensor using vertically coupled plasmonic elliptic-disk up elliptic-ring nanoparticles," *Plasmonics*, vol. 16, no. 4, pp. 1223–1230, 2021.
- [81] S. Wang, X. Sun, M. Ding, G. Peng, Y. Qi, Y. Wang, and J. Ren, "The investigation of an lspr refractive index sensor based on periodic gold nanorings array," *Journal of Physics D: Applied Physics*, vol. 51, no. 4, p. 045101, 2018.
- [82] Y. Shen, J. Zhou, T. Liu, Y. Tao, R. Jiang, M. Liu, G. Xiao, J. Zhu, Z.-K. Zhou, X. Wang, et al., "Plasmonic gold mushroom arrays with refractive index sensing figures of merit approaching the theoretical limit," Nature communications, vol. 4, no. 1, p. 2381, 2013.
- [83] Y. Liang, L. Li, M. Lu, H. Yuan, Z. Long, W. Peng, and T. Xu, "Comparative investigation of sensing behaviors between gap and lattice plasmon modes in a metallic nanoring array," *Nanoscale*, vol. 10, no. 2, pp. 548–555, 2018.
- [84] G. Abdi and H. Bahador, "High sensitivity and optimum design of lspr-based sensors by coupled nano-rings for cancer detection," Optics and Lasers in Engineering, vol. 174, p. 107975, 2024.

[85] Y. Yang, J. Murray, J. Haverstick, R. A. Tripp, and Y. Zhao, "Silver nanotriangle array based lspr sensor for rapid coronavirus detection," *Sensors and Actuators B: Chemical*, vol. 359, p. 131604, 2022.

- [86] K. E. Chong, H. W. Orton, I. Staude, M. Decker, A. E. Miroshnichenko, I. Brener, Y. S. Kivshar, and D. N. Neshev, "Refractive index sensing with fano resonances in silicon oligomers," *Philosophical Transactions of the Royal Society A: Mathematical*, *Physical and Engineering Sciences*, vol. 375, no. 2090, p. 20160070, 2017.
- [87] E. R. De Kloet, M. Joëls, and F. Holsboer, "Stress and the brain: from adaptation to disease," *Nature reviews neuroscience*, vol. 6, no. 6, pp. 463–475, 2005.
- [88] S. S. Dickerson and M. E. Kemeny, "Acute stressors and cortisol responses: a theoretical integration and synthesis of laboratory research.," *Psychological bulletin*, vol. 130, no. 3, p. 355, 2004.
- [89] S. Jo, W. Lee, J. Park, W. Kim, W. Kim, G. Lee, H.-J. Lee, J. Hong, and J. Park, "Localized surface plasmon resonance aptasensor for the highly sensitive direct detection of cortisol in human saliva," Sensors and Actuators B: Chemical, vol. 304, p. 127424, 2020.
- [90] L. Cantelli, W. J. Paschoalino, S. Kogikosky Jr, T. M. Pessanha, and L. T. Kubota, "Dna super-lattice-based aptasensor for highly sensitive and selective detection of cortisol," *Biosensors and Bioelectronics: X*, vol. 12, p. 100228, 2022.
- [91] DRG Instruments GmbH, "Salivary cortisol ELISA." https://www.drg-diagnostics.de/files/slv-2930_ifu--cortisol-salivary_2023-11-30_14.0_endeit.pdf, 2024. Accessed: September 2, 2024.
- [92] T. Iqbal, A. Elahi, W. Wijns, and A. Shahzad, "Cortisol detection methods for stress monitoring in connected health," *Health Sciences Review*, vol. 6, p. 100079, 2023.
- [93] H. Jung, J. Jung, Y.-H. Kim, D. Kwon, B.-G. Kim, H. B. Na, and H. H. Lee, "Surface plasmon resonance characteristics of au nanoparticles layered sensor chip for direct detection of stress hormone conjugated by nanoparticles," *BioChip Journal*, vol. 12, pp. 249–256, 2018.
- [94] C. M. Hill, Fundamental and applied studies of organic photovoltaic systems. The University of Alabama, 2014.
- [95] L. B. Penna and R. A. Bassani, "Increased spontaneous activity and reduced inotropic response to catecholamines in ventricular myocytes from footshock-stressed rats," *Stress*, vol. 13, no. 1, pp. 73–82, 2010.

[96] B. M. Carvalho, R. A. Bassani, K. G. Franchini, and J. W. Bassani, "Enhanced calcium mobilization in rat ventricular myocytes during the onset of pressure overload-induced hypertrophy," American Journal of Physiology-Heart and Circulatory Physiology, vol. 291, no. 4, pp. H1803–H1813, 2006.

- [97] D. Li, J. Wu, Y. Bai, X. Zhao, and L. Liu, "Isolation and culture of adult mouse cardiomyocytes for cell signaling and in vitro cardiac hypertrophy," *Journal of visualized experiments: JoVE*, no. 87, 2014.
- [98] A. M. Nicks, S. R. Holman, A. Y. Chan, M. Tsang, P. E. Young, D. T. Humphreys, N. Naqvi, A. Husain, M. Li, N. J. Smith, et al., "Standardised method for cardiomyocyte isolation and purification from individual murine neonatal, infant, and adult hearts," *Journal of Molecular and Cellular Cardiology*, vol. 170, pp. 47–59, 2022.
- [99] A. R. de Santana, J. W. M. Bassani, and R. A. Bassani, "Comparison of shock-induced damage by different waveforms assessed by spontaneous contractions in rat myocytes," in *Proceedings of the 47th Annual Meeting of the Brazilian Biophysical Society*, vol. 1, p. 164858, Brazilian Biophysical Society, Galoá, 2023.
- [100] W. Wang, W. Su, J. Han, W. Song, X. Li, C. Xu, Y. Sun, and L. Wang, "Microfluidic platforms for monitoring cardiomyocyte electromechanical activity," *Microsystems & Nanoengineering*, vol. 11, no. 1, p. 4, 2025.
- [101] Z. Li, N. Haridas, S. Kaaliveetil, Y.-H. Cheng, C. Chande, V. Perez, A. K. Miri, and S. Basuray, "Low-cost rapid prototyping for microfluidics using parafilm®-based microchannels for low resource settings," Sensors and Actuators B: Chemical, vol. 404, p. 135212, 2024.
- [102] K. Liao, Z. Yang, D. Tao, L. Zhao, N. Pires, C. A. Dorao, B. T. Stokke, L. E. Roseng, W. Liu, and Z. Jiang, "Exploring the intersection of brain-computer interfaces and quantum sensing: a review of research progress and future trends," Advanced Quantum Technologies, vol. 7, no. 1, p. 2300185, 2024.
- [103] A. A. Ahmed, N. Alegret, B. Almeida, R. Alvarez-Puebla, A. M. Andrews, L. Ballerini, J. J. Barrios-Capuchino, C. Becker, R. H. Blick, S. Bonakdar, et al., "Interfacing with the brain: How nanotechnology can contribute," ACS nano, vol. 19, no. 11, pp. 10630–10717, 2025.
- [104] Y. Song, Y. Wang, W. Wang, Y. Xie, J. Zhang, J. Liu, Q. Jin, W. Wu, H. Li, J. Wang, et al., "Advancements in noninvasive techniques for transplant rejection: from biomarker detection to molecular imaging," Journal of Translational Medicine, vol. 23, no. 1, p. 147, 2025.

[105] R. Zhang, P. Shen, Y. Xiong, T. Wu, G. Wang, Y. Wang, L. Zhang, H. Yang, W. He, J. Du, et al., "Bright, photostable and long-circulating nir-ii nanoparticles for whole-process monitoring and evaluation of renal transplantation," National Science Review, vol. 11, no. 2, p. nwad286, 2024.

- [106] K. M. Świst-Szulik, "Organ on a chip in nanotechnology," in *Human Organs-on-a-Chip Technology*, pp. 215–231, Elsevier, 2024.
- [107] M. Ramezani, Y. Ren, E. Cubukcu, and D. Kuzum, "Innovating beyond electrophysiology through multimodal neural interfaces," *Nature Reviews Electrical Engineering*, pp. 1–16, 2024.
- [108] A. L. Washburn and R. C. Bailey, "Photonics-on-a-chip: recent advances in integrated waveguides as enabling detection elements for real-world, lab-on-a-chip biosensing applications," Analyst, vol. 136, no. 2, pp. 227–236, 2011.
- [109] M. C. Estevez, M. Alvarez, and L. M. Lechuga, "Integrated optical devices for lab-on-a-chip biosensing applications," *Laser & Photonics Reviews*, vol. 6, no. 4, pp. 463–487, 2012.
- [110] D. Grajales, A. F. Gavela, C. Domínguez, J. R. Sendra, and L. M. Lechuga, "Low-cost vertical taper for highly efficient light in-coupling in bimodal nanointerferometric waveguide biosensors," *Journal of Physics: Photonics*, vol. 1, no. 2, p. 025002, 2019.
- [111] U. F. Roggero and H. E. Hernández-Figueroa, "Polymeric power splitters for multiplexing optical biosensors," Optics & Laser Technology, vol. 127, p. 106127, 2020.
- [112] U. F. Roggero, R. E. Rubio-Noriega, A. Seifert, and H. E. Hernández-Figueroa, "Highly selective, compact and efficient vertical in-coupling for interferometric optical biosensors," in *Journal of Physics: Conference Series*, vol. 2407, p. 012045, IOP Publishing, 2022.
- [113] J. C. Ramirez, J. N. Schianti, M. G. Almeida, A. Pavani, R. R. Panepucci, H. E. Hernandez-Figueroa, and L. H. Gabrielli, "Low-loss modified su-8 waveguides by direct laser writing at 405 nm," *Optical Materials Express*, vol. 7, no. 7, pp. 2651–2659, 2017.
- [114] S. Anbumani, A. M. da Silva, U. F. Roggero, A. M. Silva, H. E. Hernández-Figueroa, and M. A. Cotta, "Oxygen plasma-enhanced covalent biomolecule immobilization on su-8 thin films: A stable and homogenous surface biofunctionalization strategy," Applied Surface Science, vol. 553, p. 149502, 2021.

[115] J. R. Fernández, V. d. O. Freire, and H. E. Hernandez-Figueroa, "Ti/au layers impact in prism-based plasmonic sensing of ethanol-fuel purity detection," in 2022 SBFoton International Optics and Photonics Conference (SBFoton IOPC), pp. 1–5, IEEE, 2022.

Appendix A

Supplementary chapter

Integrated Optical Sensor for Sucrose Detection based on Multimode Interferometry and Image Analysis

Over the past two decades, a major challenge for state-of-the-art optical biosensors has been their ability to function effectively in uncontrolled environments outside the laboratory. Key limitations include inefficient optical coupling, high fabrication complexity and costs, as well as the absence of a robust detection method [108–112]. In this supplementary chapter, a novel approach is proposed based on a pigtailed polymeric optical biosensor designed to be mass-producible and operable outside controlled laboratory settings. This study focuses on the design, simulation, and optimization of an optomechanical configuration that accounts for real fabrication constraints, paving the way for practical implementation. First, a vertical in-coupling mechanism was introduced, which consists of an etched optical fiber coupled to a non-linear inverted taper. At this stage, high-order even modes are selectively coupled into the taper and subsequently propagated through a multimode waveguide. Then, a ridge waveguide with a straight configuration was chosen due to its fabrication simplicity compared to rib or pedestal structures while also minimizing losses associated with curved paths. Additionally, the taper structure eliminates the need for nanometric dimensions typically required by grating couplers. The entire platform was based on SU-8 polymer, a material selected for its low cost and straightforward fabrication process compared to traditional silicon-based platforms [113, 114].

In this system, the waveguide functions as a transducer, where the interferometric pattern formed by the interaction of propagating modes is affected by changes in the surrounding refractive index. The resulting interference pattern at the waveguide output was designed to be captured by a CCD camera and subsequently processed to determine the sensor's sensitivity. Fig. A.1 illustrates the operating principle of the proposed device.

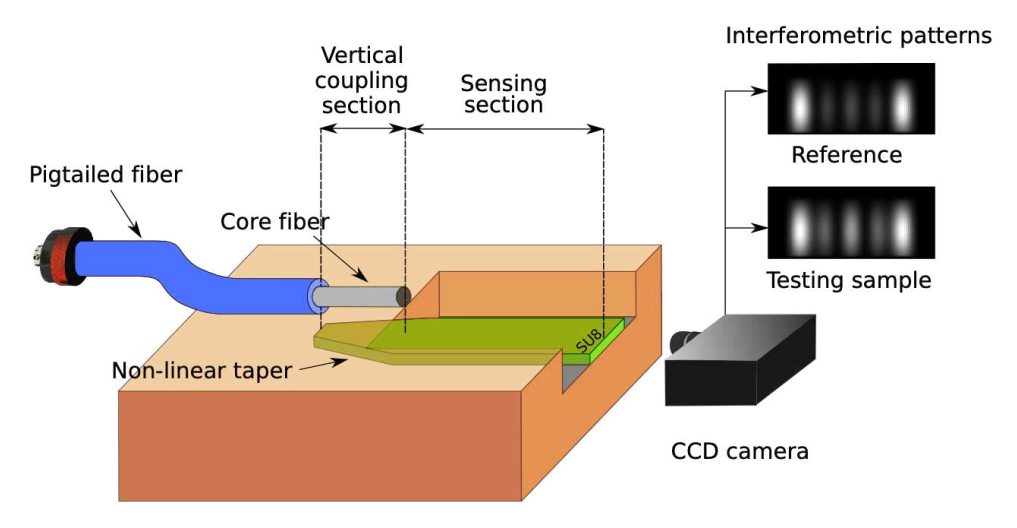


Figure A.1: General scheme of the integrated optical biosensor based on the comparison of interferometric patterns.

Methods

The operating wavelength of the integrated biosensor is set to 633 nm, as most biological fluids exhibit minimal light absorption in this spectral range. The device is based on a ridge waveguide structure consisting of a SiO₂ cladding and an SU-8 polymer core. Optical coupling is achieved using a single-mode optical fiber (SM600, Thorlabs), whose germanosilicate core has a diameter of 3.5 μ m. To optimize coupling efficiency, the fiber is chemically etched down to its core, which is then precisely aligned above the taper structure and secured with an epoxy adhesive (Norland 146h). This adhesive provides a good refractive index match with the waveguide cladding, ensuring efficient light transfer. In this configuration, light is initially coupled from the optical fiber into the taper, which subsequently acts as a multimode waveguide, supporting multiple optical modes for the sensing application.

Once the key structural parameters were defined, the device design and optimization were carried out using Ansys Lumerical software. The following design procedure was implemented:

- 1. **Modal Analysis of the Waveguide:** The waveguide geometry was optimized to determine the supported modes. For simplicity, only transverse electric (TE) modes were considered.
- 2. Coupling Structure Design: The taper and fiber core were modeled, followed by a modal analysis of two unperturbed scenarios—one with the fiber core removed and the other with the taper core removed.

- 3. **Effective Index Matching:** The effective index of each propagating TE mode within the taper was plotted as a function of taper width. The fiber core scenario has only one effective index value, corresponding to LP_{01} . The width at which the effective indices of both scenarios matched was identified for each taper mode.
- 4. **Taper Width Selection:** The initial and final widths of the taper were chosen based on the modes intended for sensing. Higher-order modes were preferred due to their significant evanescent tail, which enhances interaction with the external medium. Additionally, these modes require larger taper dimensions, allowing for a more fabrication-tolerant design.
- 5. **3D Modeling and Light Propagation Simulation:** A full 3D model of the device, including the fiber core, taper, and waveguide, was built. The EigenMode Expansion (EME) solver was employed to simulate light propagation along the complete structure.
- 6. Non-Linear Taper Optimization: The taper was divided into sections to create a non-linear structure. A length sweep was performed in the sections where the desired modes were coupled, and the power distribution among modes was analyzed at the end of the taper. Based on these results, optimal section lengths were determined.
- 7. **Interferometric Pattern Acquisition:** Using the power distribution obtained in the previous step, the interferometric pattern at the waveguide output was recorded. This process was repeated for aqueous sucrose solutions with varying refractive indices due to their different concentrations.
- 8. Image Processing and Sensor Performance Evaluation: The interferometric patterns were compared using image processing techniques, specifically the 2D Pearson correlation coefficient. From these values, the sensitivity and limit of detection (LoD) of the optical biosensor were calculated.

Results

The coupling efficiency between the optical fiber and the waveguide is a crucial factor in optimizing the device's performance. Fig. A.2 illustrates the design of the non-linear inverted taper, as well as the power distribution of the propagating modes as a function of the length of each section.

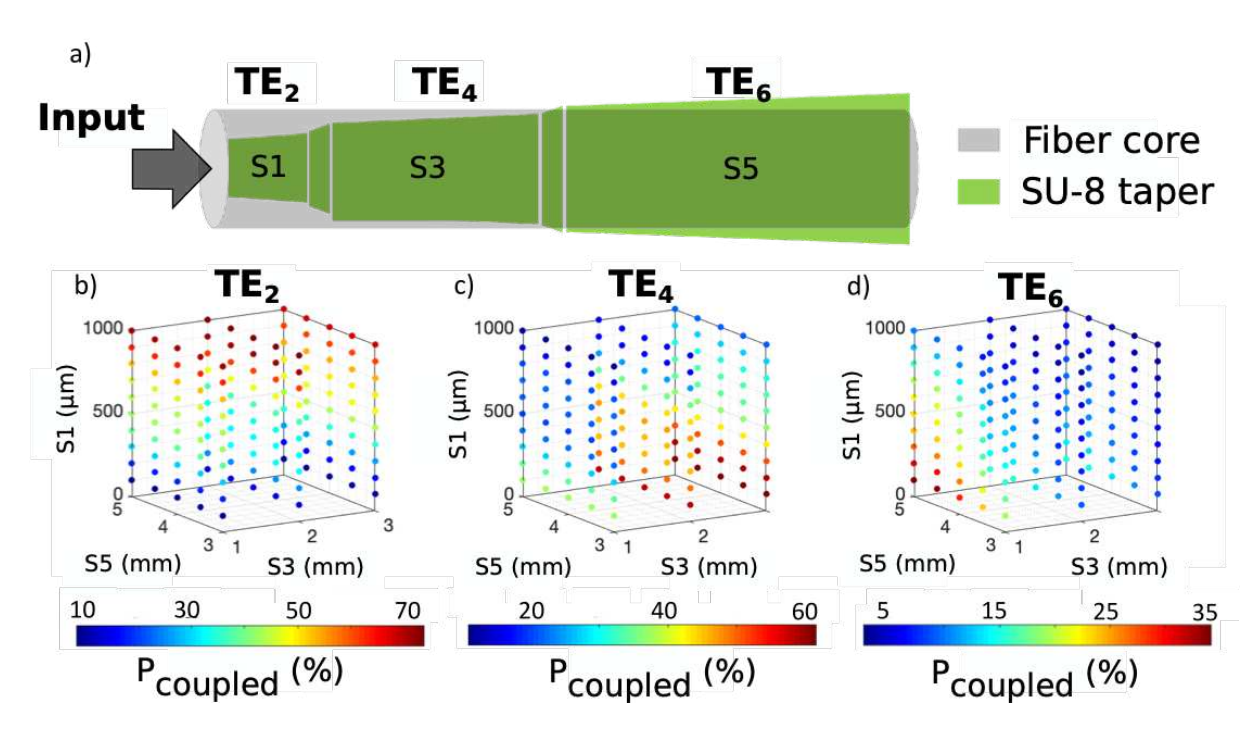


Figure A.2: a) Top view of the coupling system. Percentage of power coupled from fiber to non-linear taper as a function of the length of the taper sections for b) TE_2 , c) TE_4 and d) TE_6 modes.

The analysis reveals that longer taper sections generally result in higher power coupling from the fiber into the taper. However, the efficiency of coupling is also influenced by the remaining power available in the system. For example, the TE₂ mode is predominantly coupled in the first section (S1). As depicted in Fig. A.2b, the highest coupling efficiency for TE₂ is observed at the top face of the graph, indicating that the longest S1 leads to the maximum coupled power, independent of the subsequent sections. Conversely, for higher-order modes such as TE₄, the highest power values are found at the edge of the graph (see Fig. A.2c), corresponding to the longest S3 and the shortest S1. A similar trend is observed for the TE₆ mode, where maximum coupled power occurs at a specific vertex in the parameter space (see Fig. A.2d), corresponding to a configuration in which S5 is maximized while both S1 and S3 are minimized.

By leveraging this comprehensive coupling map, an optimal taper configuration can be selected for the sensing application. The ability to strategically control power distribution among modes provides flexibility in designing the waveguide for specific detection requirements, ensuring enhanced sensitivity and performance.

For the detection stage, interferometric patterns were captured at the waveguide output using a specific set of section lengths: $S1 = 200 \ \mu m$, $S3 = 1 \ mm$, and $S5 = 5 \ mm$. The total waveguide length was set to 1.5 mm. To evaluate the sensor's performance, the device was tested as a sucrose sensor, utilizing the refractive index values presented in Table 4.1 for aqueous sucrose solutions at concentrations of 2%, 5%, 8%, and 10%.

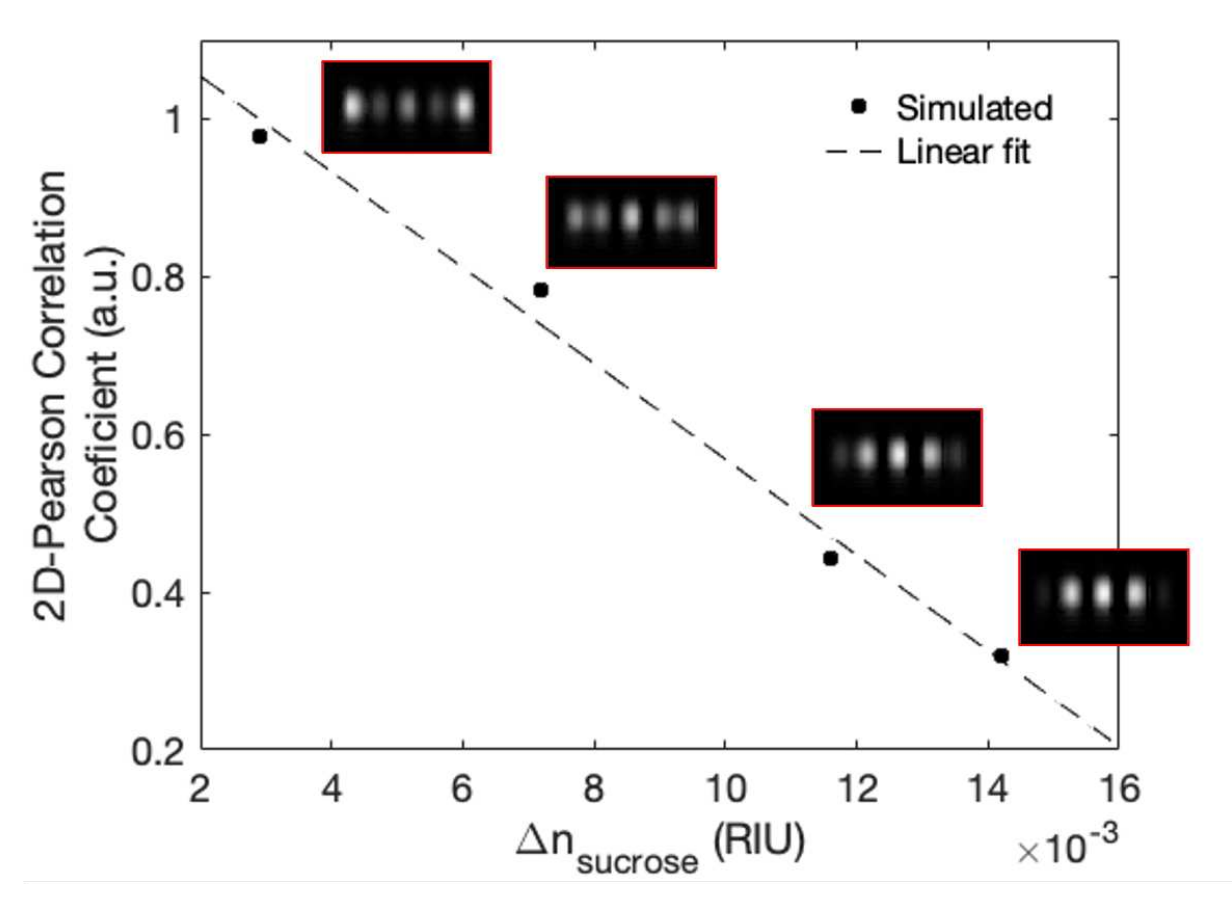


Figure A.3: Sensitivity curve of the device for sucrose detection. The insets display the interferometric patterns corresponding to each sucrose solution.

The calibration curve of the sensor, shown in Fig. A.3, was generated from these simulations. This curve represents the 2D Pearson correlation coefficient as a function of the refractive index variation. By applying a linear fit, the sensor's sensitivity-determined by the slope of the curve-was found to be 61 a.u./RIU. The limit of detection (LoD) was calculated using equation 2.4, incorporating the standard deviation obtained from a similar setup based on CCD acquisition [115]. The estimated LoD was 1.4×10^{-5} RIU.

The proposed device exhibits competitive sensing performance, yet its primary contribution lies in its design as a genuine Point-of-Care (PoC) platform. The sensor was developed with essential features that enable operation outside laboratory environments, ensuring practical applicability. Moreover, the fabrication process is simple and cost-effective, facilitating large-scale production. Additionally, the use of software-based processing techniques allows for continuous system improvement without requiring expensive hardware modifications, further enhancing the feasibility of real-world deployment.

Appendix B

What not to do: common mistakes

During the course of this doctoral research, valuable experience was gained through the various stages of the project. To contribute to the scientific community and assist future researchers in optimizing procedures, the following list of recommendations is provided.

Design and simulations

- Do not mix the simulation configurations for isolated nanoparticles and nanoparticle arrays. The performance of isolated nanoparticles is evaluated using the scattering cross-section, measured with a box monitor surrounding the nanoparticle and a Total-Field Scattered-Field (TFSF) source placed between the nanoparticle and the scattering monitor. In contrast, for nanoparticle arrays, two monitors should be placed above and below the array to measure transmittance and reflectivity, with a plane wave source for excitation.
- Carefully set the boundary conditions. In isolated nanoparticle simulations, do not use periodic conditions; however, symmetry conditions can be applied depending on the nanoparticle's geometry. For nanoparticle array simulations, Bloch/periodic conditions must be applied in the 2D array direction. In both cases, Perfectly Matched Layers (PML) should be used in the vertical direction.
- Verify the material dataset. If possible, characterize the materials used in fabrication and upload this data to the simulation environment, ensuring proper interpolation. If material characterization is not feasible, select the most appropriate model available in the software or from reliable databases.
- Model the system as close as possible to experimental conditions. For instance, consider the thin titanium adhesion layer deposited before gold or adjust the geometry and dimensions based on the actual fabricated structures.

• Keep in mind that while most simulations assume an air environment, the biosensor operates in aqueous solutions. To avoid unexpected shifts in resonance wavelengths, do not design the system to operate at the limit of the desired spectral band.

Nanofabrication

- Inspect the substrate before starting the fabrication process. Verify vendor-provided data, such as surface roughness, transmittance, resistance, and refractive index. High roughness may complicate fabrication, while low transmittance can hinder optical characterization.
- Depending on cleanroom and equipment availability, some fabrication steps—including cleaning, spin-coating, lithography, development, gold deposition, and lift-off—may need to be performed on different days. To prevent damage (e.g., resist evaporation), store samples in nitrogen chambers between steps.
- If several days pass after PMMA deposition, the substrate may act as an insulator, leading to excessive charging during e-beam lithography, which can complicate patterning. To mitigate this, deposit a 2-nm gold layer via sputtering to make the substrate conductive. After lithography, remove this layer using a gold etchant before development.
- For large-area nanoparticle arrays, e-beam lithography software divides the total area into smaller writing fields (typically 100–500 μm per side). Although these fields are aligned via interferometric techniques, alignment errors (stitching) may still occur. To prevent nanoparticles from being located at writing field boundaries, carefully define the origin coordinates, writing field area, and lattice parameters before patterning.

Experimentation

- Do not work blindly. Always visualize the sample during measurements. Whether measuring transmittance spectra or time-dependent signals, split the transmitted light and direct a portion to a camera to observe the sample. Verifying what is being measured ensures the accuracy of results. While an optical microscope is ideal, if unavailable, a suitable custom setup can be used, as demonstrated in this work.
- Although this type of device is often disposable, consider reusing samples for noncritical tests, such as verifying biofunctionalization steps (e.g., aptamer application or analyte immobilization). For reuse, clean samples with IPA and a nitrogen jet, but avoid ultrasonic baths, which may detach the nanoparticles.

- Although some studies use MgCl₂ in buffer solutions, our experiments demonstrated that it causes aptamer degradation. Avoid its use for cortisol aptamers.
- Turn off ambient lights during scattering measurements. Since scattering signals are
 weak and measured against a dark background, external light sources may introduce
 noise. For optimal results, conduct experiments in a dark room or turn off lab lights
 during data collection.
- Carefully position the electrodes for cell stimulation. Given the small size of the nanoantenna array and biological cells, electrodes must be placed close enough to ensure electric field lines pass through both the nanoantenna array and the cells. Remember that microscopes and cameras provide only a top-down view, so also consider vertical positioning when setting up experiments.

Appendix C

List of publications

The following journal articles and conference proceedings, published, submitted, or in preparation, have resulted from this doctoral research.

Journal articles

- U. F. S. Roggero, B. M. Hryniewicz, A. Santana, A. Garcia-Etxarri, A. Seifert, L. Kubota (in memoriam), J. W. Bassani, H. E. Hernández-Figueroa, "Dual-Functionality Plasmonic Nanoparticle Array for biosensing and electrophysiological recording", 2025. In preparation.
- 2. U. F. S. Roggero, C. J. Rojas-Bejarano, C. A. Herreño-Fierro, A. Seifert, A. Garcia-Etxarri, H. E. Hernández-Figueroa and M. Zapata-Herrera, "Surface Lattice Resonances for High-Performance Sensing: A Study on Gold Nanoparticle Arrays", Optics Express, 2025.
- 3. S. Anbumani, A. M. da Silva, **U. F. S. Roggero**, A. M. Silva, H. E. Hernández-Figueroa, and M. A. Cotta, "Oxygen plasma-enhanced covalent biomolecule immobilization on SU-8 thin films: A stable and homogenous surface biofunctionalization strategy", *Applied Surface Science*, 2021.

Conference proceedings

 U. F. S. Roggero, M. Zapata-Herrera, A. García-Etxarri, A. Seifert and H. E. Hernández-Figueroa, "Plasmonic nanoantennas for biosensing and monitoring of cell activity", 2024 International Conference on Optical MEMS and Nanophotonics (OMN), 2024.

- M. T. Korsa, J. Etxebarria-Elezgarai, U. F. S. Roggero, H. E Hernández-Figueroa, J. Adam and A. Seifert, "Multivariate design and data analysis for plasmonic sensing", Smart Photonic and Optoelectronic Integrated Circuits 2024, 2024.
- 3. U. F. S. Roggero, J. R. Fernández, A. Seifert and H. E Hernández-Figueroa, "Pigtailed Polymeric Optical Biosensor based on Interferometric Multimode Waveguide and Image Processing", 2023 International Conference on Optical MEMS and Nanophotonics (OMN) and SBFoton International Optics and Photonics Conference (SBFoton IOPC), 2023.
- 4. U. F. S. Roggero, R. E. Rubio-Noriega, A. Seifert and H. E Hernández-Figueroa, "Highly selective, compact and efficient vertical in-coupling for interferometric optical biosensors", *Journal of Physics: Conference Series*, 2022.